Flow Limits in Slide Coating

A dissertation
submitted to the Faculty of the Graduate School
of the University of Minnesota

by

Kristianto Tjiptowidjojo

In partial fulfillment of the requirements
for the degree of
Doctor of Philosophy.

Adviser: Marcio S. Carvalho

December 2009

Acknowledgments

I would like to acknowledge my gratitude to my co-advisors: The late Professor L. E. "Skip" Scriven and Professor Marcio S. Carvalho. Skip had been instrumental in shaping my research philosophy, especially by his insistence to keep reaching for better - excelsior. Marcio has been an excellent mentor by providing invaluable advice and guidance throughout my graduate studies.

I would also like to acknowledge my gratitude to my unofficial advisors: Wieslaw Suszynski and Dr. Juan de Santos. Wieslaw provides invaluable technical assistance in all of the experimental aspects of this research. Juan acted as a "convergence doctor" in helping me get the first solution of my viscocapillary model of slide coating.

Finally I would like to thank my colleagues, past and present, in the Coating Process Fundamentals Program at the University of Minnesota and Pontifical Catholic University at Rio de Janeiro. A foremost mention goes to Dr. Jaewook Nam who has become my compatriot for 4.5 years in room 66 and patiently kept up with my silly banters. A special thanks goes to all of the helps and friendships from the rest of room 60/66 past and present inhabitants: Dr. Takeaki Tsuda, Makoto Komatsubara, Dr. Hiroaki Kobayashi, Dr. Hiroshi Yoshiba, Yoshifumi Morita, Tomohiro Matsuda, Kazuhiko Morizawa, Dr. Eungsik Park, J. Alex Lee, Benson Tsai, and Damien Brewer. A special thanks also goes to the PUC-Rio colleagues: Dr. Juliana Valerio, Dr. Sygyfredo Cobos, Melissa Becerra, and Danmer Maza. I would also like to thank Phil Jensen for all of his helps in administrative related matter.

Contents

List of Figures

List of Tables

Chapter 1

Introduction

1.1 Precision Coating

Coatings are produced by depositing liquid layer onto a substrate and solidifying it afterwards. Coatings are vital ingredients in a wide range of products such as paper for printing, polymeric films for packaging, photographic films, polymer membranes, adhesive labels, magnetic storage media, and optical films in the flat panel display. The process can typically be divided into two major steps: Liquid application step, or sometimes referred as the coating step, and the solidification step. This study focuses on the liquid application step.

Some products such as optical film for flat panel display, shown in Fig. 1.1, requires thin film with the wet thickness in the order of 50 μm or less and thickness variation less than 5 % for each layer. Such precision is typically achieved by employing *pre-metered* coating methods, where the amount of the liquid is metered first before it is applied to a substrate and all of the liquid fed is coated to the substrate. The thickness of the coating is then governed solely by the liquid flow rate and the substrate speed and is independent of the liquid properties and other operating conditions. The alternatives of this method are *post-metered* and *self-metered* methods. In post-

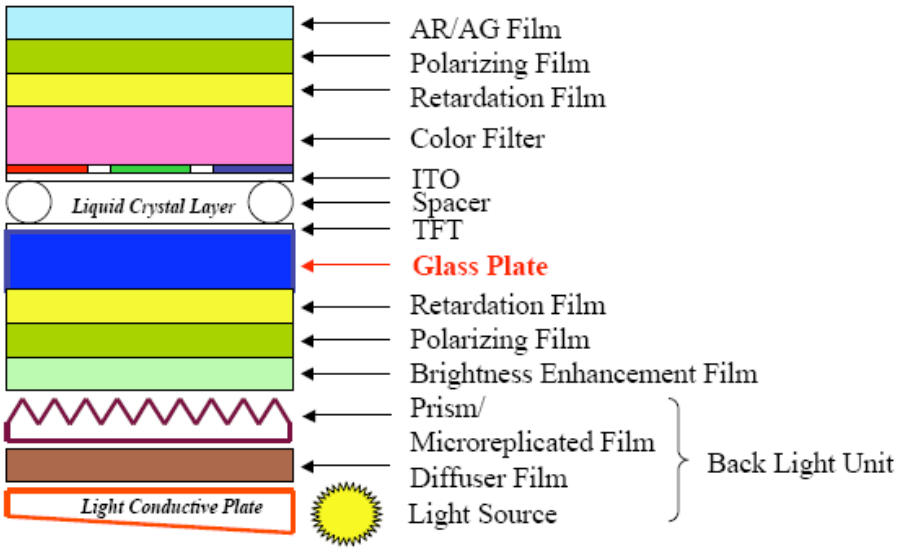

Figure 1.1: An example of precision coating products: Optical film in flat panel display. (From Fuchigami (2005))

metered method, the metering action is performed after the application step where blade or a knife is used to scrape off the excess liquid and the final film thickness is governed by the position of the blade or knife and the applied loading force. In the self-metered method, the thickness of the coating is governed by the geometric configuration of the coater, liquid properties, and other operating conditions.

Most common pre-metered coating methods consist of a family of slot, slide, and curtain coating. In slot coating, the liquid is delivered through a feed slot and picked up immediately by moving substrate or web. The web is either supported by a backing roll, as in the conventional slot coating shown in Fig. 1.2(a), or wrapped under tension around the slot-die itself, as in the tensioned-web-over slot coating shown in Fig. 1.2(c). In slide coating, the liquid forms layers of film flowing down the slide-die before coated to the web. The die is either positioned next to the web as in the conventional slide coating shown in Fig. 1.2(b) or at certain elevations above the web, as in the slide-fed curtain coating shown in Fig. 1.2(d).

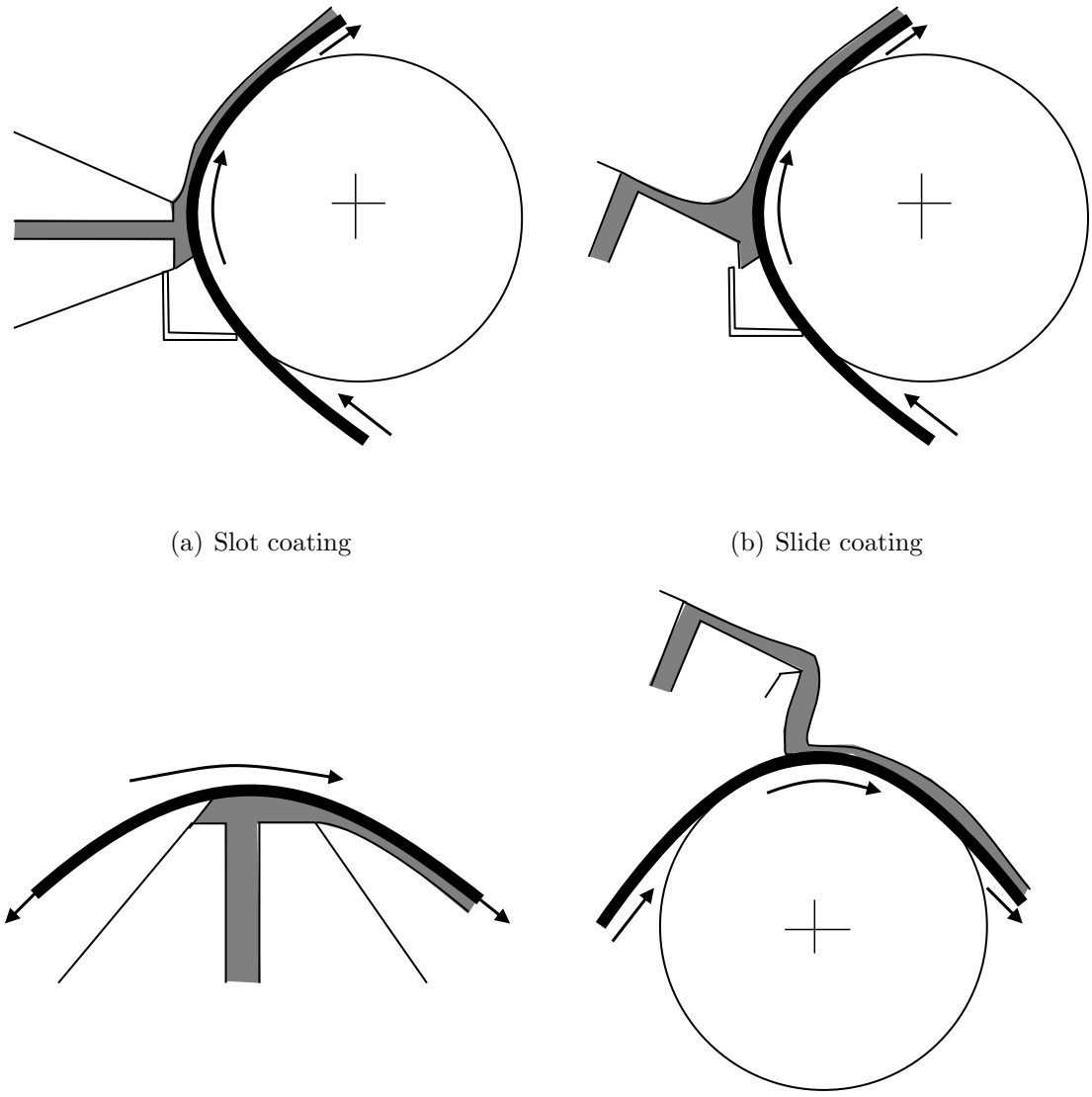

(a) Slot coating

(b) Slide coating

(c) Tensioned web Over slot-die coating

(d) Slide-fed curtain coating

Figure 1.2: Schematics of most common pre-metered coating methods.

Slide coating is the leading method for simultaneous multilayer coating, especially for coating more than three-layer simultaneously. Its advantage over slot coating method is that the die is designed to be able to incorporate additional layers simply by repeating the die-block assembly, as demonstrated by Mercier et al. (1956) in Fig. 1.3(b).

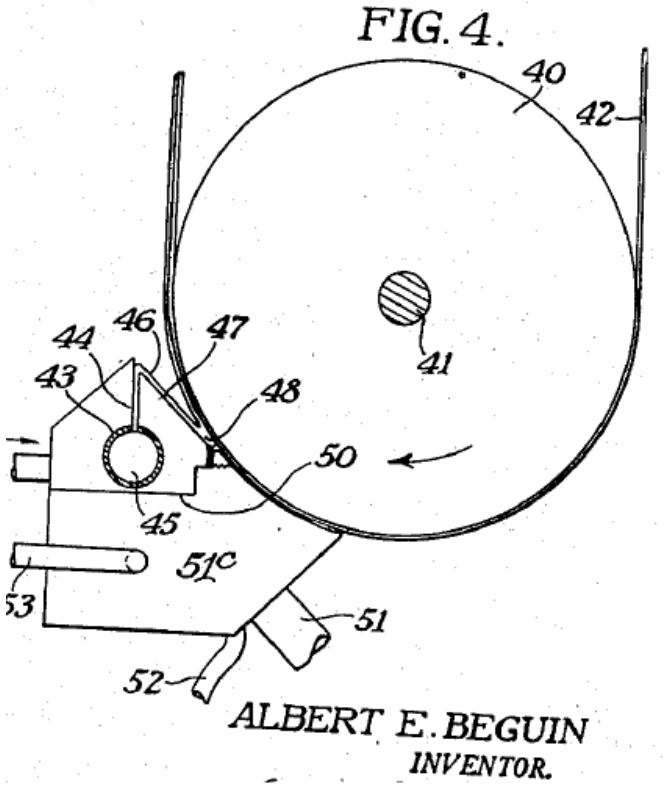

(a) Single-layer slide coating by Beguin (1954)

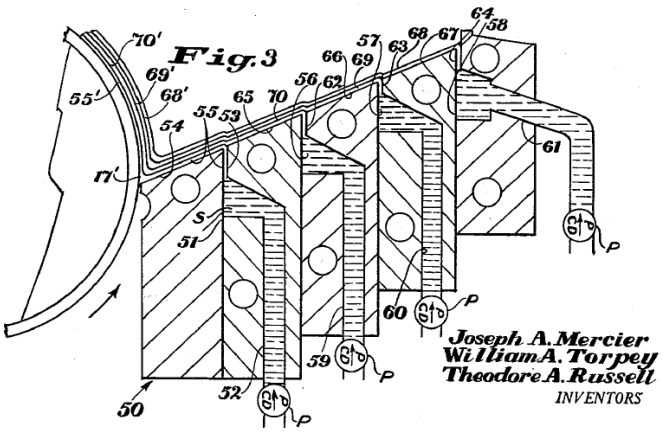

(b) Multilayer slide coating by Mercier et al. (1956)

Figure 1.3: Early patents on slide coating

Slide coating has been demonstrated to be able to coat as many as 20 layers simultaneously, making it the method of choice for precision multilayer coating process. This technology was originally developed for application in color photographic film products, but now has evolved for producing magnetic recording media, as demonstrated by Kolb and Huelsman (2004), medical device as claimed by Schwarz (2008), and other multilayer products that require precision coating.

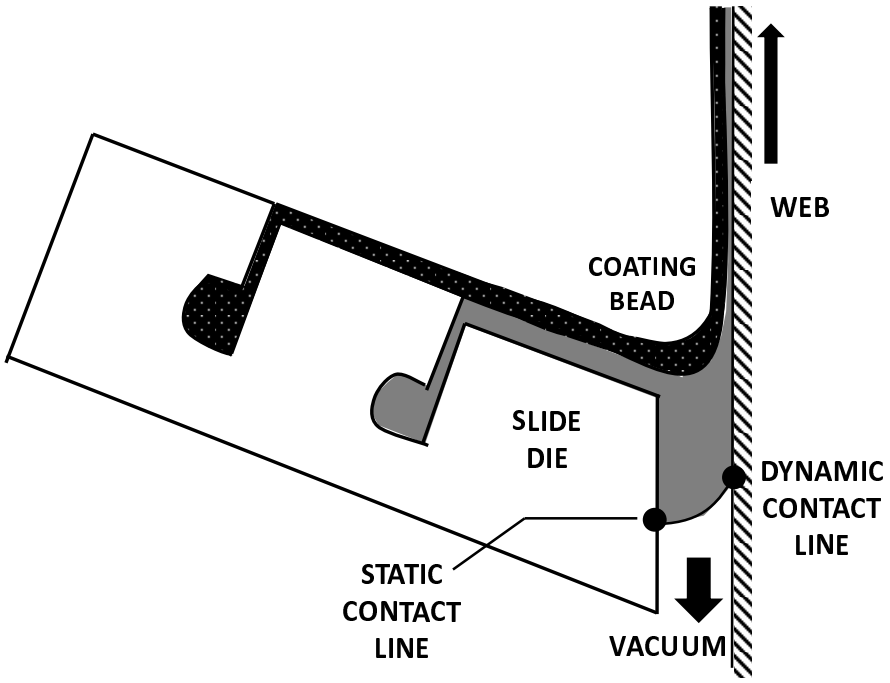

Figure 1.4: Schematic of slide coating

In slide coating, as shown in Figure 1.1, the coating liquids are delivered through feed slots onto an inclined surface, *slide*, where they form layers of liquid film flowing down the slide-die and form a liquid bridge, *coating bead*, onto the moving web, where the liquid is then carried to the solidification process. In practice, a reduced pressure, so-called *vacuum* is applied underneath the coating bead in order to stabilize it, especially at the thin coating condition. The technique of applying vacuum

underneath the coating bead was invented by Beguin (1954), in the same patent that he introduced single-layer slide coating, as shown in Fig. 1.3(a).

The coating action occurs in a line where the bead contacts the web. The underlying physics occurring in this line, the *dynamic contact line*, has not yet been well-resolved in terms of basic principles. The no-slip boundary condition that is well-established in fluid mechanics does not apply near the dynamic contact line because if the condition were true, the shear and extensional rates would be infinite there and coating would be impossible. Such local singularity will not be true in nature and there must be submicroscopic processes that operate to relieve the singularity. The apparent contact angle between the liquid's free surface and the web is called *dynamic contact angle* and its dependence to the flow field and surface properties is still an active research area today.

The lower meniscus of the bead also intersects the lip of the slide and the intersection line is called *static contact line*. This too is a submicroscopic three-dimensional region. In practice, the position of the static contact line may be pinned to a convenient location such as the sharp die-lip edge or it may be allowed to wet the die face. In some cases, wetting the die face, as shown in Fig. 1.1, is more preferred than pinning the static contact line to the die-lip edge due to the buffer zone created by large separation between downstream and upstream menisci.

1.2 Operability Limits: Coating Window

Slide coating, like other coating methods, is subject to defects and failures due to fluid mechanical instabilities, especially in the bead, although three-dimensional edge effect play important role too. Some of these defects and failures have been identified, as shown in Figure 1.2.

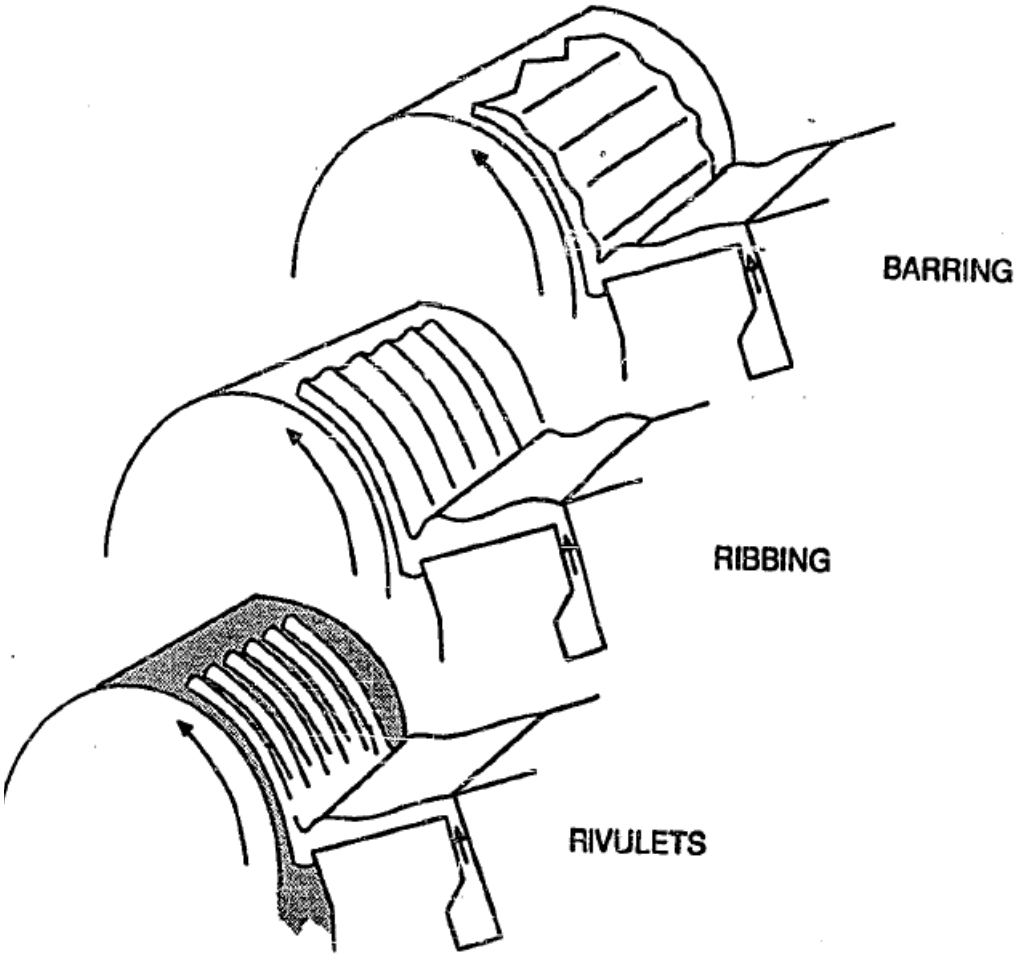

Figure 1.5: Schematic of common coating defects. (From Christodoulou (1990))

Applied vacuum fluctuations can lead to the coating bead oscillation that causes *barring*, coating thickness variation along the downstream direction. Another type of flow instability that can occur is the *ribbing* instability that creates non-uniformity along the cross-web direction. In some extreme conditions, the two-dimensional flow far from the edge does not exist and what is observed is alternating wet and dry stripes called *rivulets*. Applying too high of a vacuum can lead to a flow state at which liquid flows towards the vacuum chamber, the premetered action is lost and generally the thickness no longer becomes uniform.

All these defects set the operability limits of the coating process. Knowing operating conditions at which each defect or failure occurs is essential in producing defect-free coating. The operating condition range where the coating is possible is usually referred as *coating window*.

Slide coating window, even for single-layer case, is not well understood as the slot coating window. Slot coating operability limits have been well studied and the bead breakup mechanisms have been identified as well. Study of slot coating window was started by Ruschak (1976) in his theoretical analysis of slot coating bead. He determined the feasibility limits of the slot coating bead by regarding it as quasi-static, i.e., dominated by capillary pressure, and neglecting viscous stresses and pressure drop inside the bead. He defined the operability limit based on the possible curvatures of upstream and downstream menisci, which translates to the sustainable pressure jump between them. These sustainable pressure jump limits impose constraints on admissible operating parameters. Higgins and Scriven (1980) refined Ruschak's analysis by incorporating viscous forces in the bead to form an improved coating window. A comprehensive experimental of a feasibility coating window for slot coating was performed by Sartor (1990) where he mapped the coating window by performing flow visualization and recorded the onset of rivulets, ribbing, and weeping. He showed that the prediction of feasibility window from viscocapillary model agree qualitatively with experiment. Gates (1999) studied how the die lip shape alters the coating window by performing experiments and computer-aided theory. Romero et al. (2004) presented a complete coating window in their study on slot coating low flow limit with diluted solution of high molecular weight polymer. Some of the coating windows that they reported are shown in Fig. 1.2.

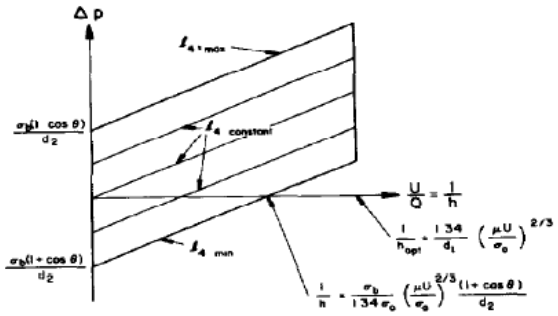

(a) Ruschak (1976)

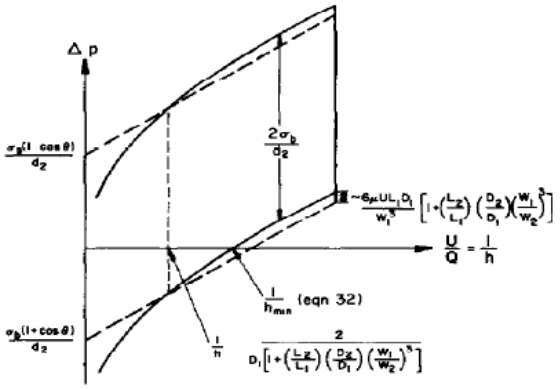

(b) Higgins and Scriven (1980)

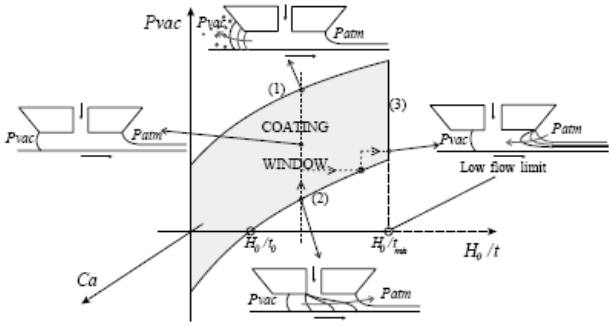

(c) Romero et al. (2004)

Figure 1.6: Progression of slot coating windows development

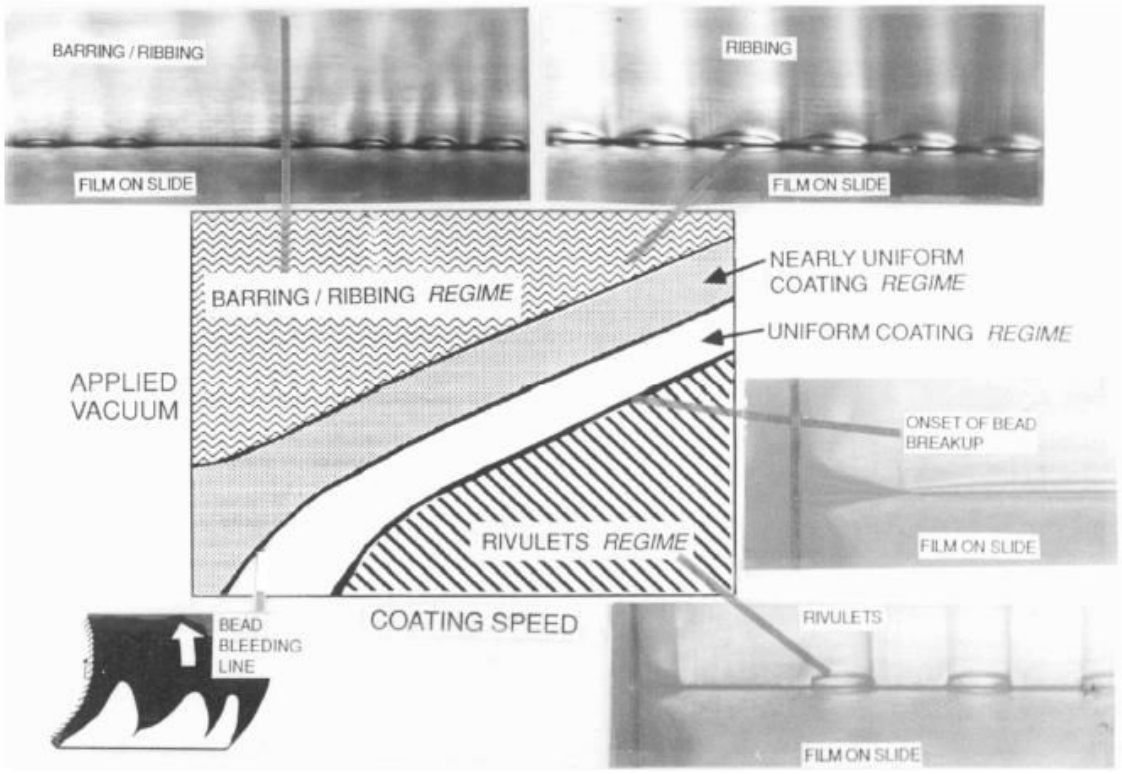

Figure 1.7: Experimental slide coating window reported by Chen (1992)

Most of the slide coating windows reported in the literatures came from experiments. Tallmadge et al. (1979) reported experimental values of lower and upper coating speed limits under different flow rates, gap widths, and viscosities. They did not apply vacuum underneath the coating bead. Gutoff and Kendrick (1987) improved Tallmadge et al. (1979)'s experimental methods by incorporating vacuum in their studies of slide coating's low flow limit at different viscosities and gap widths. They demonstrated that thinner coating can be achieved when vacuum is applied underneath the bead. Chen (1992) reported experimental values of vacuum limits at different coating thickness, but he did not investigate low flow limit. Hens and van Abbenyen (1997) added experimental values of ribbing and rivulets formation. Schweizer (1988) improved flow visualization technique of coating flows with the use of dye and hydrogen bubbles and he was able to capture streamlines and vortices in the slide coating flow.

With those tools, he was able to report critical flow rates corresponding to the onset of vortex birth at the downstream meniscus at a given coating speed. However none of these studies explored coating bead breakup mechanisms and the effects of the die geometry to the operability windows.

The goals of this study is to identify the mechanisms of the slide coating bead breakdown and to predict their corresponding critical operating conditions. It starts with a development of a one-dimensional viscocapillary model of slide coating and that is discussed in Chapter 2. The chapter contains a thorough critical examination of a slide coating model based on a combination of nonlinear asymptotic models of flow down the slide and up the moving web. Effects of the conditions employed to match both film profiles and the way they are imposed in the discrete system is examined. Furthermore, the effect of different operating parameters on the flow and the limits of the process are investigated as well. The range of applicability of the one-dimensional nonlinear model is determined by comparing the predictions to the solution of the complete two-dimensional Navier-Stokes.

Based on our evaluation of the model's inadequacy in describing the flow at the coating bead, especially at high capillary and Reynolds numbers, we propose an improvement of the model by augmenting it with full two-dimensional Navier-Stokes theory in the coating bead, where the flow is mostly two-dimensional. The hybrid model development together with the validation study is discussed in Chapter 3. The chapter contains the construction of the model by sandwiching coating bead region, where two-dimensional Navier-Stokes is applied, with two regions, slide and web regions, where one-dimensional viscocapillary model is applied. Multiple combination of numbers and types of matching conditions used for stitching these region are explored and their effects on the prediction of free surface shape, pressure field, and streamlines are studied as well. The model is then validated by comparing the predictions to the solution of the complete two-dimensional Navier-Stokes.

Advances in the theoretical modeling of coating flow, especially in slide coating, was developed by Christodoulou and Scriven (1989) where they solved full 2-D steady Navier-Stokes with Galerkin finite element method. However, due to high computation in that time, they only made few excursions in parameter space and did not perform systematic exploration to find operability limits. A continuation of the works of Christodoulou and Scriven (1989) is covered in Chapter 4. Through systematic parametric study, we uncovered coating bead breakup mechanisms at low vacuum, high vacuum, and low flow limits. The information of these bead breakup mechanisms are then used to construct theoretical prediction of onset of low vacuum, high vacuum, and low flow limits at different coating speed, hence forms a coating window. A stability criterion based on simple stability analysis is later added to the model that allows for predicting onset of ribbing instability in the coating window.

The prediction of the bead breakup mechanisms and coating windows are verified with flow visualization experiment and this subject is covered in Chapter 5. Bead breakup mechanisms at low-vacuum limit, high-vacuum limit, and low-flow limit are uncovered with the aid of through-the-roll viewing of the bead and a high speed camera. Experimental coating windows are also mapped and compared with predictions from the computer-aided theory at different coating speed, gap width, and slide inclinations.

Chapter 2

Viscocapillary Model of Slide Coating

2.1 Introduction

Many important aspects of coating flows are well accounted for by one-dimensional lubrication and viscocapillary models that are easier to set-up, computationally far less expensive to use, and more straightforward to interpret than families of solutions of two-dimensional Navier-Stokes equation system. The latter is generally more accurate and reliable, but requires specialized algorithms to account for the free surface and demands substantial computation time (Christodoulou and Scriven, 1989). Youn et al. (2006) present a review of the available viscocapillary models for pre-metered coating flows. Unlike slot coating, no simple accurate model of even single-layer slide coating has emerged. We believe the absence of an accurate model is caused by the less confinement of the liquid by solid surfaces, and the non-unidirectional flow at the film formation region.

A viscocapillary model for slide coating flow that ignores inertia and balances viscous force with capillary pressure was presented by Galehouse and Colt (1984). Their model consists of analytical solutions of the linearized film profile equations of flows

down an inclined plane and up a moving surface, which are valid approximations only far upstream on the slide and far downstream on the web. The bead that connects these two regions is assumed to be thick enough yet immune to gravity so that its pressure is constant and its upper free surface is an arc of circle. These three parts, slide flow, web flow, and circular bead, are spliced together by requiring inclination and curvature to be continuous at two arbitrarily chosen matching points, as shown in Figure 2.1(a). This model, though crude, is the pioneering attempt at a simple one-dimensional viscocapillary model of slide coating.

Another simple model was proposed by Hens and van Abbenyen (1997). They focused on neither the arriving film flow on the slide nor the departing flow on the web. Instead, they defined a bead region, as shown in Figure 2.1(b), to construct for it an overall momentum balance by postulating plausible influxes and outfluxes of momentum together with gravitational forces acting on the bead section, pressure ("vacuum") on free surfaces, surface tension at cuts in free surfaces, and most problematic of all, viscous drag on the portions of slide and web that are inside their control volume. The severe limitation is the empiricism of their estimates, above all the appeal to Sakiadis' patently inappropriate boundary layer flow and the disregard of the flow rearrangements in the bead region, including the effect of capillary pressure gradient from varying curvature of the flow's upper free surface. In essence they postulated solutions of the Navier-Stokes system for viscous free surface flow in the bead without examining critically the then available Navier-Stokes solutions (Christodoulou and Scriven, 1989).

Nagashima (1993, 2004) attempted to extend Galehouse and Colt's model to include more of the flow rearrangements in the bead region by not linearizing the film profile equations on the slide and the web and retaining the inertia, i.e. momentum convection, terms in them. But instead of interposing an effectively static bead region in between the one-dimensional slide and web flows as Galehouse and Colt did, he spliced the solution of the slide flow equation with that of web flow equation directly at a plausibly, yet arbitrarily chosen, matching point, as shown in Figure 2.1(c). He did so in the expectation that the viscous and inertial force would become negligible at the matching point so that both equations would describe one and the same nearly

static meniscus there. They do not, however, in the parameter ranges Nagashima examined. So the question remains as to whether there is a parameter range at which one-dimensional models of slide coating is accurate. Another important point is the possibility of improving the one-dimensional models by developing simple yet accurate models of the coating bead region to fit correctly between the nonlinear asymptotic approximations of the flow down the slide and along the web. Jung et al. (2004) used similar approach to study a slide-fed curtain coating process, the solution of the film profile equation down the slide was matched to the solution of the film profile equation of a free falling liquid curtain.

This work presents a thorough critical examination of the nonlinear asymptotic model for the flow down the slide and up the moving web reported by Nagashima (1993, 2004). The model is rewritten in terms of an arc length coordinate system defined along the free surface, which avoids singularities that may occur when a cartesian system is used. Effects of the conditions employed to match both film profiles and the way they are imposed in the discrete system is examined. Furthermore, the effect of different operating parameters on the flow and the limits of the process are investigated as well. The range of applicability of the one-dimensional nonlinear model is determined by comparing the predictions to the solution of the complete two-dimensional Navier-Stokes.

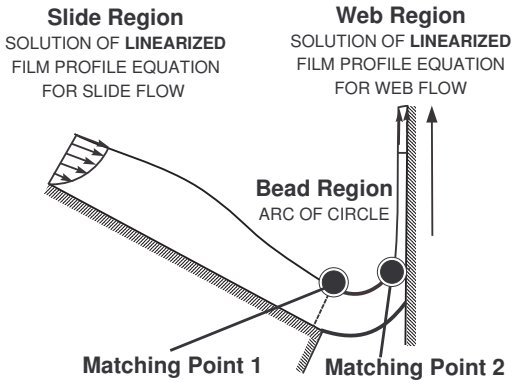

(a) Galehouse and Colt (1984).

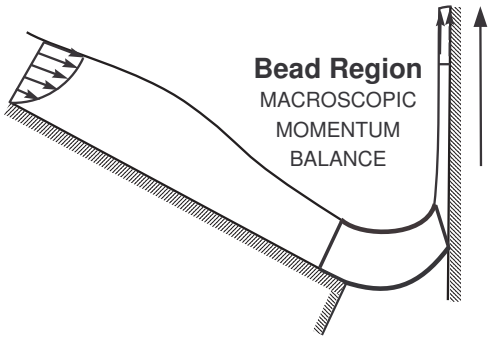

(b) Hens and van Abbenyen (1997).

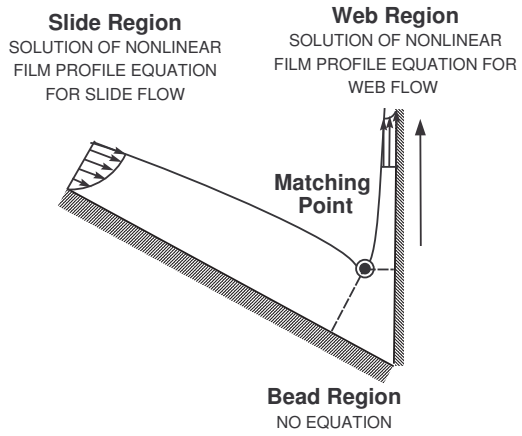

(c) Nagashima (1993, 2004).

Figure 2.1: Proposed simple models of slide coating.

2.2 Nonlinear Asymptotic Model of Slide Coating Flow

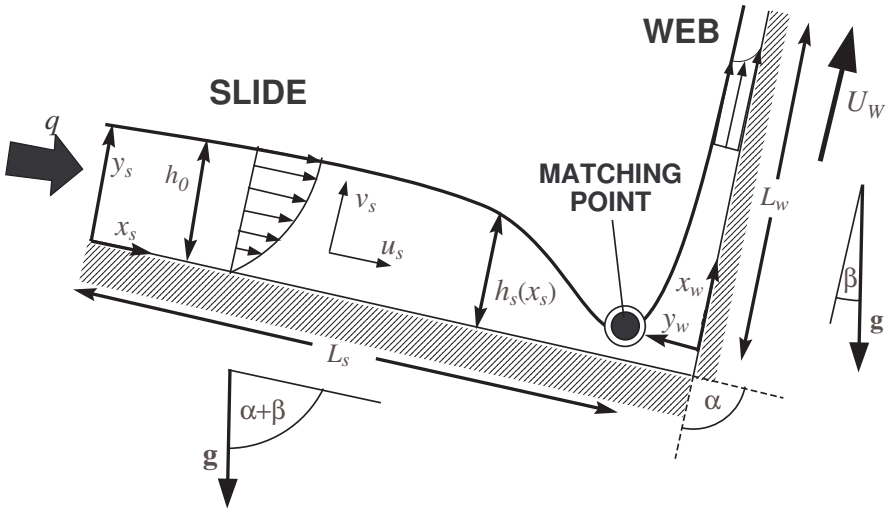

Figure 2.2: Film profile equation of slide coating flow.

2.2.1 Film Profile Equation

The film profile equation is an ordinary differential equation that governs the variation of film thickness along a one-dimensional solid support. The form of the film profile equation depends on the approximations employed in simplifying the complete two dimensional Navier-Stokes equation system. The film profile equation employed by Nagashima (1993, 2004) is obtained with the approach outlined by Higgins and Scriven (1979). Similar approach has been used to derive film profile equation to describe the flow in a slide-fed curtain coating process Jung et al. (2004). The fundamental steps of the derivation of film profile equation of the flow down a slide are shown here as an example of the procedure.

First, the Navier-Stokes equation is simplified by assuming the flow down the slide to be locally rectilinear. The simplification leads to the following equations, where

where the subscript s denotes the variables in the slide region, :

$$\frac{\partial u_s}{\partial x_s} + \frac{\partial v_s}{\partial y_s} = 0 \tag{2.1}$$

$$\mathrm{Re}\left[u_s \frac{\partial u_s}{\partial x_s} + v_s \frac{\partial u_s}{\partial y_s}\right] = 3 - \frac{\partial p}{\partial x_s} + \frac{\partial^2 u_s}{\partial y_s^2} \tag{2.2}$$

$$0 = -3\tan(\alpha+\beta) - \frac{\partial p}{\partial y_s} \tag{2.3}$$

where Reynolds number, Re, is defined to be

$$\mathrm{Re} = \frac{\rho q}{\mu}, \tag{2.4}$$

ρ is the liquid density, q is the flow rate per unit width, and μ is the liquid viscosity. The fully developed film thickness far upstream the slide, h_0, is the chosen unit of length and the average film speed of the fully developed flow, $\frac{q}{h_0}$, is the chosen characteristic velocity.

By using the appropriate boundary conditions at the solid surface and gas-liquid interface, and constant flow rate per unit width q, the velocity profile tangential to the slide is derived:

$$u_s(x_s, y_s) = \frac{3}{h_s}\left[\frac{y_s}{h_s} - \frac{1}{2}\left(\frac{y_s}{h_s}\right)^2\right]. \tag{2.5}$$

The normal component of the velocity profile v_s is obtained from continuity equation (2.1), combined with no penetration condition at slide surface:

$$v_s(x_s, y_s) = u_s \frac{y_s}{h_s}\frac{dh_s}{dx_s}. \tag{2.6}$$

The pressure field is approximated by integrating the normal component of the momentum equation (2.3), and applying normal stress balance at the liquid-gas interface:

$$p = -\frac{1}{\mathrm{Ca}}\frac{\mathrm{d}\kappa_s}{\mathrm{d}x_s} + 3(h_s - y_s)\tan(\alpha+\beta), \tag{2.7}$$

where the capillary number, Ca, is defined as

$$\mathrm{Ca} = \frac{\mu q}{h_0 \sigma}, \tag{2.8}$$

σ is the liquid surface tension and κ is the curvature of the free surface, which for two-dimensional translationally symmetric meniscus is

$$\kappa = \frac{\dfrac{\mathrm{d}^2 h}{\mathrm{d}x^2}}{\left[1 + \left(\dfrac{\mathrm{d}h}{\mathrm{d}x}\right)^2\right]^{\frac{3}{2}}}. \tag{2.9}$$

The film profile equation is obtained by inserting the approximate velocity profiles (2.5) and (2.6) together with the pressure profile (2.7) into the tangential component of the momentum equation (2.2) and integrating it across the film thickness (Christodoulou and Scriven, 1989; Nagashima, 1993, 2004):

$$\underbrace{\frac{1}{3\mathrm{Ca}}\frac{\mathrm{d}\kappa_s}{\mathrm{d}x_s}}_{\text{Capillary Pressure Gradient}} = \underbrace{-\frac{2}{5}\mathrm{Re}\frac{1}{h_s^3}\frac{\mathrm{d}h_s}{\mathrm{d}x_s}}_{\text{Inertia}} + \underbrace{\tan(\alpha+\beta)\frac{\mathrm{d}h_s}{\mathrm{d}x_s}}_{\text{Cross-Streamwise Gravity}} + \underbrace{\frac{1}{h_s^3}}_{\text{Viscous}} - \underbrace{\frac{1}{1}}_{\text{Streamwise Gravity}}. \tag{2.10}$$

Similar analysis can be constructed for the flow up the moving web. The corresponding film profile equation for the flow near the moving web is

$$\underbrace{\frac{1}{3\mathrm{Ca}}\frac{\mathrm{d}\kappa_w}{\mathrm{d}x_w}}_{\text{Capillary Pressure Gradient}} = \left[\underbrace{\frac{\mathrm{Re}}{15}\left(\frac{U_W^2}{h_w} - \frac{6}{h_w^3}\right)}_{\text{Inertia}} - \underbrace{\frac{\sin\beta}{\cos(\alpha+\beta)}}_{\text{Cross-Streamwise Gravity}}\right]\frac{\mathrm{d}h_w}{\mathrm{d}x_w} + \underbrace{\frac{1}{h_w^3} - \frac{U_W}{h_w^2}}_{\text{Viscous}} + \underbrace{\frac{\cos\beta}{\cos(\alpha+\beta)}}_{\text{Streamwise Gravity}}, \tag{2.11}$$

where U_W is the web speed measured in units of the average velocity of flow down far upstream the slide, $\dfrac{q}{h_0}$

2.2.2 Asymptotic Inflow and Outflow Boundary Conditions

The film profile equations (2.10) and (2.11) are third order nonlinear differential equations and therefore require three boundary conditions. Christodoulou and Scriven (1989), Nagashima (1993, 2004), and later Jung et al. (2004) derived inflow and outflow boundary conditions from asymptotic solution of the equations, which are obtained by linearizing it upstream the slide and downstream the web where the flow is nearly fully developed. This derivation is summarized here. At a region far upstream of the slide, the deviation from the fully developed film thickness h_0 is small and the dimensionless film thickness can be expressed as:

$$h_s(x_s) = 1 + \varepsilon_s h_s'(x_s), \tag{2.12}$$

where ε_s is a very small quantity. Similarly, at a region far downstream of the web, the dimensionless film thickness can be expressed as

$$h_w(x_w) = \frac{h_\infty}{h_0} + \varepsilon_w h_w'(x_w), \tag{2.13}$$

where h_∞ is the fully developed thickness on the moving web. In this formulation, h_∞ can not be specified independently of the web speed U_W in order to satisfy the imposed flow rate from the flow down the slide. Retaining terms through $o(\varepsilon_s)$ and $o(\varepsilon_w)$, the linearized film profile equations for slide and web flows are

$$\frac{\mathrm{d}^3 h_s'}{\mathrm{d}x_s^3} - 3\mathrm{Ca}\left[-\frac{2}{5}\mathrm{Re} + \tan(\alpha+\beta)\right]\frac{\mathrm{d}h_s'}{\mathrm{d}x_s} + 9\mathrm{Ca}h_s' = 0, \tag{2.14}$$

and

$$\frac{\mathrm{d}^3 h_w'}{\mathrm{d}x_w^3} + \mathrm{Ca}\left\{\frac{\mathrm{Re}}{5}\left[6\left(\frac{h_0}{h_\infty}\right)^3 - U_W^2\frac{h_0}{h_\infty}\right] + 3\frac{\sin\beta}{\cos(\alpha+\beta)}\right\}\frac{\mathrm{d}h_w'}{\mathrm{d}x_w} + 3\mathrm{Ca}\left[3\left(\frac{h_0}{h_\infty}\right)^4 - 2U_W\left(\frac{h_0}{h_\infty}\right)^3\right]h_w' = 0. \tag{2.15}$$

Solutions of equation (2.14) have the general form

$$h_s'(x_s) = C_1 e^{\lambda_{1,s} x_s} + C_2 e^{\lambda_{2,s} x_s} + C_3 e^{\lambda_{3,s} x_s} \tag{2.16}$$

where the λ_s are the roots of the characteristic polynomial

$${\lambda_s}^3 - 3\mathrm{Ca}\left[-\frac{2}{5}\mathrm{Re} + \tan(\alpha+\beta)\right]\lambda_s + 9\mathrm{Ca} = 0. \tag{2.17}$$

As Christodoulou and Scriven (1989) and Nagashima (1993, 2004) pointed out, of the three roots of equation (2.17), one is real and negative and the other two are complex conjugate roots with positive real part. This is true for slide inclination less than 20$^{\mathrm{o}}$ measured from horizontal direction ($\alpha + \beta < 70^{\mathrm{o}}$), capillary number less than 1, and no inertia. At low capillary number, Ca $\leqq$ 0.01, and creeping flow, Re = 0, this is always true for any slide inclination. Only roots with positive real part are physically relevant because the deviation from the fully developed film thickness should decay in the upstream direction. Consequently, only the complex roots are admissible. The solution of the linearized equation can be written in the form

$$h_s = 1 + \varepsilon_s \exp(\lambda_{r,s} x_s)\cos(\lambda_{i,s} x_s + \Phi) \tag{2.18}$$

where $\lambda_{r,s}$ represents the exponential decay constant, $\lambda_{i,s}$ represents the wavenumber of the standing wave, and Φ is the phase angle of the wave. A free parameter Robin-type boundary condition can be formed by a linear combination of equation (2.18) and its first and second derivatives to eliminate the parameters ε_s and Φ. This serves as the inflow boundary condition for the slide flow:

$$\frac{\mathrm{d}^2 h_s}{\mathrm{d}x_s^2} - 2\lambda_{r,s}\frac{\mathrm{d}h_s}{\mathrm{d}x_s} + \left(\lambda_{r,s}^2 + \lambda_{i,s}^2\right)(h_s - 1) = 0 \quad \text{at } x_s = 0 \tag{2.19}$$

Similarly, the solutions of the linearized film profile equation for the flow up the moving web, equation (2.15), are of the form

$$h_w'(x_w) = C_1 e^{\lambda_{1,w} x_w} + C_2 e^{\lambda_{2,w} x_w} + C_3 e^{\lambda_{3,w} x_w}, \tag{2.20}$$

where the λ_w are the three roots of the characteristic polynomial

$$\lambda_w{}^3 + \mathrm{Ca}\left\{\frac{\mathrm{Re}}{5}\left[6\left(\frac{h_0}{h_\infty}\right)^3 - U_W^2\frac{h_0}{h_\infty}\right] + 3\frac{\sin\beta}{\cos(\alpha+\beta)}\right\}\lambda_w + 3\mathrm{Ca}\left[3\left(\frac{h_0}{h_\infty}\right)^4 - 2U_W\left(\frac{h_0}{h_\infty}\right)^3\right] = 0. \quad (2.21)$$

In the web region, the deviation from the fully developed film thickness should decay along the downstream direction. Consequently, only the real negative root of the characteristic polynomial is admissible. The solution is

$$h_w = \frac{h_\infty}{h_0} + \varepsilon_w \exp(\lambda_{r,w} x_w). \quad (2.22)$$

Two linearly independent Robin-type asymptotic outflow boundary conditions can be derived from eq. (2.22):

$$\frac{\mathrm{d}h_w}{\mathrm{d}x_w} - \lambda_{r,w}\left(h_w - \frac{h_\infty}{h_0}\right) = 0 \quad \text{at } x_w = L_W; \quad (2.23)$$

$$\frac{\mathrm{d}^2h_w}{\mathrm{d}x_w^2} - \lambda_{r,w}^2\left(h_w - \frac{h_\infty}{h_0}\right) = 0 \quad \text{at } x_w = L_W. \quad (2.24)$$

Because these inflow and outflow boundary conditions are independent from the departure measure of fully developed thickness, ε_s and ε_w, and phase angle, Φ, that depends on the location of the boundary, they can be applied at any location, providing that the linearized film profile equations are still valid there.

2.2.3 Matching Conditions

The matching between the flow down the slide and up the moving web is done by requiring the film thickness, its slope, and its curvature to be continuous at an arbitrarily chosen matching point. These matching conditions serve as two outflow

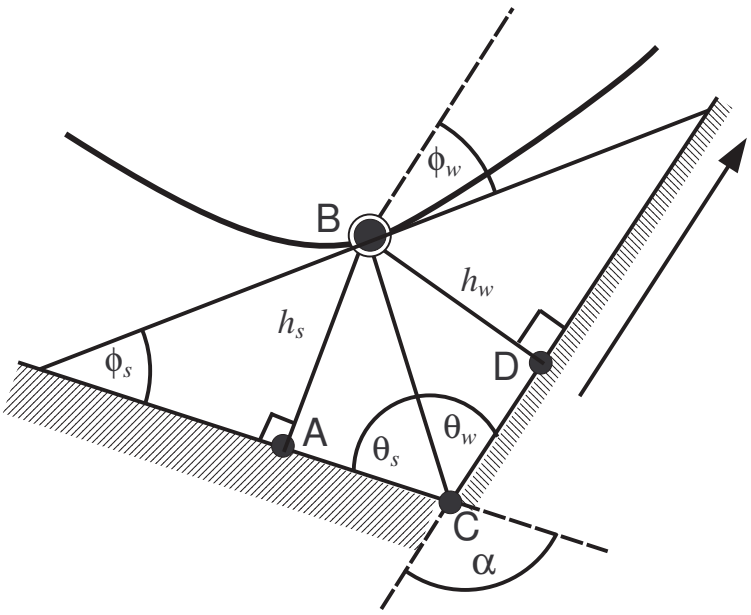

Figure 2.3: Matching the flows.

boundary conditions for the slide flow and one inflow boundary condition for the web flow, thus completing the boundary condition set of each flow region.

Film thickness matching is shown in Figure 2.3. Triangle ABC and BCD have a common hypotenuse at line BC. From the trigonometric law of sines, the film thickness of the slide flow, h_s, and that of the web flow, h_w, are related by

$$\frac{h_s}{\sin\theta_s} = \frac{h_w}{\sin\theta_w}. \tag{2.25}$$

Nagashima (1993, 2004) chose to set the matching location on the bisector ray of the angle between the slide and the web, such that $\theta_s = \theta_w$, and the thickness matching condition reduces to equal film thickness, i.e. $h_s = h_w$. We also employed equal-angle bisecting ray as the matching point in most of our calculation. However, as explained later in Section 2.3.4, we also employed other bisecting angle as well and investigated its effect to the computed thickness profile.

Matching slope of the two profiles is equivalent to relate their inclinations, $\phi_s \equiv$

$\tan^{-1}\left(\frac{\mathrm{d}h_s}{\mathrm{d}x_s}\right)$ and $\phi_w \equiv \tan^{-1}\left(\frac{\mathrm{d}h_w}{\mathrm{d}x_w}\right)$, as depicted in Figure 2.3. Mathematically, ϕ_s and ϕ_w are related by

$$\phi_w = \phi_s + \alpha - \pi \tag{2.26}$$

Curvature of a profile is independent of its orientation in space and therefore independent from the coordinate system. The curvature matching condition is simply

$$\kappa_s = \kappa_w \tag{2.27}$$

2.2.4 Transformation to Arc-Length Coordinate

In order to improve the performance of the numerical method employed to solve the film profile equations, the equations are recast in an arc length coordinate system defined along the free surface. This approach was not employed by Nagashima (1993, 2004) and Jung et al. Jung et al. (2004), although Kheshgi and Scriven (1979) and Kistler and Scriven (1979) had reported great success of employing arc length coordinate to solve the film profile equations. The advantage of the arc length coordinates is that it is, by definition, monotonic along the free surface and so avoids the singularities caused by meniscus inclination of 90^o or even double valued film thickness profile when they are expressed in cartesian coordinates. Such cases would guarantee failure for any numerical method employed for solving them, unless the coordinate system is locally switched to eliminate the singularities, which is impractical. The third-order ODE written in terms of cartesian coordinates along the slide and web that describe the film profile equations are transformed into a system of three first order ODE written in terms of the arc length coordinate plus one additional ODE that relates both coordinate systems. At the slide region, the ODE system is

$$\frac{\mathrm{d}h_s}{\mathrm{d}s} = \sin\phi_s, \tag{2.28}$$

$$\frac{\mathrm{d}\phi_s}{\mathrm{d}s} = \kappa_s, \tag{2.29}$$

$$\frac{1}{3\mathrm{Ca}}\frac{\mathrm{d}\kappa_s}{\mathrm{d}s} = \left[-\frac{2}{5}\mathrm{Re}\frac{1}{h_s^3} + \tan\left(\alpha+\beta\right)\right]\sin\phi_s + \left[\frac{1}{h_s^3} - 1\right]\cos\phi_s, \tag{2.30}$$

$$\frac{\mathrm{d}x_s}{\mathrm{d}s} = \cos\phi_s. \tag{2.31}$$

At the web region, the ODE system is

$$\frac{\mathrm{d}h_w}{\mathrm{d}s} = \sin\phi_w, \tag{2.32}$$

$$\frac{\mathrm{d}\phi_w}{\mathrm{d}s} = \kappa_w, \tag{2.33}$$

$$\begin{aligned}\frac{1}{3\mathrm{Ca}}\frac{\mathrm{d}\kappa_w}{\mathrm{d}s} &= \left[\frac{\mathrm{Re}}{15}\left(\frac{U_W^2}{h_w} - \frac{6}{h_w^3}\right) - \frac{\sin\beta}{\cos\left(\alpha+\beta\right)}\right]\sin\phi_w \\ &\quad + \left[\frac{1}{h_w^3} - \frac{U_W}{h_w^2} + \frac{\cos\beta}{\cos\left(\alpha+\beta\right)}\right]\cos\phi_w,\end{aligned} \tag{2.34}$$

$$\frac{\mathrm{d}x_w}{\mathrm{d}s} = \cos\phi_w. \tag{2.35}$$

The inflow and outflow boundary conditions, in arc-length coordinates are

$$\frac{\kappa_s}{\cos\phi_s} - 2\lambda_{r,s}\tan\phi_s + \left(\lambda_{r,s}^2 + \lambda_{i,s}^2\right)\left(h_s - 1\right) = 0 \quad \text{at slide inflow} \tag{2.36}$$

$$\tan\phi_w - \lambda_{r,w}\left(h_w - \frac{h_\infty}{h_0}\right) = 0 \quad \text{at web outflow} \tag{2.37}$$

$$\frac{\kappa_w}{\cos\phi_w} - \lambda_{r,w}^2\left(h_w - \frac{h_\infty}{h_0}\right) = 0 \quad \text{at web outflow} \tag{2.38}$$

In addition of those boundary conditions, three matching conditions, equations (2.25), (2.26), and (2.27) are also imposed at the slide outflow and web inflow to close the system.

2.2.5 Solution Method

Both film profile equations written in terms of arc-length coordinates take the form of a system of four coupled first-order ODE'S, one of which is non-linear. The system was discretized by a second-order finite difference method at interior nodes. Centered difference stencil was employed at interior nodes and backward/forward difference stencil was used at the boundary and matching nodes of each region. The resulting nonlinear algebraic system of equation was solved by Newton's method.

The mesh was graded in the highly curved region, i.e. at the vicinity of matching region, in order to capture the steep gradient in thickness profile and to reduce computation effort. The mesh was graded with appropriate one-dimensional stretching functions compiled by Vinokur (1983) and de Santos (1991).

At the slide region, the nodes are concentrated at the matching point, i.e. $\xi_s = N_s$ and the stretching function employed is

$$s\left(\frac{\xi_s}{N_s}\right) = \frac{\tanh\ \left(A_s \frac{\xi_s}{N_s}\right)}{\tanh A_s} \tag{2.39}$$

where A_s represent the strength of node concentration at $\xi_s = N_s$. If the spacing at $\xi_s = N_s$ is specified (ΔS_{N_s}), A_s must satisfy

$$\sinh 2A = \frac{2A}{N \Delta S_{N_s}}. \tag{2.40}$$

Similarly, the nodes at the web region are concentrated at the matching point, i.e. $\xi_w = 0$ and the stretching function employed is

$$s\left(\frac{\xi_w}{N_w}\right) = 1 + \frac{\tanh\ \left[A_w \left(\frac{\xi_w}{N_w} - 1\right)\right]}{\tanh A_w} \tag{2.41}$$

where A_w represent the strength of node concentration at $\xi_w = 0$. If the spacing at

$\xi_w = 0$ is specified (ΔS_0), A_w must satisfy

$$\sinh 2A_w = \frac{2A_w}{N_w \Delta S_0}. \tag{2.42}$$

The domain lengths were set at $15h_0$ and $5h_0$ for slide and web regions respectively. The numbers of nodes deployed were 150 and 100 for slide and web regions respectively. The effect of these arbitrary choices of domain lengths on the solution is discussed next.

2.3 Results

2.3.1 Effect of Domain Length

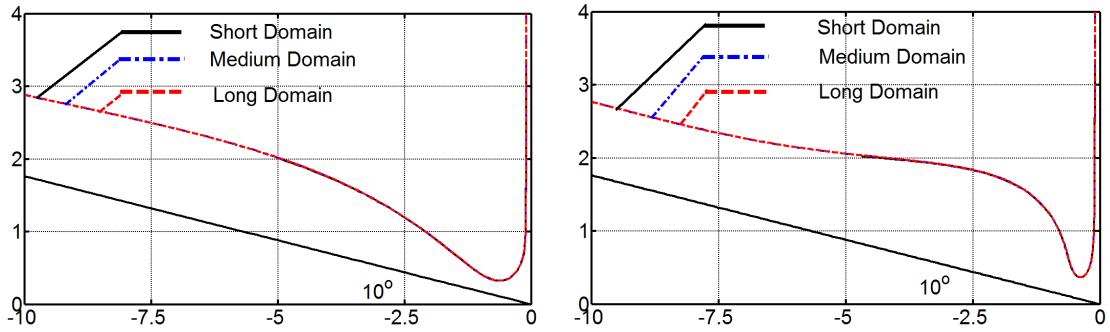

(a) Ca = 0.01 Re = 0. (b) Ca = 0.1 Re = 10.

Figure 2.4: Effect of domain length - $\alpha = 80^o, \beta = 0^o, U_W = 10$.

Imposing inflow and outflow boundary conditions as Robin boundary conditions permits the domain of calculation to be shorter than when Dirichlet and Neumann boundary conditions are imposed and the level of accuracy of the approximation is fixed Bixler (1982). However, the domain length chosen has to be long enough such that the computed solution is insensitive to the arbitrary location of the synthetic flow boundaries. In this study, the sensitivity of the slide and web domain lengths, pa-

rameterized as a total arc length along the free surface, S_S and S_W, was tested on slide - web inclination and flow parameter sets that are representative of actual coating operations. The slide and web inclinations were set at 10^o and 90^o from horizontal respectively, as depicted in Fig. 2.4. The sensitivity analysis was done at two cases, low capillary number with zero inertia, Ca = 0.01 and Re = 0, and moderate capillary and Reynolds numbers, Ca = 0.1 and Re = 10. The three domain lengths tested were:

- Short: $S_S = 5h_0$; $S_W = 3h_0$
- Medium: $S_S = 15h_0$; $S_W = 5h_0$
- Long: $S_S = 30h_0$; $S_W = 10h_0$

Nodes were distributed uniformly along the free surface of the domain, 20 nodes per unit arc-length along the slide and web, so that the distribution was invariant as the domain length was changed. The computed film thickness profiles with each domain length are presented in Figure 2.4.

The solutions are virtually the same for the cases tested, even for the case of flow with inertia and higher capillary number, which is expected to require longer domain length due to the presence of a standing wave near the matching point. The domain length chosen for the analysis presented from now on was slide domain of 15 h_0 and web domain of 5 h_0.

2.3.2 Effect of Mesh

The sensitivity of the solution to the level of discretization, i.e. the numbers of nodes used, was tested at the same parameters used to test the effect of domain length, i.e. , Ca = 0.01 and Re = 0, and, Ca = 0.1 and Re = 10. The analysis was done for three different number of nodes for the slide flow N_s and the web flow N_w:

- $N_s = 75$ and $N_w = 50$

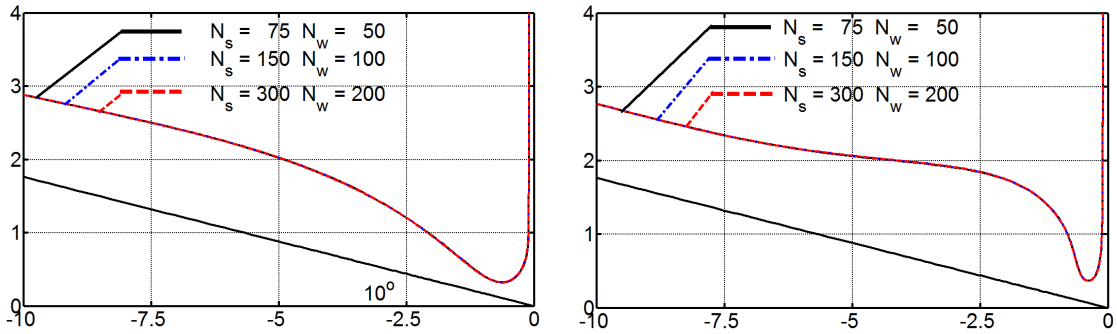

(a) Ca = 0.01 Re = 0.

(b) Ca = 0.1 Re = 10.

Figure 2.5: Effect of mesh - $\alpha = 80^o, \beta = 0^o, U_W = 10$.

- $N_s = 150$ and $N_w = 100$
- $N_s = 300$ and $N_w = 200$

The computed thickness profiles are presented in Fig. 2.5. The solutions are insensitive to the mesh at both set of parameters. The results presented from now on were obtained using $N_s = 150$ and $N_w = 100$.

2.3.3 Effect of Matching Conditions Assignments

In order to impose boundary and matching conditions in the finite difference approximation of the film profile equations, some of the residual equations that come from the discretized ODE at the nodes located at inflow, outflow, and matching points have to be replaced by boundary and matching conditions. Matching the thickness, slope, and curvature requires three conditions that can be assigned to replace three out of six finite difference equations at the matching nodes of a combined slide and web domains and there are several ways to do that.

To test the sensitivity of the solutions to the different ways of imposing matching conditions, we performed numerical experiment on a base case: Ca = 0.01, Re = 0, $U_W = 10$, at slide-web folding angle $\alpha = 80^o$ and web angle $\beta = 0^o$. The nodes

are concentrated near the matching point with appropriate stretching functions as mentioned in Section 2.2.5. Three matching conditions assignment tested and their illustration is presented in Fig. 2.6; they were :

- Matching Assignment 1. Inclination and curvature matching conditions, equations (2.26) and (2.27), are imposed in the matching node of the slide flow domain by replacing finite difference approximations of equations (2.29) and (2.30) (ODEs for the free surface inclination and curvature) respectively. Thickness matching condition, equation (2.25), is imposed in the matching node of the web flow domain by replacing the finite difference approximation of equation (2.32) (ODE for the film thickness).

- Matching Assignment 2. Thickness matching condition, equation (2.25), is imposed in the matching node of the slide flow domain by replacing the finite difference approximations of equation (2.28) (ODE for the film thickness). Inclination and curvature matching conditions, equations (2.26) and (2.27), are imposed in the first node of the web domain by replacing finite difference approximations of equations (2.33) and (2.34) respectively (ODEs for the free surface inclination and curvature). This is the opposite of the Matching Assignment 1.

- Matching Assignment 3. All matching conditions, i.e. equations (2.25), (2.26), and (2.27), are assigned by replacing the finite difference approximations of equations (2.32), (2.33), and (2.34) in the matching node of the web region.

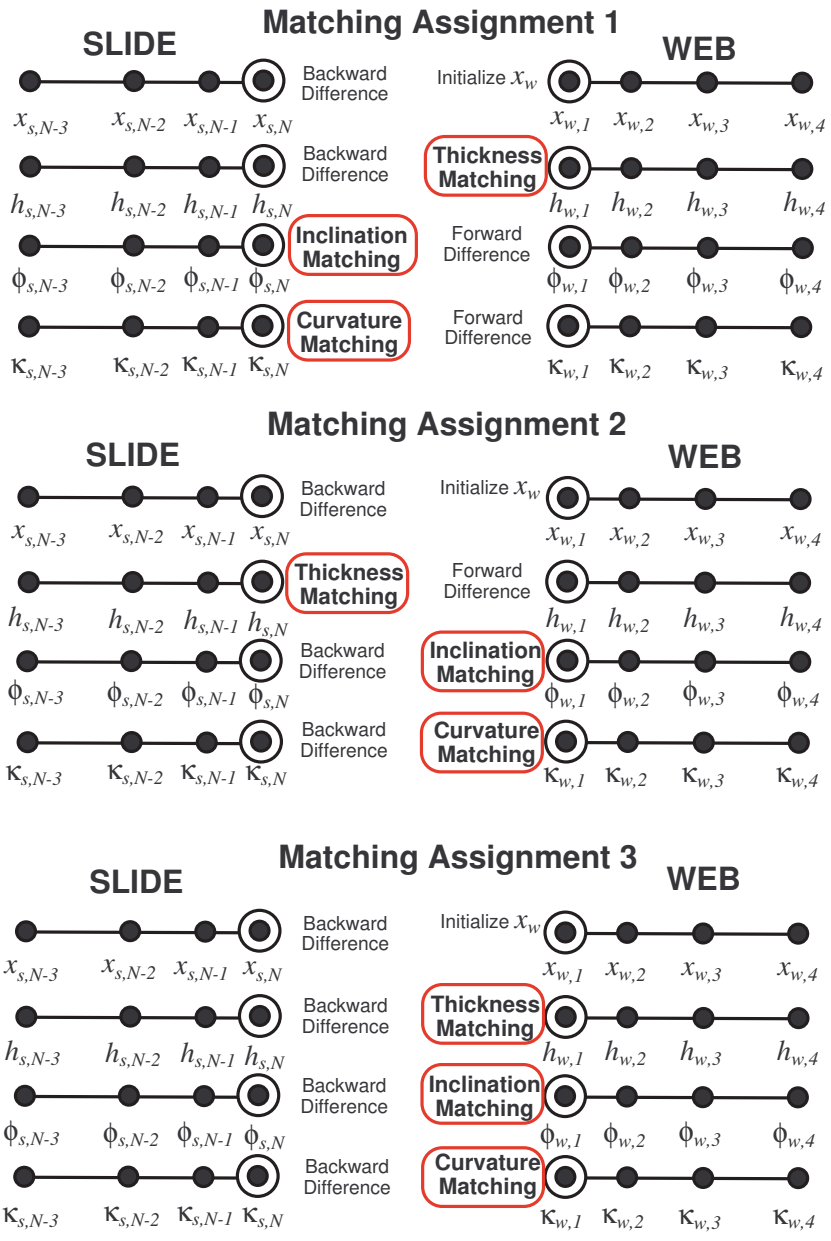

Figure 2.6: Ways of assigning matching conditions I.

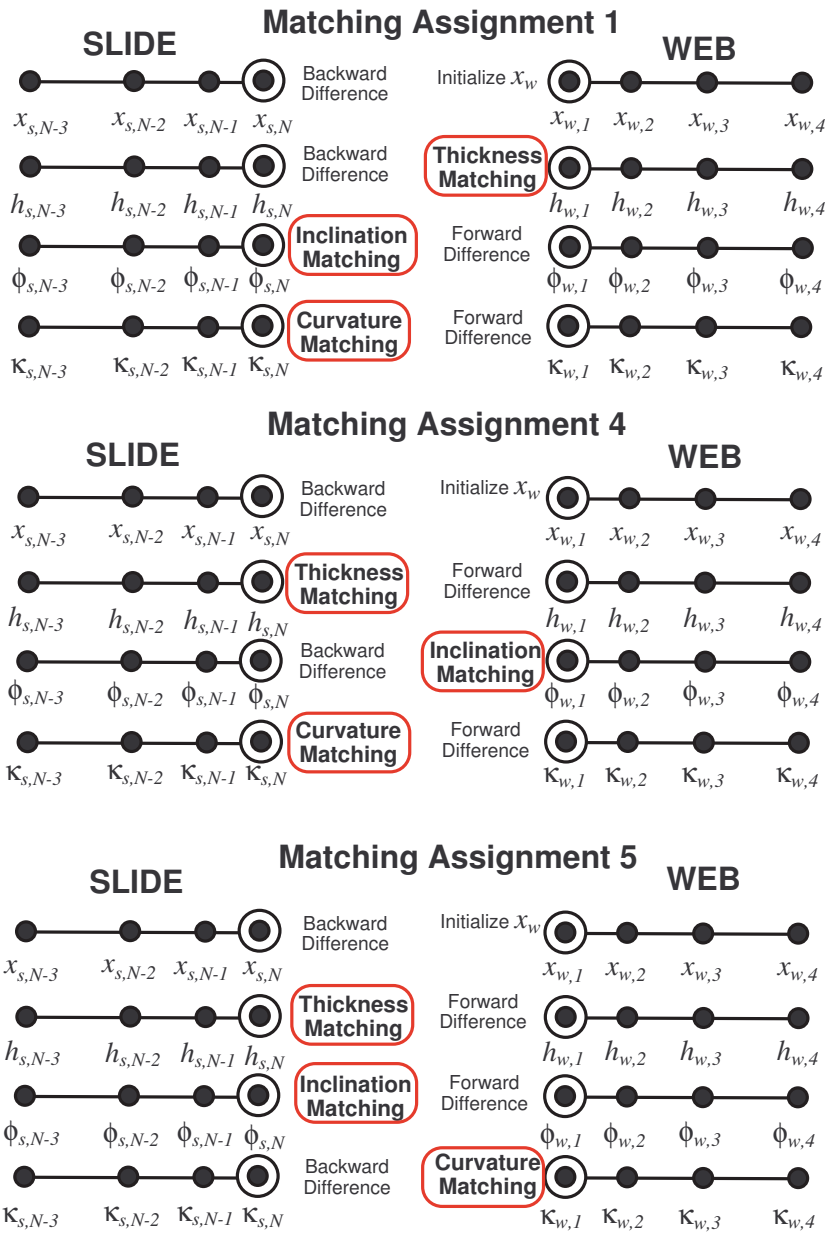

Figure 2.7: Ways of assigning matching conditions II.

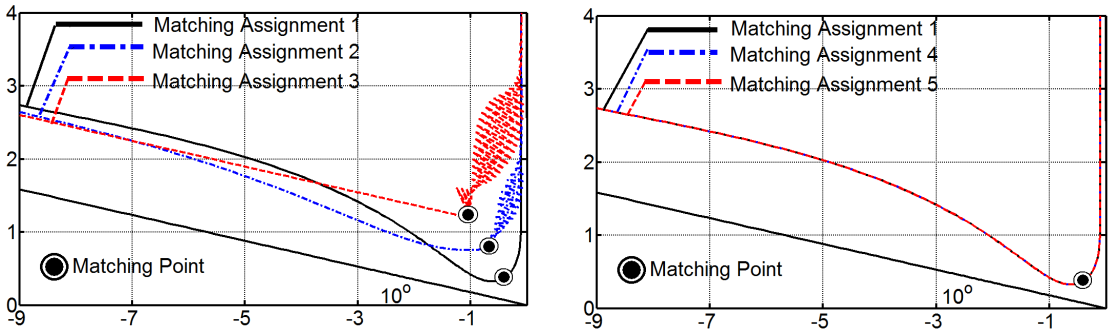

(a) Matching conditions assignment I

(b) Matching conditions assignment II

Figure 2.8: Effect of matching conditions assignments - $\alpha = 80^o$, $\beta = 0^o$, Ca = 0.01, Re = 0, $U_W = 10$.

The computed thickness profiles with each one of the matching condition assignments are shown in Figure 2.8(a). The film profiles obtained with Matching Assignments 2 and 3 present oscillations in the web flow region only. Moreover, wiggles from Matching Assignment 3 have greater amplitudes and are damped at a distance further downstream than the wiggles from Matching Assignment 2. The oscillations arise because the system of equations for the web flow alone becomes overspecified when using more than one matching condition. Moreover, the wiggles become more severe as the equation system is further constrained, as it happens with Matching Assignment 3. The film profile equation of the web flow is a third-order ODE and it already has two outflow boundary conditions, equations (2.23) and (2.24). In order to make the system well-posed, only one additional condition is needed and that is provided by one matching condition. Imposing more than one matching condition, in addition to the already specified two outflow boundary condition, will be analogous to imposing more than three boundary conditions to a third-order ODE and the system becomes overspecified. The excessive constraints then produce an oscillatory solution, as shown in Fig. 2.8(a), in order to satisfy all of the imposed conditions at the domain boundaries.

Nevertheless, Matching Assignment 1 is not a unique working combination. A second set of matching condition assignments, illustrated in Fig. 2.7, were tested and the

computed thickness profiles are shown in Fig. 2.8(b). In the schemes 4 and 5, just as in Matching Condition 1, two matching conditions are imposed on the slide flow and one matching condition is imposed on the web flow. What differs is the differential equations that is sacrificed and what matching condition is used. All assignment schemes shown in Figure 2.7 do not overspecify the equation system on the slide nor the web. As expected, they all yielded solutions without oscillations.

The main conclusion is that although the system of equations for the slide and web flows are solved simultaneously, it is not enough to satisfy the number of boundary and matching conditions globally. Each set of ODE that describes the flow down the slide and up the web has to have the appropriate number of boundary conditions.

2.3.4 Effect of Matching Location

As described, viscocapillary model of slide coating consists of a model of the flow down the slide and a model of the flow up the web spliced at a chosen matching point by matching conditions. The location of the matching point is arbitrary and it is defined in terms of the angle θ_s specified in the thickness matching condition, equation (2.25). As the angle θ_s falls, the matching location is shifted further upstream the slide. This may have a strong effect on the predicted film thickness profile.

Nagashima (1993, 2004) set the matching point to be along the bisector line, where $\theta_s = \frac{\alpha}{2}$, and never investigated the effects of changing the matching point location on the computed thickness profile. We explored that by comparing predictions at different values of θ_s. The computed thickness profiles are presented in Fig. 2.9.

At low capillary number and vanishing Reynolds number, the effect of the matching point location is weak. The gradient of the curvature of the film profile is small and each term of the film profile equation does not change much as the matching point is translated up or downstream. At higher capillary and Reynolds numbers, the

meniscus is highly curved and the curvature gradient is also high near the matching point. Therefore, changes on the location of the matching point is accompanied by large changes in the magnitude of each term of both film profile equations. The prediction then becomes very sensitive to the location of the matching point, as shown in Figure 2.9b. The effect is more pronounced on the film profile on the slide where a standing wave is formed. Which solution is more accurate can only be determined by comparing all the three profiles with the solution of the complete two-dimension Navier Stokes equation.

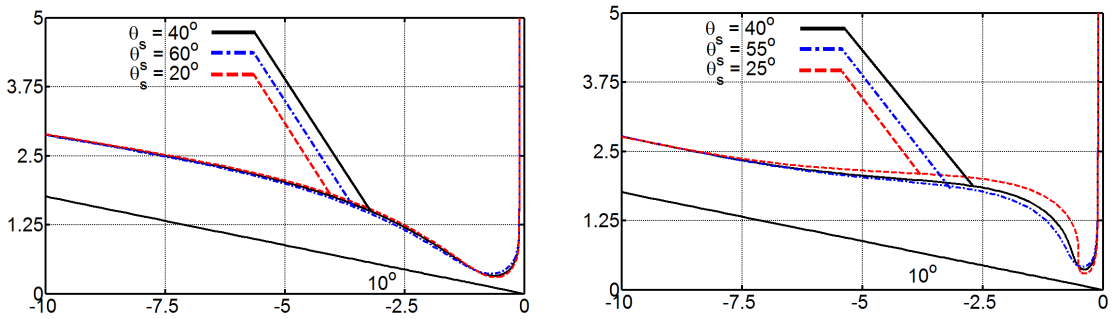

(a) Ca = 0.01, Re = 0. (b) Ca = 0.1, Re = 10.

Figure 2.9: Effect of matching location - $\alpha = 80^o \beta = 0^o$, $U_W = 10$.

2.3.5 Effect of Operating Conditions

What follows is an analysis on how different operating conditions affect the film profile along the slide and web. Changes in free surface configuration may explain important operating limits of slide coating process. For all cases examined here, the matching condition assignment employed is what was referred as Matching Assignment 1 at Section 2.3.3 with the matching location at the bisecting ray between the slide and the web. The parameters that govern the slide coating flow are the capillary number $\text{Ca} = \dfrac{\mu q}{\sigma h_0}$, the Reynolds number $\text{Re} = \dfrac{\rho q}{\mu}$, dimensionless web speed $U_W = \dfrac{V_{\text{web}} h_0}{q}$, and parameters that define the flow geometry.

The evolution of the film profile over the slide and web as the capillary number changes is presented in Fig. 2.10 at Reynolds number Re = 10, dimensionless web speed $U_W = 10$, web inclination with respect to vertical $\beta = 0^o$, and the inclination between slide and web $\alpha = 80^o$. As the capillary number rises, the meniscus near the turnaround region becomes more curved in order to keep the low pressure under the free surface. This low pressure creates an adverse pressure gradient along the web that counter-acts the drag of the upward moving web. The thinner the deposited layer, the higher the adverse pressure gradient needs to be. The capillary number also has a strong effect on the configuration of the standing wave formed on the foot of the slide. Its wavelength increases as the capillary force becomes stronger, i.e. lower capillary number. Consequently, the departure of the film profile from its fully developed value decays slower along the upstream direction.

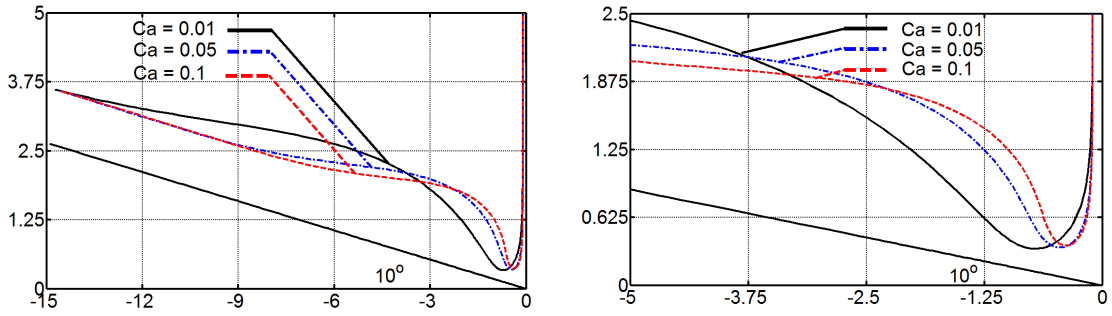

(a) Overall profile.

(b) Bead region.

Figure 2.10: Effect of capillary number - $\alpha = 80^o, \beta = 0^o$, Re = 10 $U_W = 10$.

The effect of Reynolds number, in a range from 0 to 10, at capillary number Ca = 0.01 is shown in Fig. 2.11. The effect on the free surface curvature near the matching point is small. However, as the Reynolds number rises, the adverse pressure gradient necessary to slow down the flow down the slide increases in order to compete with the higher inertial force. Consequently, the amplitude of the standing wave near the bottom of the slide becomes larger.

The thickness of the coated layer falls as the dimensionless web speed rises at a

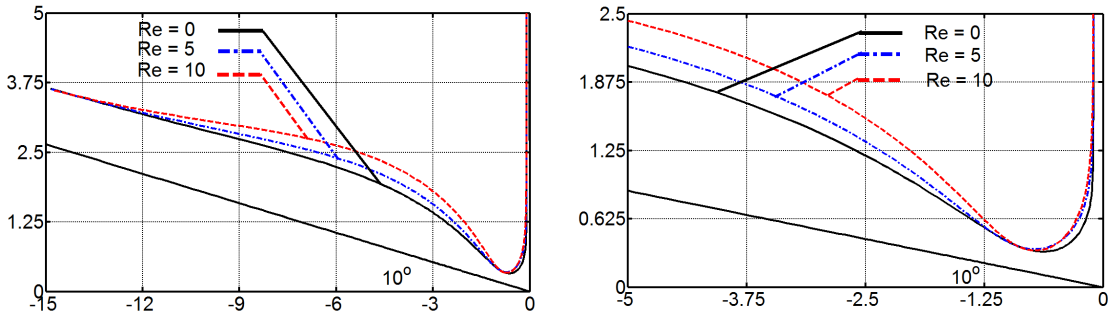

(a) Overall profile.

(b) Bead region.

Figure 2.11: Effect of Reynolds number - $\alpha = 80^o, \beta = 0^o$, Ca $= 0.01$, $U_W = 10$.

constant Reynolds and capillary numbers. Therefore, a stronger adverse pressure gradient along the web is needed to meter the liquid dragged by the moving web. The adverse pressure gradient is created by a lower pressure under the meniscus that becomes more curved as thickness falls, as shown in Fig. 2.12. The thickness of the liquid film under the meniscus also falls, and therefore a higher pressure upstream of the turnaround flow region is needed to keep the flow rate constant. This explains the high amplitude standing wave on the foot of the slide observed at high U_W. The small radius of curvature of the meniscus combined with the large amplitude standing wave may lead to an unstable film profile that would define the maximum dimensionless web speed for stable flow.

Effect of slide and web inclination is shown at Figure 2.13. As the folding angle between slide and web α decreases, the liquid has to make sharper turn, from parallel to the slide surface to parallel to the web surface. The sharp change of the flow direction and the geometric restriction on the meniscus configuration lead to smaller radius of curvature of the free surface near the matching point. The stronger adverse pressure gradient along the web may lead to unstable flow that define the smallest slide-web inclination for stable operation.

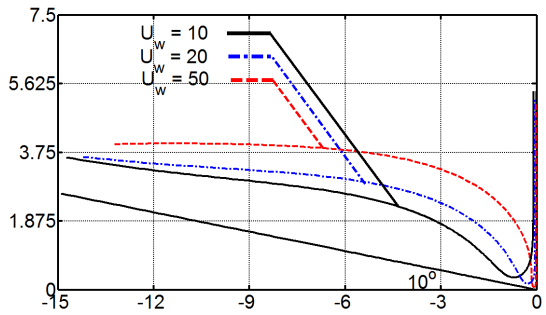

(a) Overall profile.

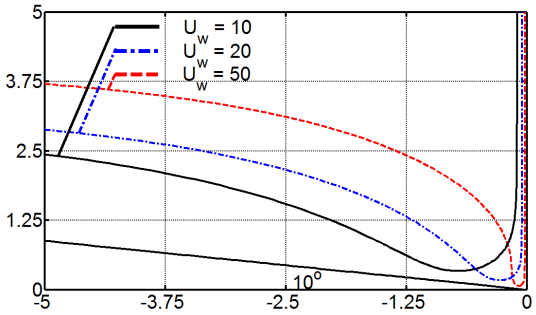

(b) Bead region.

Figure 2.12: Effect of web speed - $\alpha = 80^o, \beta = 0^o$, Ca = 0.01, Re = 10.

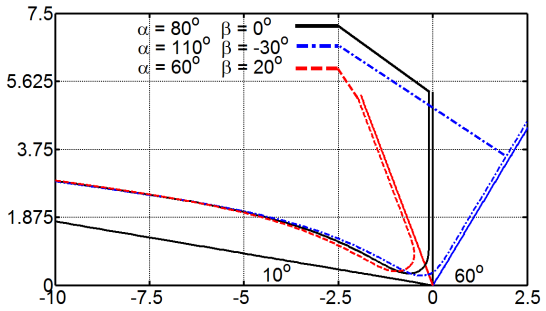

(a) Effect of web inclination - overall profile.

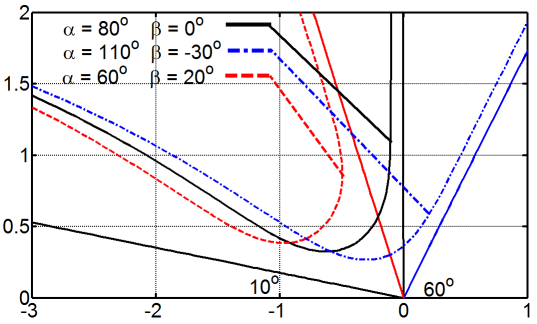

(b) Effect of web inclination - bead region.

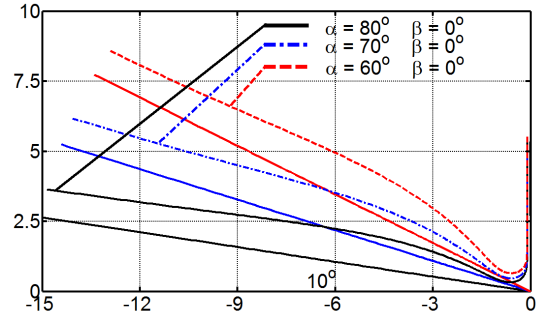

(c) Effect of slide inclination - overall profile.

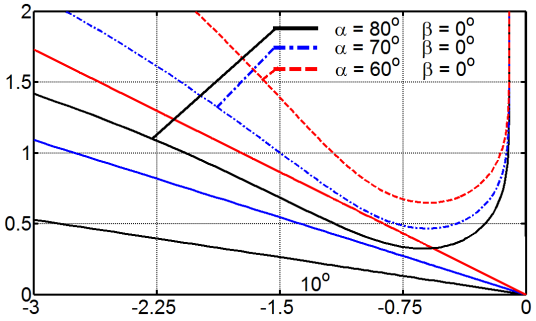

(d) Effect of slide inclination - bead region.

Figure 2.13: Effect of inclination - Ca = 0.01, Re = 0, $U_W = 10$.

2.4 Validation of the Asymptotic Model: Comparison with Solution of the 2D Navier-Stokes

The range of validity of the nonlinear asymptotic model was tested by comparing its prediction of free surface profile with the solution of the full 2-D Navier-Stokes system with the appropriate boundary conditions to account for the free surface.

Because of the free surfaces, the flow domain at each parameter is unknown a priori. In order to solve this free boundary problem by means of standard techniques for boundary-value problems, the set of differential equations and boundary conditions posed in the unknown physical domain is transformed into an equivalent set defined in a known reference domain. This transformation is made by a mapping that connects both domains.

The Navier-Stokes system and the mapping (mesh generation) equations were solved all together by the Galerkin finite-element method. Biquadratic basis functions were used to represent both the velocity and the mapping from the reference to the physical domain. The basis functions used to represent the pressure field were piecewise, linear, and discontinuous. Once all the variables are represented in terms of the basis functions, the system of partial differential equations reduces to simultaneous algebraic equations for the coefficients of the basis functions of all the fields. This set of equations is nonlinear and sparse. It was solved by Newtons method. The linear system of equations at each Newtonian iteration was solved using a frontal solver.

The details of the formulation and solution method are not presented here, but they are similar to the ones used to study slot coating process (Romero et al., 2004) and based on the pioneering work of Christodoulou and Scriven (1989) and de Santos de Santos (1991).

Since the viscocapillary model neglects the presence of the upstream meniscus of slide

coating flow, the comparison only entails the prediction of the top free surface profile. The goal of the comparison was also to determine the appropriate matching point location that connects the slide and web flows. Three different matching locations were used in most of the comparisons presented here.

The solutions obtained with the 1-D viscocapillary model were compared to the full 2-D Navier-Stokes predictions at different capillary and Reynolds numbers for 3 different matching locations. The 2D solutions were obtained with coating gap of 300 μm. At low Reynolds and capillary numbers, Re = 0.3 and Ca = 0.009, Fig. 2.14 (a)-(b), the film thickness profile predicted by both models are similar. As discussed before, at this set of parameters the curvature of the free surface in the turnaround region is small, making the solution almost insensitive to the matching point location. Moreover, all terms of the film profile equations are small near the matching point, making the viscocapillary model accurate. The matching location at $\theta_s = 40^o$ yielded the prediction closest to the full 2-D solutions of the flow. At higher Reynolds number, Re = 7, and same capillary number, Ca = 0.009, Fig. 2.14 (c)-(d), the agreement near the matching is still good, except the profile obtained with $\theta_s = 60^o$. At higher capillary number, Ca = 0.09, Fig. 2.15 (a)-(d), the discrepancy between the computed film thickness profile is large. In this range, predictions obtained with $\theta_s = 60^o$ were the ones closest to the full 2-D solutions. An inappropriate choice of matching point location can lead to highly inaccurate free surface shape, as shown in Fig. 2.15 (d). At higher capillary number, locating the matching point toward the web flow and extending the slide flow film profile solution further downstream improves the accuracy of the viscocapillary model.

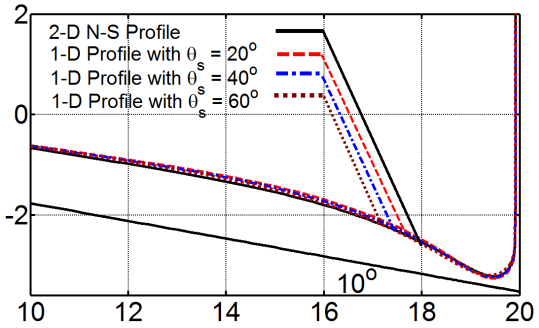

(a) Ca = 0.009 Re = 0.3 Overall profile.

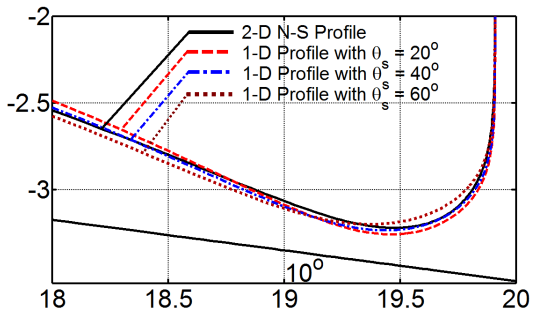

(b) Ca = 0.009 Re = 0.3 Bead region.

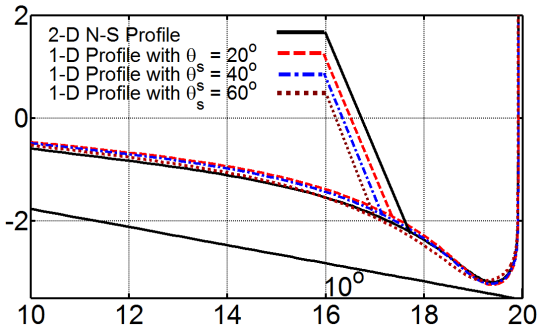

(c) Ca = 0.009 Re = 7 Overall profile.

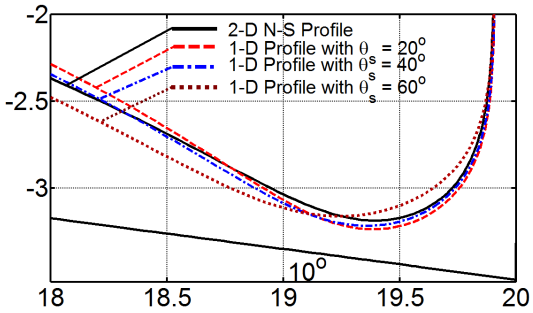

(d) Ca = 0.009 Re = 7 Bead region.

Figure 2.14: Comparison with 2-D N-S profile at different capillary and Reynolds numbers - Part I - $\alpha = 80^o$, $\beta = 0^o$, $U_W = 11$.

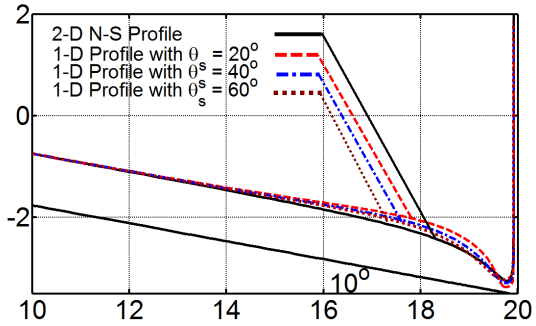

(a) Ca = 0.09 Re = 0.3 Overall profile.

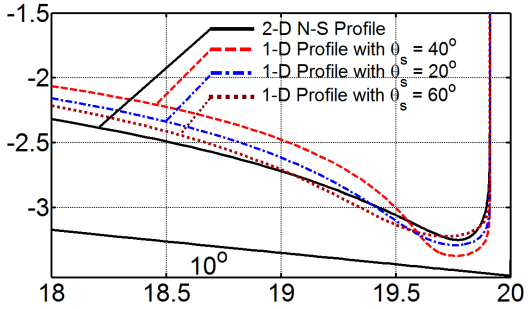

(b) Ca = 0.09 Re = 0.3 Bead region.

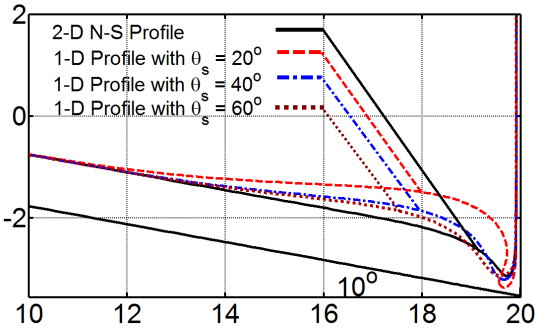

(c) Ca = 0.09 Re = 7 Overall profile.

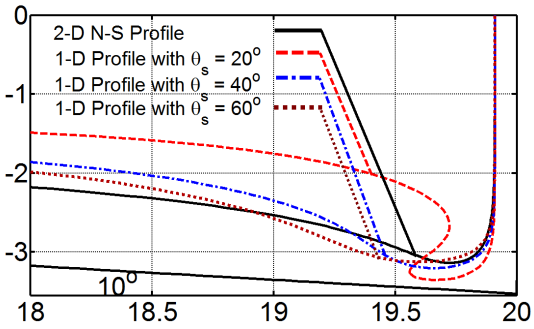

(d) Ca = 0.09 Re = 7 Bead region.

Figure 2.15: Comparison with 2-D N-S profile at different capillary and Reynolds numbers - Part II - $\alpha = 80^o$, $\beta = 0^o$, $U_W = 11$.

Figure 2.16 shows the comparison between 1-D and 2-D predictions at low capillary number, Ca = 0.009, and Re = 7, at different web speeds U_W. As it rises, the film thickness deposited on the web falls and a stronger adverse pressure gradient is needed to meter the flow up the moving web. The 1-D viscocapillary model is able to capture this behavior and the agreement with the predictions from 2-D model is good in the parameter range explored. The smallest relative error was obtained when the matching point location was $\theta_s = 40^o$.

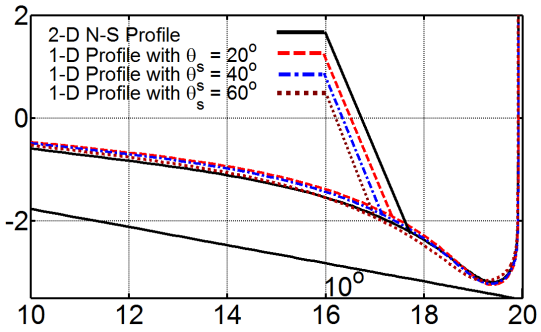

(a) $U_W = 11$ Overall profile.

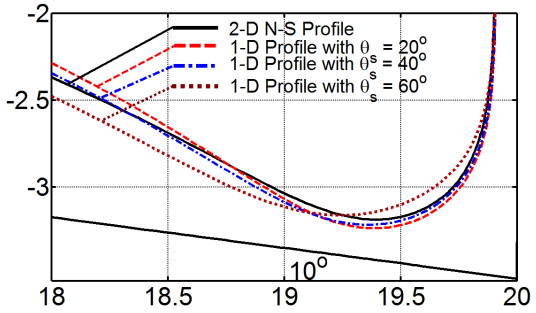

(b) $U_W = 11$ Bead region.

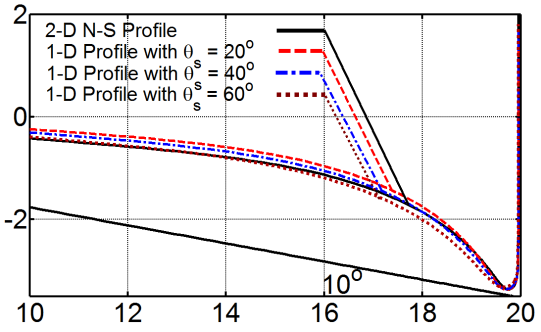

(c) $U_W = 20$ Overall profile.

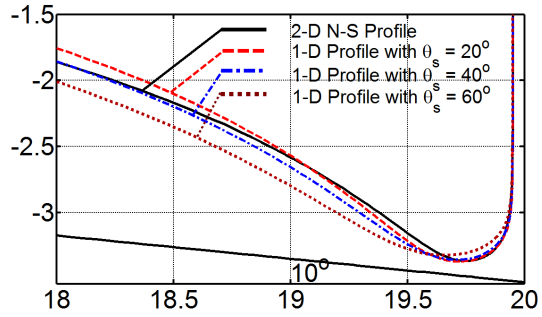

(d) $U_W = 20$ Bead region.

Figure 2.16: Comparison with 2-D N-S profile at different web speed - $\alpha = 80^o$, $\beta = 0^o$, Ca = 0.009, Re = 7.

The effect of the slide and web inclinations on the accuracy of the viscocapillary model is shown in Figs. 2.17 and 2.18. The comparison was done at Ca = 0.009, Re = 7, and $U_W = 11$. The agreement is satisfactory over the range of inclinations explored. It is clear, however, that the accuracy of the 1-D model improves as the angle between the

slide and the web rises. At larger angles, as presented in Fig. 2.17(a)-(b), the radius of curvature of the meniscus is large and consequently sub-ambient pressure under the meniscus is low, leading to the smaller pressure gradient down the slide and up the web.

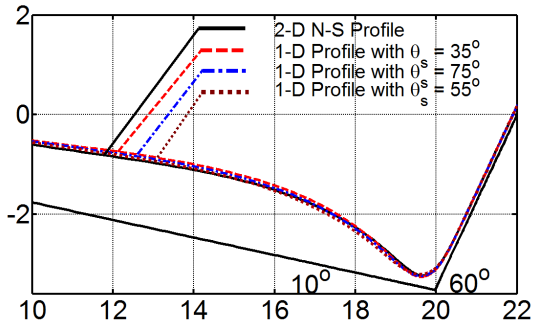

(a) $\alpha = 110^o$, $\beta = -30^o$ Overall profile.

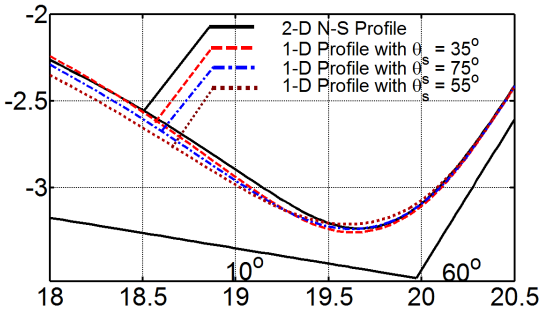

(b) $\alpha = 110^o$, $\beta = -30^o$ Bead region.

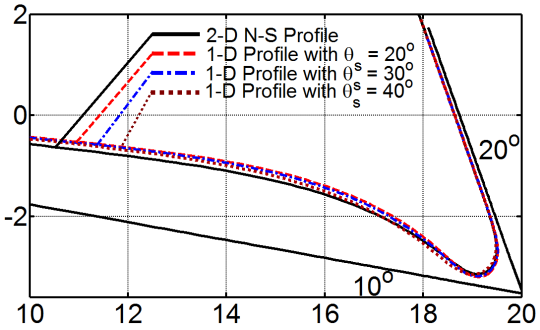

(c) $\alpha = 60^o$, $\beta = 20^o$ Overall profile.

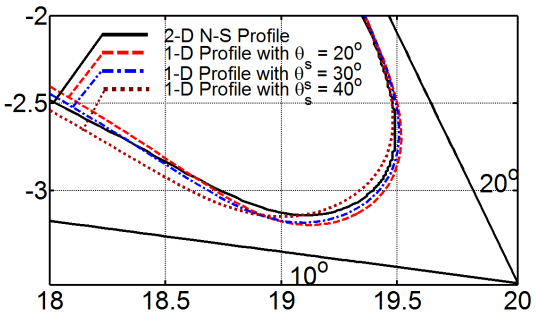

(d) $\alpha = 60^o$, $\beta = 20^o$ Bead region.

Figure 2.17: Comparison with 2-D N-S profile at different web inclinations - Ca = 0.009, Re = 7, $U_W = 11$.

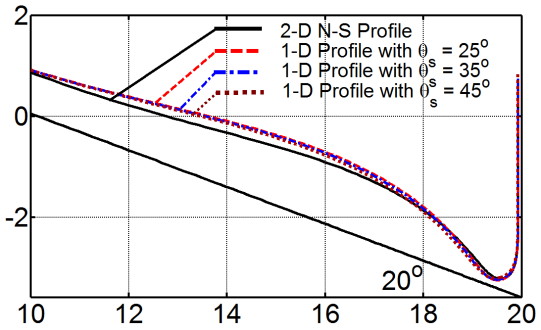

(a) $\alpha = 70^o$, $\beta = 0^o$ Overall profile.

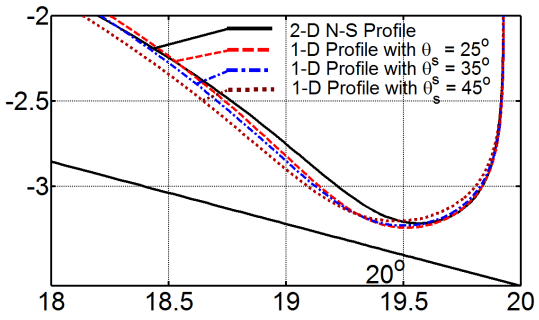

(b) $\alpha = 70^o$, $\beta = 0^o$ Bead region.

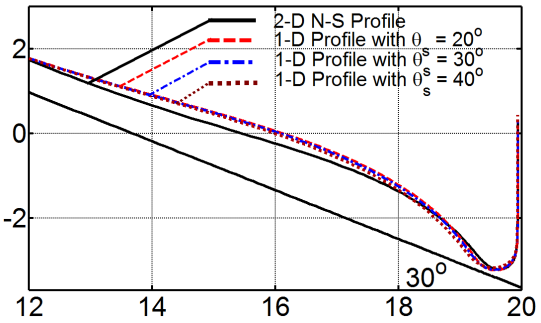

(c) $\alpha = 60^o$, $\beta = 0^o$ Overall profile.

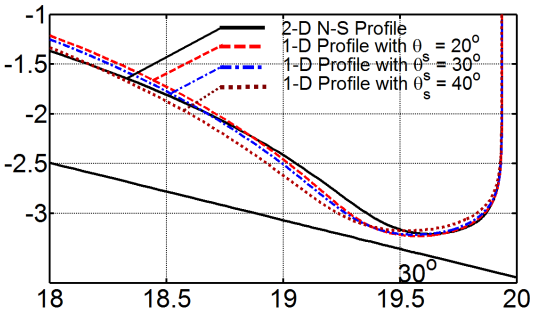

(d) $\alpha = 60^o$, $\beta = 0^o$ Bead region.

Figure 2.18: Comparison with 2-D N-S profile at different slide inclinations - Ca = 0.009, Re = 7, $U_W = 11$.

The comparison between the 1-D viscocapillary model's prediction and 2-D Navier-Stokes theory's was also performed at different slide-web gap to check the range at which the 1-D model, which does not take the gap into account, is valid. Due to the lack of gap as a parameter in the viscocapillary model and in order to make a fair comparison, the computed thickness profiles from 2-D Navier-Stokes theory at different gaps were translated along the slide surface such that the thickness profile on the web overlap one another. Figure 2.19 shows the free surface profile obtained with the viscocapillary model and with the full 2-D Navier-Stokes model at 3 different gaps, covering the range from $3.3h_\infty$ to $9.0h_\infty$ at Ca = 0.009, Re = 7, and $U_W = 11$. If the gap is small enough, the 2-D solution is virtually insensitive to this parameter, and the 1-D predictions agree with the full 2-D Navier-Stokes solutions. At larger

gaps, the coating bead can no longer be treated as a liquid pool and the meniscus tends to curve toward the gap. In this case, the 1-D predictions are not accurate and the viscocapillary model is not valid. This result shows that the use of viscocapillary model should be limited to cases at which the gap-to-thickness ratio is less than approximately 6.0.

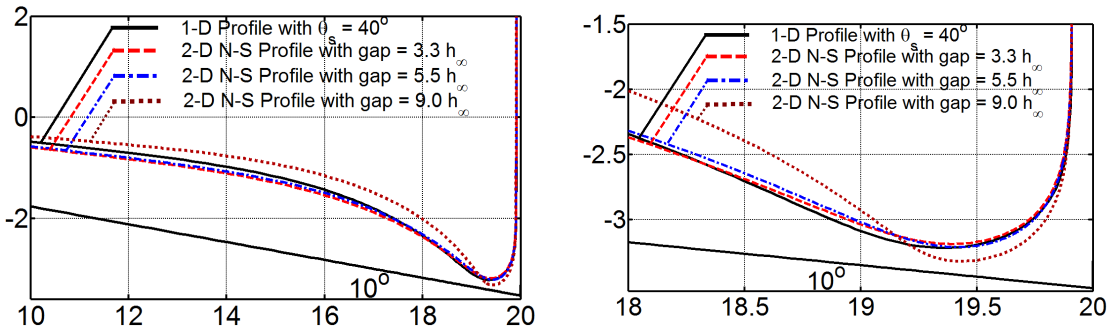

(a) Overall profile.

(b) Bead region.

Figure 2.19: Comparison with 2-D N-S profile at different gap - $\alpha = 80^o$, $\beta = 0^o$,Ca = 0.009, Re = 7, $U_W = 11$.

2.5 Conclusion

A critical review of the available viscocapillary model is presented. We improve on the more accurate available model by writing it in terms of an arc-length coordinate along the free surface and by making the matching location adjustable. We have demonstrated that with the appropriate formulation, a simplified 1-D viscocapillary model of slide coating can be constructed and its range of validity are governed by the limitation of the approximations employed: Small inclination of film thickness, low capillary number, and low Reynolds number. The approximation worsen at the bead zone, as expected, where in the 1-D viscocapillary model it was assumed to be a static pool and in a realistic coating operation, it is not so. The results show that viscocapillary model are accurate only at low capillary numbers and small gap-to-thickness ratio.

Based on our observations, we conclude that a 1-D slide coating model that can be applied at high capillary and Reynolds number can not be derived. The reason is that the flow in the bead region is far from a static pool. We propose an efficient model by inserting N-S theory at a suitably defined bead region to link the film profile equations down the slide and up the web. The hybrid model is the most efficient approach to study slide coating flows and the operating limits of the process. It takes advantage of the asymptotic model where it is valid and relies on the full 2-D model where the flow is far from rectilinear. This model is discussed in Chapter 3.

Chapter 3

Hybrid Model of Slide Coating

3.1 Introduction

Slide coating is widely used for applying multilayer of thin liquids simultaneously onto a substrate or web. The thickness of the coated layer is set solely by flow rate and web speed. However, at certain operating conditions, the layer is not uniform, or even fail to coat. It is crucial to determine the window of operability in the parameter space where uniform coating can be obtained. Theoretical modeling can be a valuable tool in predicting the operability window of slide coating process.

Theoretical modeling of slide coating had been performed, ranging from lubrication approximation based analysis that leads to viscocapillary model (Nagashima, 1993, 2004; Tjiptowidjojo and Carvalho, 2009) to solution of full 2-D Navier-Stokes equation (Christodoulou and Scriven, 1989). In Chapter 2, we present critical examination of the viscocapillary model and identify the conditions where the model's prediction is no longer accurate. The model's inadequacy at those conditions is due to limitations set by ad-hoc hypotheses used in constructing the model. In conclusion, the model accuracy can be significantly improved by describing the flow in the coating bead region by the full 2-D Navier-Stokes equation.

Coupling of one-dimensional approximation model with a two-dimensional description has been employed in coating flow analysis. Some examples of the models are presented in Fig. 3.1. Kistler (1984) combined full 2-D Navier-Stokes in the film forming zone, right after takeoff from the die, to a 1-D viscocapillary model of flow developing zone, right before the curtain, in his curtain coating. He was able to determine how upstream condition in the flow forming zone affected the flow developing into the curtain. Stay and Barocas (2003) combined full 2-D Stokes flow and 1-D lubrication flow equations to model fully-submerged roll coating flow. The 1-D lubrication model was applied at the thin narrow region, i.e. the nip between 2 rolls, and it was sandwiched in between by wider region, where 2-D Stokes equation was applied to describe the flow at the rest of the domain. They reported a significant speed up in computation time than when the whole region was modeled as 2-D Stokes flow. Park (2008) also employed similar philosophy as Stay and Barocas (2003) did in his tensioned-web over slot die coating model where he interposed the 2-D Navier-Stokes region in between two 1-D elastoviscocapillary models.

This work presents an improved slide coating model where the viscocapillary models presented in Chapter 2 is augmented by the two-dimensional Navier-Stokes system in the coating bead region. In this study, we explore multiple combinations of number and types of matching conditions needed for stitching these regions together and examine their effects on the predictions of free surface shape, pressure fields, and streamlines as well as the effect of changing matching locations. The model is then validated by comparing the predictions to the solution of the full two-dimensional Navier-Stokes.

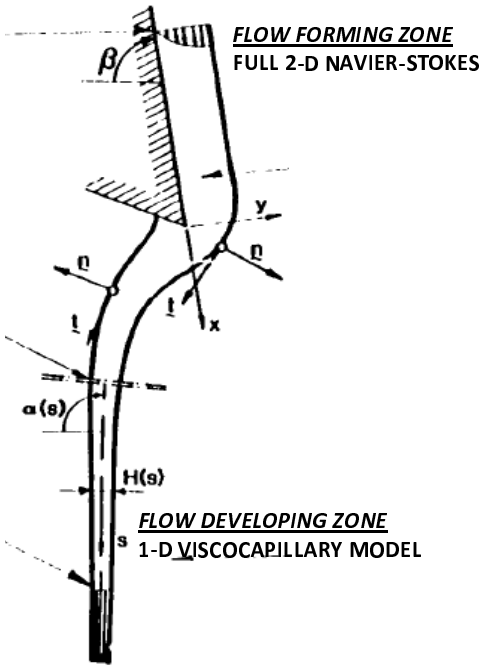

(a) Kistler (1984).

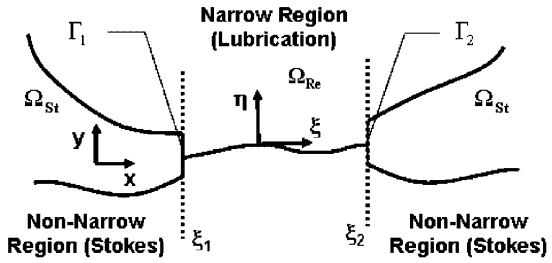

(b) Stay and Barocas (2003).

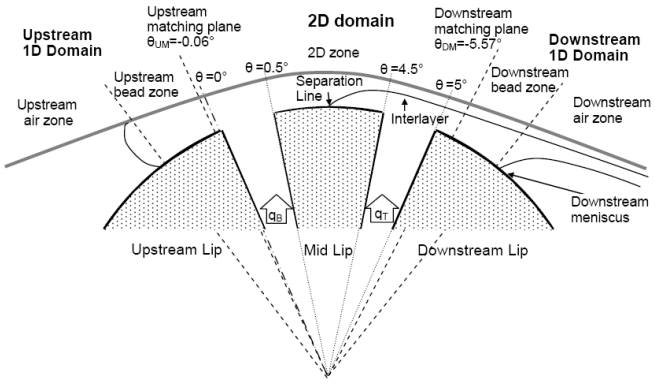

(c) Park (2008).

Figure 3.1: Hybrid models of coating flows.

3.2 The Model

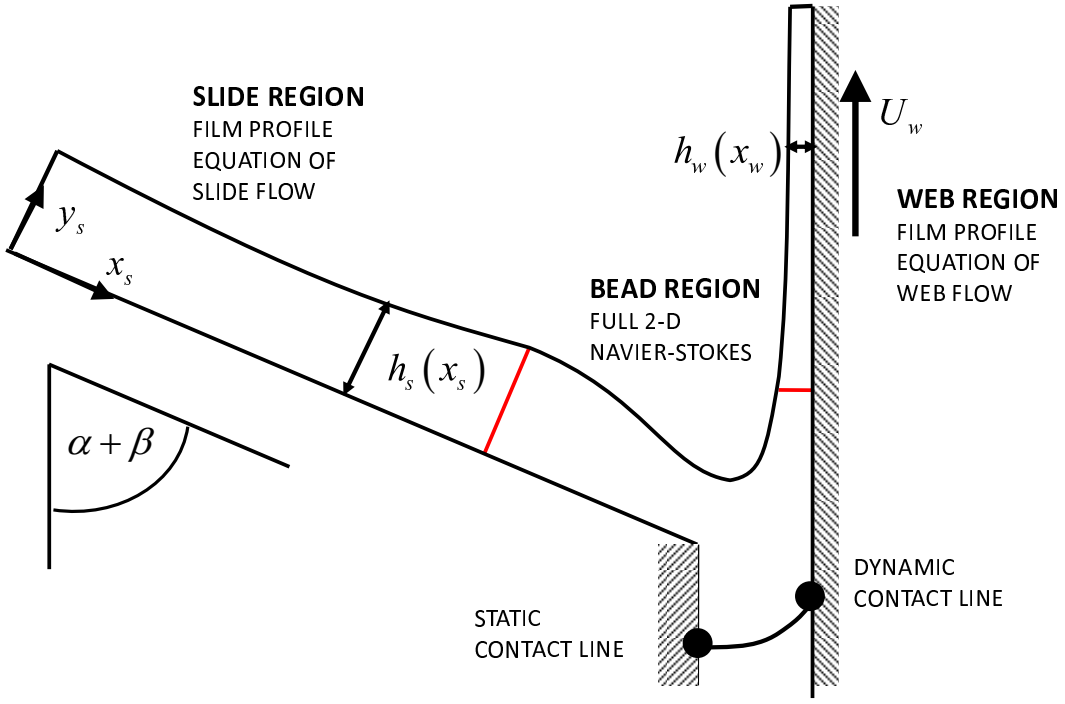

Figure 3.2: Hybrid model of slide coating

The flow domain is divided in three regions, the slide, the bead, and the web regions, as depicted in Fig. 3.2. Flows down the slide and up the web are described with film profile equation that governs the evolution of film thickness along a solid surface. The derivation of film profile equations is discussed by Nagashima (1993, 2004); Tjiptowidjojo and Carvalho (2009) At the flow turnaround region, the film profile equations does not describe the flow well, which is then described with full 2-D Navier-Stokes theory, where now the velocity and pressure have to be solved as well in addition to the free surface profile. The predictions obtained in each region need to be connected to predictions of the adjacent regions. The governing equation and boundary or matching conditions employed for each region is discussed in the following section.

3.2.1 Governing Equations

Slide Region

The film profile equations of slide flow, written in the arc-length coordinate s along the free surface are (Tjiptowidjojo and Carvalho, 2009)

$$\left.\begin{aligned} \frac{\mathrm{d}h_s}{\mathrm{d}s} - \sin\phi_s &= 0 \\ \frac{\mathrm{d}\phi_s}{\mathrm{d}s} - \kappa_s &= 0 \\ \sigma\frac{\mathrm{d}\kappa_s}{\mathrm{d}s} - \left[\rho\frac{6}{5}\frac{q^2}{{h_s}^3} + \rho g\sin(\alpha+\beta)\right]\sin\phi_s & \\ - \left[\mu\frac{3q}{{h_s}^3} - \rho g\cos(\alpha+\beta)\right]\cos\phi_s &= 0 \\ \frac{\mathrm{d}x_s}{\mathrm{d}s} - \cos\phi_s &= 0 \end{aligned}\right\} \tag{3.1}$$

x_s is the coordinate along the slide surface, h_s, ϕ_s, and κ_s are the film thickness, inclination, and curvature respectively. q is the volumetric flow rater per unit width of the liquid with density ρ, viscosity μ, and surface tension σ. The slide inclination is $\alpha + \beta$, measured counterclockwise from the direction of gravity.

The possible boundary or matching conditions include the combination of specification of the film thickness or the slope or the curvature at the inflow boundary or the matching between those at the matching plane. The outflow plane of the slide region is the inflow plane of the bead region and the conditions imposed in this plane are called matching conditions. Three boundary or matching conditions are needed for a well-posed equation system at this region.

Web Region

The film profile equations of web flow, written in the arc length coordinate along the free surface, are (Tjiptowidjojo and Carvalho, 2009)

$$\left.\begin{aligned} \frac{\mathrm{d}h_w}{\mathrm{d}s} - \sin\phi_w &= 0 \\ \frac{\mathrm{d}\phi_w}{\mathrm{d}s} - \kappa_w &= 0 \\ \sigma\frac{\mathrm{d}\kappa_w}{\mathrm{d}s} - \left[\frac{\rho}{5}\left(\frac{{U_w}^2}{h_w} - 6\frac{q^2}{{h_w}^3}\right) - \rho g\sin(\beta)\right]\sin\phi_w & \\ + \left[3\mu\left(\frac{U_w}{{h_w}^2} - \frac{q}{{h_w}^3}\right) - \rho g\cos(\beta)\right]\cos\phi_w &= 0 \\ \frac{\mathrm{d}x_w}{\mathrm{d}s} - \cos\phi_w &= 0 \end{aligned}\right\} \tag{3.2}$$

x_w is the coordinate along the web surface, h_w, ϕ_w, and κ_w are film thickness, inclination, and curvature respectively. The web is positioned at an inclination of β, measured counterclockwise from the direction of gravity. Just as in slide flow region, the film profile of the web flow is also requires three boundary or matching conditions at the matching plane and the outflow boundary.

Bead Region

At the bead region, full 2-D Navier-Stokes theory is applied here. The steady momentum and continuity equations are

$$\rho\mathbf{u}\cdot\nabla\mathbf{u} = \rho\mathbf{g} + \nabla\cdot\mathbf{T} \quad \text{and} \quad \nabla\cdot\mathbf{u} = 0 \tag{3.3}$$

$\mathbf{u}$ is the liquid velocity, $\mathbf{T} = -p\mathbf{I} + \mu\left[\nabla\mathbf{u} + (\nabla\mathbf{u})^{\mathrm{T}}\right]$ is the total stress tensor and p is pressure.

At the wall of slide and the web, no slip boundary condition applies: $\mathbf{u} = \mathbf{0}$ at slide surface and $\mathbf{u} = U_w \mathbf{t}_w$ at the web surface, where U_w is the web speed. The static contact line is allowed to move along the slide die face with prescribed contact angle θ_s. The dynamic contact line in the coating bead is allowed to move along the web with a prescribed contact angle θ_w and the Navier slip condition

$$\frac{1}{\beta_{\text{slip}}} \mathbf{t}_w \cdot (\mathbf{u} - U_w \mathbf{t}_w) = \mathbf{t}_w \mathbf{n}_w : \mathbf{T} \tag{3.4}$$

is imposed to alleviate the singularity there (Huh and Scriven, 1971)

Along the free surface, the force balance and kinematic condition apply:

$$\mathbf{n} \cdot \mathbf{T} = \sigma \frac{\mathrm{d}\mathbf{t}}{\mathrm{d}s} - \mathbf{n} p_{\text{amb}} \quad \text{and} \quad \mathbf{n} \cdot \mathbf{u} = 0 \tag{3.5}$$

σ is the liquid surface tension, s is arc length coordinate along the free surface, and p_{amb} is the ambient pressure and set to zero.

Due to the free surface, the flow domain is unknown apriori. This free boundary problem can be solved by transforming the equations to an equivalent set defined in a known reference domain. The transformation is performed by a mapping $\mathbf{x} = \mathbf{x}(\boldsymbol{\xi})$ to connect these two domains. This work used the mapping scheme presented by de Santos (1991) and Benjamin (1994). They proposed a pair of elliptic differential equations identical to the ones encountered in diffusional transport process with variable diffusion constant to govern the inverse of mapping, i.e. $\boldsymbol{\xi} = \boldsymbol{\xi}(\mathbf{x})$:

$$\nabla \cdot (\mathrm{D}_\xi \nabla \xi) = 0 \quad \text{and} \quad \nabla \cdot (\mathrm{D}_\eta \nabla \eta) = 0 \tag{3.6}$$

where D_ξ and D_η are diffusion-like coefficients used to control element spacing. The appropriate boundary conditions for these inverse mapping equations are specifications of solid surface geometry as well as in the matching planes. Stretching functions

compiled by Vinokur (1983) and de Santos (1991).

Matching of the flows between the 1-D regions; slide and web flow regions; and the 2-D region, bead flow region, requires that the conservation of mass and momentum are satisfied along with continuity of free surface shape. The mass and momentum conservation can be applied either by matching the velocity profile $\mathbf{u}_{\text{2-D}} = \mathbf{u}_{\text{1-D}}$ or the traction $\mathbf{n} \cdot \mathbf{T}_{\text{2-D}}$ at the matching plane. The continuity of free surface can be applied either by matching the film thickness, inclination, or curvature. The greater detail of how the matching conditions were applied is covered in the next section.

3.2.2 Solution Method

The film profile equations and the Navier-Stokes equation system together with the mapping equation were solved with Galerkin/ finite element method. Velocity and the mapping from reference to physical domain were represented with biqudratic basis function ϕ_i and pressure was represented with piecewise linear discontinuous basis function ψ_i. All of the degree of freedom from film profile equations: film thickness, inclination, curvature, and position along the solid surface, are represented with quadratic basis function φ_i:

$$
\begin{aligned}
&u = \sum_{j=1}^{n} u_j \phi_j \quad ; \quad v = \sum_{j=1}^{n} v_j \phi_j \quad ; \quad p = \sum_{j=1}^{m} p_j \psi_j \\
&x = \sum_{j=1}^{n} x_j \phi_j \quad ; \quad y = \sum_{j=1}^{n} y_j \phi_j \\
&h_s = \sum_{j=1}^{k} h_{s,j} \varphi_j \quad ; \quad \phi_s = \sum_{j=1}^{k} \phi_{s,j} \varphi_j \quad ; \quad \kappa_s = \sum_{j=1}^{k} \kappa_{s,j} \varphi_j \quad ; \quad x_s = \sum_{j=1}^{k} x_{s,j} \varphi_j \\
&h_w = \sum_{j=1}^{l} h_{w,j} \varphi_j \quad ; \quad \phi_w = \sum_{j=1}^{l} \phi_{w,j} \varphi_j \quad ; \quad \kappa_w = \sum_{j=1}^{l} \kappa_{w,j} \varphi_j \quad ; \quad x_w = \sum_{j=1}^{l} x_{w,j} \varphi_j
\end{aligned}
$$

The coefficients of the basis functions are the unknowns of the discretized problems

and were solved by requiring the Galerkin weighted residuals to be zero in each region: In the slide region Ω_s, the weighted residuals are :

$$R_i^{h_s} = \int_{\Omega_s} \varphi_i \left\{ \frac{\mathrm{d}h_s}{\mathrm{d}s} - \sin\phi_s \right\} \mathrm{d}\Omega_s \tag{3.7}$$

$$R_i^{\phi_s} = \int_{\Omega_s} \varphi_i \left\{ \frac{\mathrm{d}\phi_s}{\mathrm{d}s} - \kappa_s \right\} \mathrm{d}\Omega_s \tag{3.8}$$

$$\begin{aligned} R_i^{\kappa_s} &= \int_{\Omega_s} \varphi_i \left\{ \sigma \frac{\mathrm{d}\kappa_s}{\mathrm{d}s} - \left[\rho \frac{6}{5} \frac{q^2}{{h_s}^3} + \rho g \sin(\alpha+\beta) \right] \sin\phi_s \right\} \mathrm{d}\Omega_s \\ &\quad - \int_{\Omega_s} \varphi_i \left\{ \left[\mu \frac{3q}{{h_s}^3} - \rho g \cos(\alpha+\beta) \right] \cos\phi_s \right\} \mathrm{d}\Omega_s \end{aligned} \tag{3.9}$$

$$R_i^{x_s} = \int_{\Omega_s} \varphi_i \left\{ \frac{\mathrm{d}x_s}{\mathrm{d}s} - \cos\phi_s \right\} \mathrm{d}\Omega_s \tag{3.10}$$

In the bead region Ω_b, they are:

$$\mathbf{R}_i^M = \iint_{\Omega_b} \left\{ \phi_i \left(\rho \mathbf{u} \cdot \nabla \mathbf{u} - \rho \mathbf{g} \right) + \nabla \phi_i \cdot \mathbf{T} \right\} \mathrm{d}\Omega_b - \int_{\Gamma_b} \phi_i \mathbf{n} \cdot \mathbf{T} \, \mathrm{d}\Gamma_b \tag{3.11}$$

$$R_i^C = \iint_{\Omega_b} \psi_i \nabla \cdot \mathbf{u} \, \mathrm{d}\Omega_b \tag{3.12}$$

$$R_i^x = -\iint_{\Omega_b} D_\xi \nabla \phi_i \cdot \nabla \xi \, \mathrm{d}\Omega_b + \int_{\Gamma_b} \phi_i D_\xi \mathbf{n} \cdot \nabla \xi \, \mathrm{d}\Gamma_b \tag{3.13}$$

$$R_i^y = -\iint_{\Omega_b} D_\eta \nabla \phi_i \cdot \nabla \eta \, \mathrm{d}\Omega_b + \int_{\Gamma_b} \phi_i D_\eta \mathbf{n} \cdot \nabla \eta \, \mathrm{d}\Gamma_b \tag{3.14}$$

In the web region Ω_w, they are:

$$R_i^{h_w} = \int_{\Omega_w} \varphi_i \left\{ \frac{\mathrm{d}h_w}{\mathrm{d}s} - \sin\phi_w \right\} \mathrm{d}\Omega_w \tag{3.15}$$

$$R_i^{\phi_w} = \int_{\Omega_w} \varphi_i \left\{ \frac{\mathrm{d}\phi_w}{\mathrm{d}s} - \kappa_w \right\} \mathrm{d}\Omega_w \tag{3.16}$$

$$\begin{aligned} R_i^{\kappa_w} \;=\; & \int_{\Omega_w} \varphi_i \left\{ \sigma \frac{\mathrm{d}\kappa_w}{\mathrm{d}s} - \left[\frac{\rho}{5} \left(\frac{{U_w}^2}{h_w} - 6\frac{q^2}{{h_w}^3} \right) - \rho g \sin(\beta) \right] \sin\phi_w \right\} \mathrm{d}\Omega_w \\ & - \int_{\Omega_w} \varphi_i \left\{ \left[3\mu \left(\frac{U_w}{{h_w}^2} - \frac{q}{{h_w}^3} \right) - \rho g \cos(\beta) \right] \cos\phi_w \right\} \mathrm{d}\Omega_w \end{aligned} \tag{3.17}$$

$$R_i^{x_w} = \int_{\Omega_w} \varphi_i \left\{ \frac{\mathrm{d}x_w}{\mathrm{d}s} - \cos\phi_w \right\} \mathrm{d}\Omega_w \tag{3.18}$$

The treatment of boundary and matching conditions is described in the following sections

Matching Mass and Momentum Conservation

Mass and momentum matching conditions act as velocity boundary conditions of the bead region. It either can be applied in a similar manner to Dirichlet boundary conditions by specifying both velocity components u and v at the matching plane or in similar manner to Neumann boundary conditions by specifying the traction term $\mathbf{n} \cdot \mathbf{T}$ of residuals (3.11) at the matching plane. Matching velocity components are done by replacing residuals (3.11) with

$$\mathbf{R}_i^M|_{\text{match}} = \mathbf{u}(x,y) - \mathbf{u}_{1-D}(x,y), \tag{3.19}$$

where $\mathbf{u}_{1-D}$, is the velocity profile of the viscocapillary flow at slide or web regions. At the matching plane between the slide and bead region, the velocity profile is :

(Tjiptowidjojo and Carvalho, 2009)

$$\mathbf{t}_s \cdot \mathbf{u}_{1-D} = \frac{3q}{h_s}\left[\frac{y_s}{h_s} - \frac{1}{2}\left(\frac{y_s}{h_s}\right)^2\right] \tag{3.20}$$

$$\mathbf{n}_s \cdot \mathbf{u}_{1-D} = \frac{3q}{h_s}\left(\frac{y_s}{h_s}\right)\left[\frac{y_s}{h_s} - \frac{1}{2}\left(\frac{y_s}{h_s}\right)^2\right]\tan\phi_s \tag{3.21}$$

where q is the volumetric flow rate per unit width, h_s, and ϕ_s are free surface thickness and inclination respectively, which are obtained from solutions of film profile equations of slide flow. Likewise, at the matching plane between the bead and web region, the velocity profile is : (Tjiptowidjojo and Carvalho, 2009)

$$\mathbf{t}_w \cdot \mathbf{u}_{1-D} = \frac{3}{2}\left(U_w - \frac{q}{h_w}\right)\left[\left(\frac{y_w}{h_w}\right)^2 - 2\left(\frac{y_w}{h_w}\right)\right] \tag{3.22}$$

$$\begin{aligned}\mathbf{n}_w \cdot \mathbf{u}_{1-D} &= -3\left(\frac{y_w}{h_w}\right)^2 \tan\phi_w \left[\left(\frac{1}{2}\left(\frac{y_w}{h_w}\right) - 1\right)\frac{q}{h_w}\right] \\ &\quad - \tan\phi_w \left[U_w\left(\frac{1}{3}\left(\frac{y_w}{h_w}\right) - \frac{1}{2}\right)\right]\end{aligned} \tag{3.23}$$

where h_w, and ϕ_w are free surface thickness and inclination respectively, which are obtained from solutions of film profile equations of web flow.

Matching traction is done by substituting

$$\mathbf{n} \cdot \mathbf{T}_{1-D} = -p_{1-D}\mathbf{n} + 2\mu\mathbf{n} \cdot \left[\nabla\mathbf{u}_{1-D} + (\nabla\mathbf{u}_{1-D})^{\mathrm{T}}\right] \tag{3.24}$$

into the residual (3.11) at the matching plane and form the following residual

$$\begin{aligned}\mathbf{R}_i^M|_{\text{match}} &= \iint_{\Omega_b} \left\{\phi_i|_{\text{match}} \left(\rho\mathbf{u} \cdot \nabla\mathbf{u} - \rho\mathbf{g}\right) + \nabla\phi_i|_{\text{match}} \cdot \mathbf{T}\right\} \mathrm{d}\Omega_b \\ &\quad - \int_{\Gamma_b} \phi_i|_{\text{match}} \left\{-p_{1-D}\mathbf{n} + 2\mu\mathbf{n} \cdot \left[\nabla\mathbf{u}_{1-D} + (\nabla\mathbf{u}_{1-D})^{\mathrm{T}}\right]\right\} \mathrm{d}\Gamma_b\end{aligned} \tag{3.25}$$

where $\mathbf{u}_{1-D}$ is defined in equation (3.20) at the slide - bead matching plane or equation (3.22) at the bead - web matching plane, p_{1-D} is the pressure field at the matching plane, which at the slide - bead matching plane is

$$p_{1-D} = \rho g \sin(\alpha + \beta)(h_s - y_s) - \sigma \kappa_s \tag{3.26}$$

and at the bead - web matching plane is

$$p_{1-D} = \rho g \sin\beta (h_w - y_w) - \sigma \kappa_w \tag{3.27}$$

Based on these options, there are 4 possible mass and momentum matching conditions. However, as shown later, only one combination works: The matching velocity condition is applied in the slide - bead matching plane and the matching traction in the bead - web plane.

Matching the Free Surface Shape

As mentioned earlier, matching of free surface shape between one-dimensional and two-dimensional region is made by imposing continuity in the film thickness, slope, and curvature. The matching of thickness is applied by replacing residuals (3.7), or (3.15) or (3.14) at the matching plane with

$$R^h_{\text{match}} = h_{1-D} - h_{2-D} \tag{3.28}$$

where h_{1-D} is either the film thickness of slide flow h_s or that of web flow h_w evaluated at the matching plane. h_{2-D} is the location of the free surface at the corners of the bead region and can be calculated based on the matching location by:

$$h_{2-D} = \sqrt{(x_f - x_{\text{match}})^2 + (y_f - y_{\text{match}})^2} \tag{3.29}$$

where x_f and y_f are the position of the free surface corner points of the bead region and x_{match} and y_{match} are the position of the matching location points at the slide or

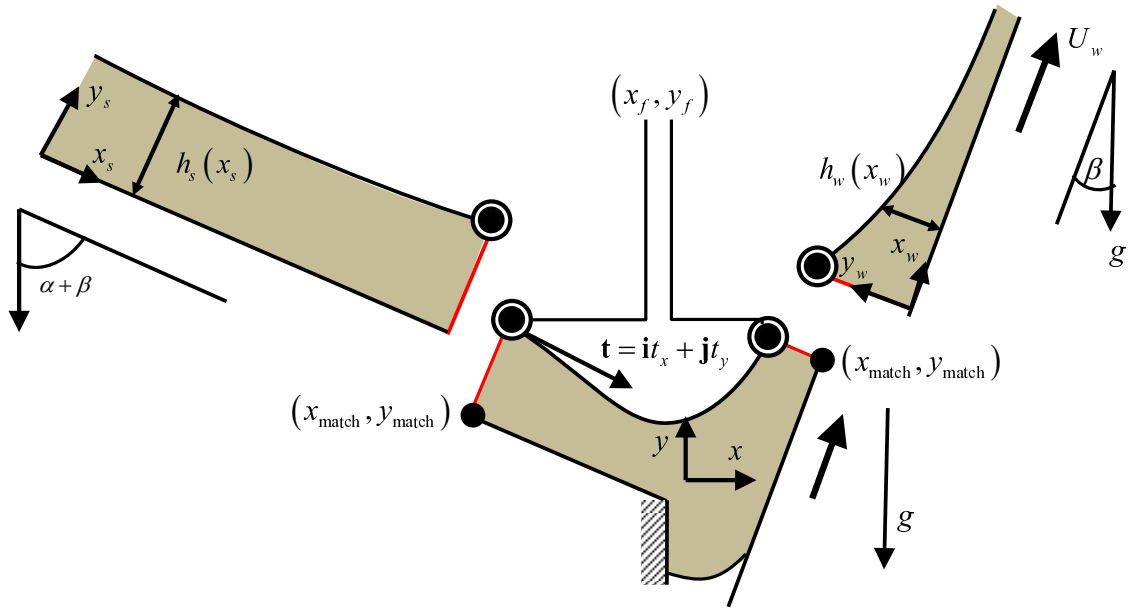

Figure 3.3: Matching free surface illustration

web surface. Similarly, inclination matching is applied by replacing residuals (3.8), or (3.16), or (3.14) with

$$R^{\phi}_{\text{match}} = \phi_{1-D} - \phi_{2-D} \tag{3.30}$$

where ϕ_{1-D} is either the film inclination of slide flow ϕ_s or that of web flow ϕ_w evaluated at the matching plane. ϕ_{2-D} is the inclination of the free surface at each corner of the bead region and can be calculated from the tangent vectors at the corner points by

$$\phi_{2-D} = \arctan\left(\frac{t_y}{t_x}\right) - \phi_{\text{shift}} \tag{3.31}$$

where ϕ_{shift} is the angle between the coordinate system employed in the slide or web and bead regions. ϕ_{shift} between the slide and bead coordinate system is $\alpha + \beta - \frac{\pi}{2}$ and that of bead - web region is $\beta + \frac{\pi}{2}$. t_x and t_y are the x and y components of the tangent vector of the free surface at those corner points. They are evaluated at the

reference domain to be:

$$t_x = \frac{\frac{\partial x}{\partial \xi}}{\sqrt{\left(\frac{\partial x}{\partial \xi}\right)^2 + \left(\frac{\partial y}{\partial \eta}\right)^2}} \quad \text{and} \quad t_y = \frac{\frac{\partial y}{\partial \eta}}{\sqrt{\left(\frac{\partial x}{\partial \xi}\right)^2 + \left(\frac{\partial y}{\partial \eta}\right)^2}} \tag{3.32}$$

where ξ and η are the coordinates at the reference domain. The mapping between the physical coordinates and the reference coordinates is governed by elliptic mesh generation equations 3.6 discussed earlier. Curvature matching is applied in similar manner, by replacing residuals (3.9), or (3.17), or (3.14) with

$$R^{\kappa}_{\text{match}} = \kappa_{1-D} - \kappa_{2-D} \tag{3.33}$$

where κ_{1-D} is either the film curvature of slide flow κ_s or that of web flow κ_w evaluated at the matching plane. κ_{2-D} is the curvature of the free surface at each corner of the bead region and is evaluated in the reference domain as follows

$$\begin{aligned} \kappa_{2-D} &= \mathbf{n} \cdot \frac{\mathrm{d}\mathbf{t}}{\mathrm{d}s} \\ &= \frac{-\left(\frac{\partial y}{\partial \xi}\right)^2 \left(\frac{\partial^2 x}{\partial \xi^2}\frac{\partial y}{\partial \xi} - \frac{\partial x}{\partial \xi}\frac{\partial^2 y}{\partial \xi^2}\right) + \left(\frac{\partial x}{\partial \xi}\right)^2 \left(\frac{\partial x}{\partial \xi}\frac{\partial^2 y}{\partial \xi^2} - \frac{\partial^2 x}{\partial \xi^2}\frac{\partial y}{\partial \xi}\right)}{\left[\left(\frac{\partial x}{\partial \xi}\right)^2 + \left(\frac{\partial y}{\partial \eta}\right)^2\right]^{\frac{5}{2}}} \end{aligned} \tag{3.34}$$

Both slide and web flow equations are systems of 3 first-order ODE and each of them requires three boundary and matching conditions. In principle, each film profile equation has 4 possibilities of applying these conditions: All three at inflow, one at inflow and two at outflow, two at inflow and one at outflow, and all three at outflow. In the bead region, two matching conditions are available to set the position of the free surface corner points at both matching planes. Choosing the right combinations of boundary and matching conditions is critical in order to maintain continuity of the film thickness, inclination, and curvature throughout the whole domain.

In the slide region, applying all 3 conditions in the inflow boundary will leave no condition to be applied at the matching plane and the only coupling between the slide and the bead region is from one matching condition at the corner point provided by the bead region. This scheme will lead to continuity of only one degree of freedom, e.g. film thickness, across the slide-bead matching plane, leaving the other two, e.q. film inclination and curvature, to be discontinuous. On the other hand, applying all 3 conditions at the matching planes will lead to overspecified system, since with the addition of one matching condition contributed from the bead region, brings up the total to 4 matching conditions for specifying 3 degree of freedoms at the matching plane. The same guideline also applies in determining the numbers of boundary and matching conditions to be applied at the web region. Therefore, the ideal combination of boundary and matching conditions assignments for governing film shape are:

1. At slide region, apply one boundary condition at the inflow and two matching conditions at the matching plane.
2. At the bead region, apply one matching condition each to its matching planes.
3. At web region, apply two matching conditions at the matching plane and one boundary conditions at the outflow.

With this arrangement, a total of three matching conditions is applied at each matching plane to ensure continuity of film thickness, inclination, and curvature across all these regions. The assignment of the *type* of matching and boundary conditions to be applied was not found to be as critical as in the counting of the *number* of boundary and matching conditions. As long as there is no redundancy in applying matching conditions between two regions, i.e. the same matching condition is applied twice by replacing both residuals at both regions with the same condition, that leads to singular system.

In this study, the film profile equation of the slide region have one boundary condition imposed at the inflow and have two matching conditions applied at the matching

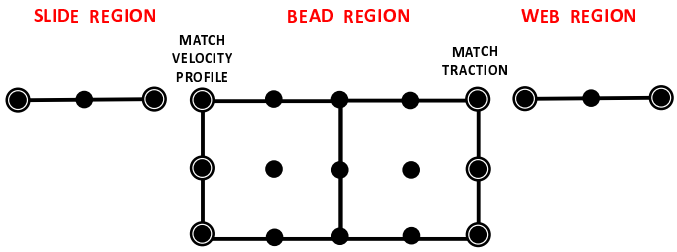

(a) Mass and Momentum Boundary and Matching Conditions

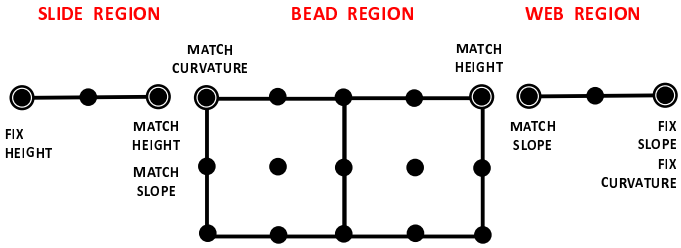

(b) Mesh Boundary and Matching Conditions

Figure 3.4: Boundary and Matching Conditions Assignment

plane. At the other side, the bead region contributes one matching condition to the matching plane. This gives a total of three matching conditions that can be specified between the slide and bead regions: Matching of thickness and inclination at the slide region side and matching of curvature at the bead region side.

Ideally, web flow should have two matching condition at the matching plane and one outflow boundary condition. However, as shown later in the next section, that assignment does not lead to physical solution. Instead, the opposite assignment needs be applied: One matching condition and two outflow boundary conditions. Web flow equation have two boundary conditions specified at the outflow and can only accept one matching condition at the matching plane. With the addition of one matching condition that the bead region can contribute, only two matching conditions are imposed at the matching plane between the bead and web flow regions. Continuity of film thickness and slope are imposed here.

3.3 Effect of Matching Conditions

3.3.1 Reversing Number of Matching and Boundary Conditions

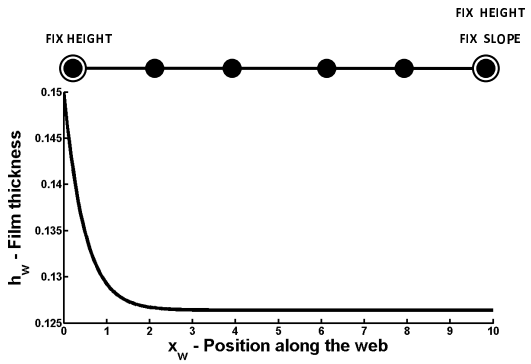

(a) One inflow condition and two outflow conditions

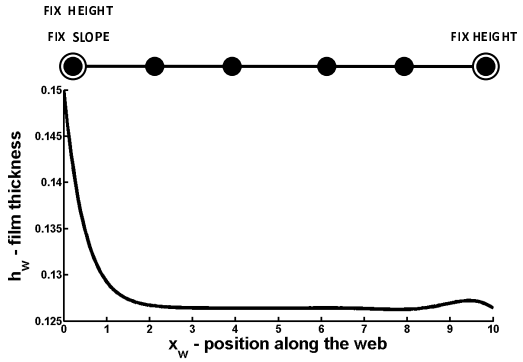

(b) Two inflow conditions and one outflow condition

Figure 3.5: Effect of reversing numbers of matching and boundary conditions at the web flow region

As mentioned earlier, solution of the film profile equation of web is not physical when two matching conditions are applied in the matching plane or the inflow and one boundary condition is applied in the outflow. This is evident from the results of numerical experiments performed by solving the film profile equation of the web alone. As shown in Fig. 3.5, reversing the number of matching or boundary conditions at

the inflow and outflow leads to the film profile to form standing wave at the outflow and this result is not physical. On the other hand, with one condition applied at the inflow and two boundary conditions applied at the outflow, the film profile reaches its fully developed thickness at the outflow, as expected. The film profile equation of slide region does not have the same problem. The number of matching and boundary conditions can be reversed without yielding to non-physical solution as in the case of web film profile equation.

Therefore, the film profile of web flow can only have one matching condition imposed on it and with the addition from one matching condition that can be applied at the bead region, bring up the total number of matching conditions that can be imposed between the bead and web regions to be only two. In this study, we chose to sacrifice the matching of curvature. However, the discontinuity of curvature is not expected to be large enough due to the matching traction condition (3.24) imposed from the mass and momentum matching condition. When the flow is rectilinear at the matching plane, the pressure field is governed solely by the curvature of the film. Since the pressure field is weakly matched, we expect the curvature difference in the plane to be small and it was found to be in the order of 10^{-6}. In contrast, because the film profile equations of the slide region permits for two matching conditions, and the mesh generation equation of the bead region requires one matching condition, a total of three matching conditions can be imposed there: matching of film thickness, inclination, and curvature.

3.3.2 Effect of Momentum and Mass Matching Conditions Assignments

Figure 3.6 displays the prediction of pressure field and streamlines from four matching condition assignments and how they are compared with the prediction from full 2-D model. Relaxing the matching traction condition into only matching pressure and letting the viscous component to be free did not appear to affect the model accuracy

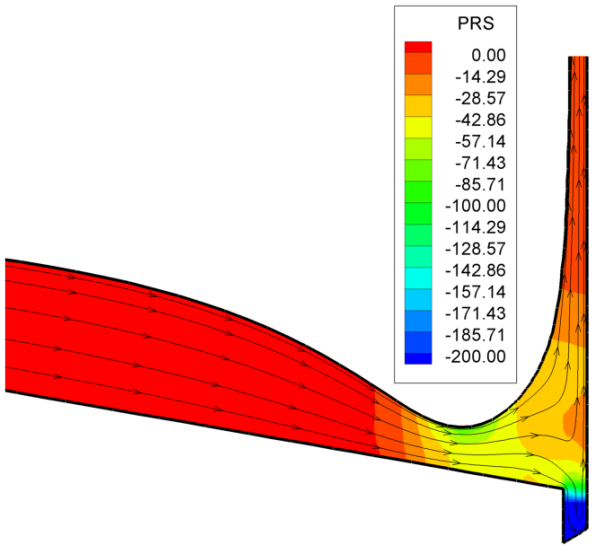

(a) Full 2-D

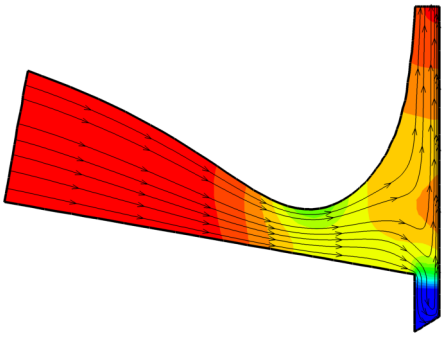

(b) Match velocity at slide-bead and match traction at bead-web

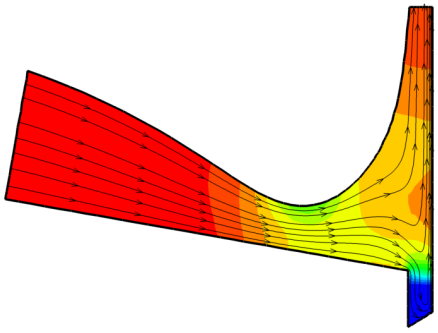

(c) Match velocity at slide-bead and match pressure at bead-web

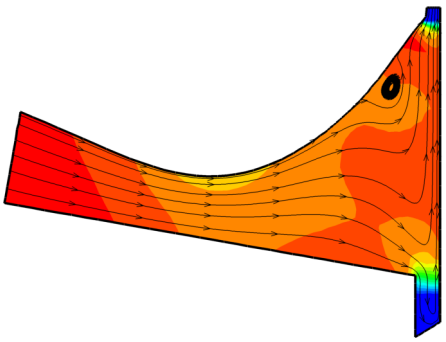

(d) Match traction at slide-bead and match velocity at bead-web

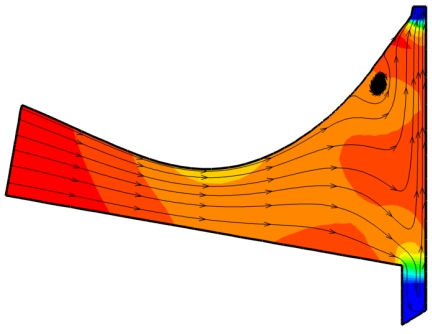

(e) Match pressure at slide-bead and match velocity at bead-web

Figure 3.6: Comparison of streamline and pressure field predictions at different mass and momentum matching conditions with full 2-D model - $\alpha = 80^{o}$, $\beta = 0^{o}$, Re = 16, Ca = 0.009, $h_{\infty}/h_0 = 0.16$

significantly, as shown in Fig. 3.6(c). However, reversing the matching conditions assignment by imposing matching of traction with the slide flow and matching of velocity profile with the web flow causes the prediction to be non physical in both velocity profile and pressure fields, as shown in Fig. 3.6(d). This can be attributed to the lack of curvature matching between the bead and web regions, that ultimately dictate the pressure field at the matching zone. Therefore, maintaining the pressure matching with the web region is necessary. Imposing matching of velocity profile with both slide and web flows is too restrictive and the trial did not yield converged solution. Imposing matching traction on both slide and web flow is too relaxed and no solution was found, even with the correct solution as the initial guess.

3.3.3 Effect of Matching Locations

The effect of moving the matching locations on the hybrid model accuracy is shown in Figs. 3.7 and 3.8. As the bead region is shrunk by shifting the slide - bead matching location further downstream or bead-web matching further upstream, the prediction of the free surface shape and pressure field is worsen. , the predictions of pressure field is worsen. Figs. 3.7(c) and 3.7(d) demonstrates that predictions of pressure fields at near the matching plane lose accuracy when the matching location of the bead-web and the slide-bead is shifted toward the bead region respectively. Fig. 3.8(c) further demonstrates that in addition to the loss of accuracy in the pressure fields, shifting the slide-bead matching plane downstream leads to inaccurate free surface shape at the slide region. The accuracy of the model can be improved by expanding the bead region, therefore expanding the region where the full 2-D Navier-Stokes calculation is performed, as demonstrated in Figs. 3.7(e) and 3.8(d). The lesson that can be learned from this study is that as in any synthetic inflow or outflow plane, the locations of the matching planes need to be such that the solution is not affected by shifting the inflow matching plane upstream and the outflow matching plane downstream.

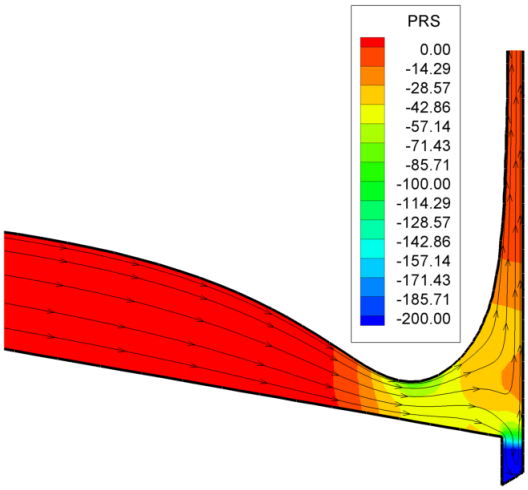

(a) Full 2-D

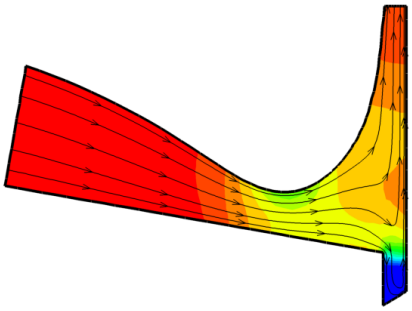

(b) Default matching location

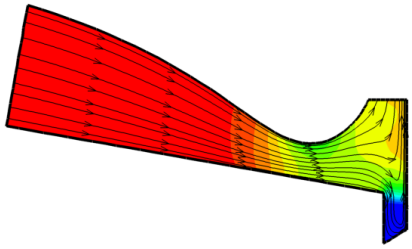

(c) Bead-web matching location shifted upstream

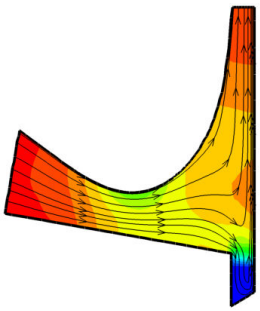

(d) Slide-bead matching location shifted downstream

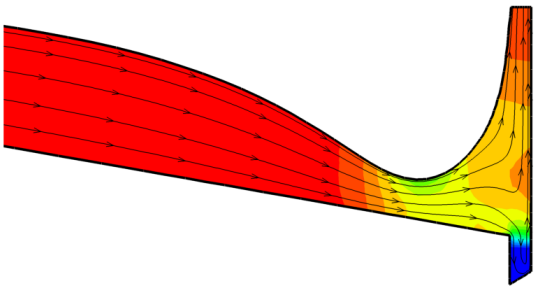

(e) Slide-bead matching location shifted upstream

Figure 3.7: Comparison of streamline and pressure field predictions at different matching point locations with full 2-D model - $\alpha = 80^o$, $\beta = 0^o$, Re = 16, Ca = 0.009, $h_\infty/h_0 = 0.16$

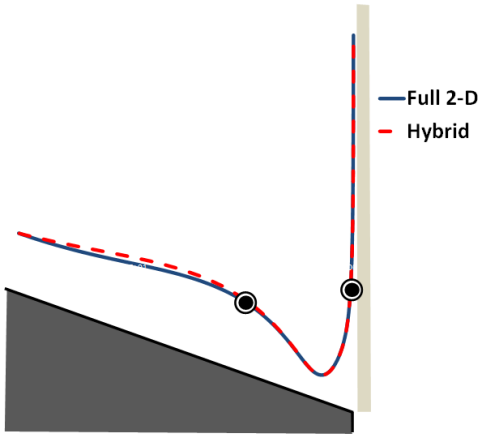

(a) Base Case

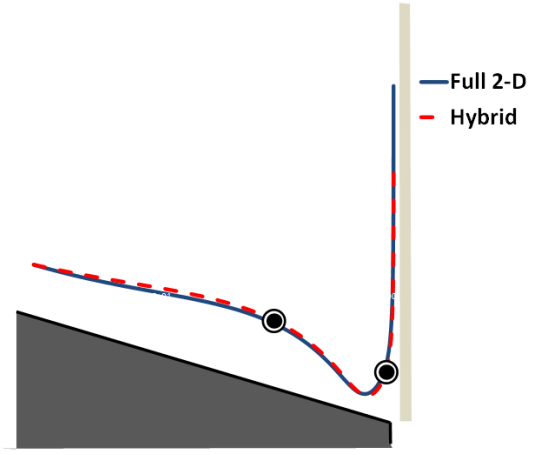

(b) Web Flow Matching Point Shifted Upstream

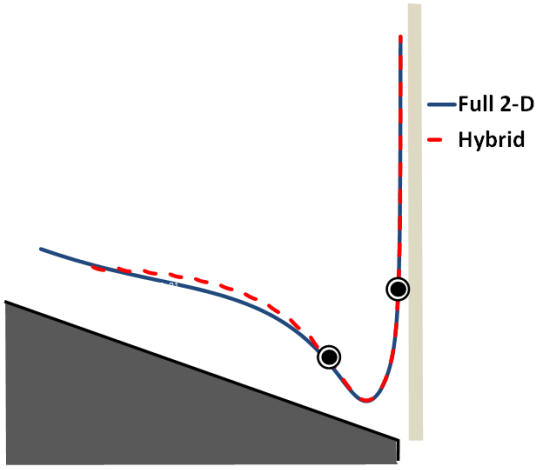

(c) Slide Flow Matching Point Shifted Downstream

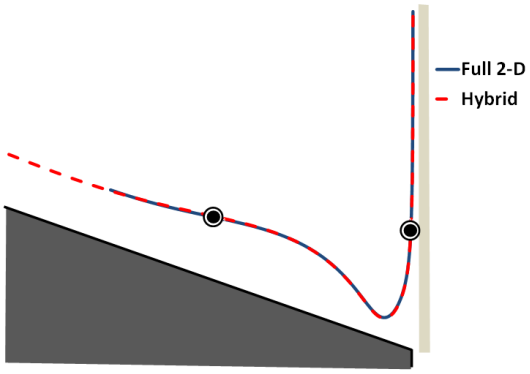

(d) Slide Flow Matching Point Shifted Upstream

Figure 3.8: Comparison of free surface predictions with full 2-D model at different matching point locations - $\alpha = 80^o$, $\beta = 0^o$, Re $= 16$, Ca $= 0.009$, $\frac{h_\infty}{h_0} = 0.16$

	Full 2-D	Hybrid Model
	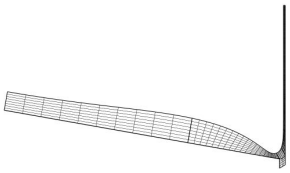	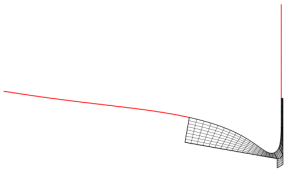
Number of elements	512	302
Number of nodes	2197	1239
Number of degree of freedoms	10324	5772
Average time per Newton iteration (ms)	10.2	5.86

Table 3.1: Comparison of computation cost between hybrid and full 2-D models

3.4 Comparison of Computation Cost

The computation cost of the hybrid and full 2-D models was compared and the result is summarized in Table 3.1. Both models have the same refinement at the free surface and therefore the comparison of free surface shape prediction is mesh independent. Similarly, the bead region at both models have the same refinement that makes the prediction of pressure field and streamline to be mesh independent as well. As shown in Table 3.1, the hybrid model has about 40 % less number of degree of freedoms than the full 2-D model that leads to reduction of computational time by a factor of approximately 2. This advantage will become more significant when the computation have to be performed so many times as in parametric study for constructing theoretical coating window.

3.5 Model Validation: Comparison with Predictions from Full 2-D Model

Predictions of the free surface shape, streamlines, and pressure fields from the hybrid model was compared with prediction from the full 2-D model in order to determine the range of parameter space where the hybrid model is valid. Each figure that shows comparison of pressure field and streamlines between the hybrid and full 2-D

models only displays pressure field and streamlines at the bead region of the hybrid model. The parameters explored were Reynolds number $\mathrm{Re} = \frac{\rho q}{\mu}$ and capillary number $\mathrm{Ca} = \frac{\mu U_w}{\sigma}$.

Comparison of the hybrid model predictions to those of full 2-D model at different Reynolds and capillary numbers are shown in Figs. 3.9, 3.10, and 3.11. The hybrid model is accurate at low Reynolds and capillary number and remain so at moderate capillary number and low Reynolds number. As Reynolds number rises, the free surface prediction at the slide region is worsen and it is consistent with what was found by Tjiptowidjojo and Carvalho (2009) at the viscocapillary model of slide coating. However when the Reynolds number rises, as shown in Figs. 3.12 and 3.13, the model overpredicts the standing wave size due to inaccuracy of the film profile equation at the slide region, as demonstrated by Tjiptowidjojo and Carvalho (2009). The accuracy can be recovered by shifting the matching location between slide and bead regions further upstream where the approximation used to derive film profile equation at the slide region is still valid.

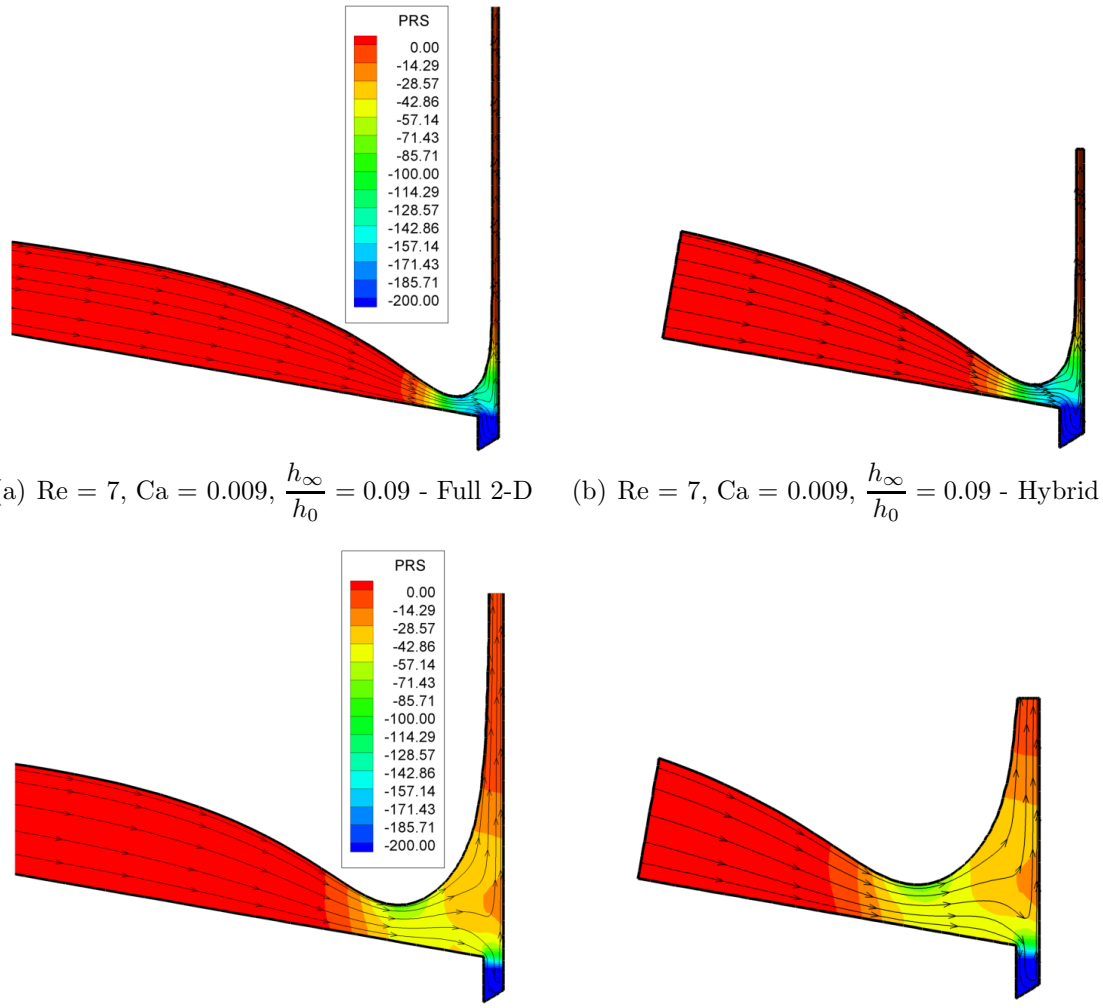

(a) Re = 7, Ca = 0.009, $\frac{h_\infty}{h_0} = 0.09$ - Full 2-D (b) Re = 7, Ca = 0.009, $\frac{h_\infty}{h_0} = 0.09$ - Hybrid

(c) Re = 16, Ca = 0.009, $\frac{h_\infty}{h_0} = 0.16$ - Full 2-D (d) Re = 16, Ca = 0.009, $\frac{h_\infty}{h_0} = 0.16$ - Hybrid

Figure 3.9: Comparison of streamline and pressure field predictions with full 2-D model at different Reynolds and capillary numbers - Part I - $\alpha = 80^o$, $\beta = 0^o$

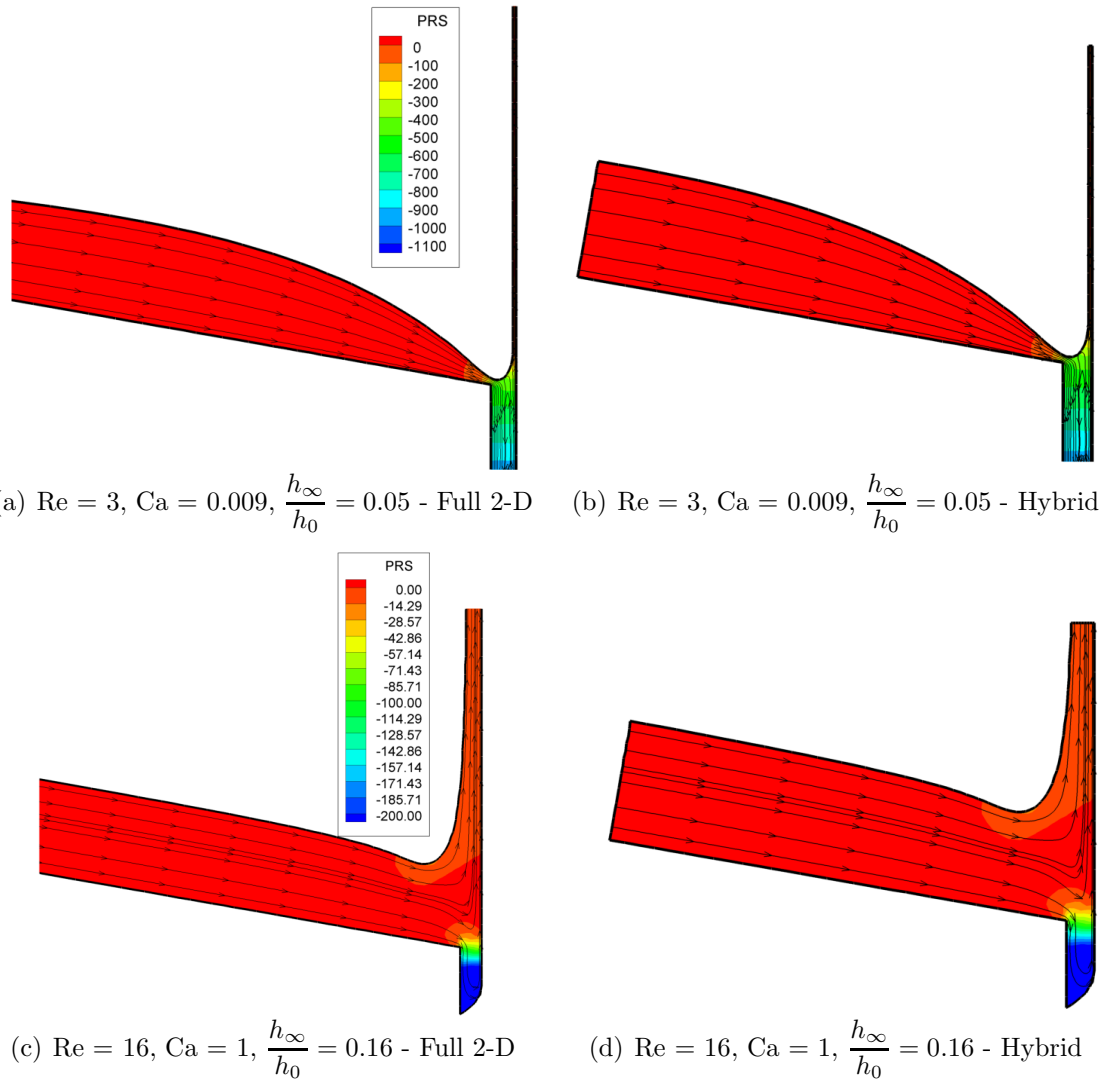

(a) Re = 3, Ca = 0.009, $\frac{h_\infty}{h_0} = 0.05$ - Full 2-D

(b) Re = 3, Ca = 0.009, $\frac{h_\infty}{h_0} = 0.05$ - Hybrid

(c) Re = 16, Ca = 1, $\frac{h_\infty}{h_0} = 0.16$ - Full 2-D

(d) Re = 16, Ca = 1, $\frac{h_\infty}{h_0} = 0.16$ - Hybrid

Figure 3.10: Comparison of streamline and pressure field predictions with full 2-D model at different Reynolds and capillary numbers - Part II - $\alpha = 80^o$, $\beta = 0^o$

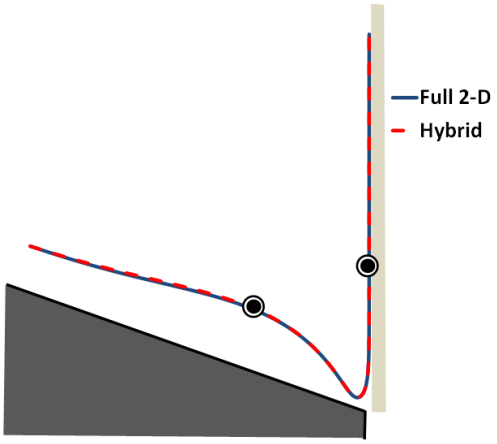

(a) Re = 7, Ca = 0.009, $\frac{h_\infty}{h_0} = 0.09$

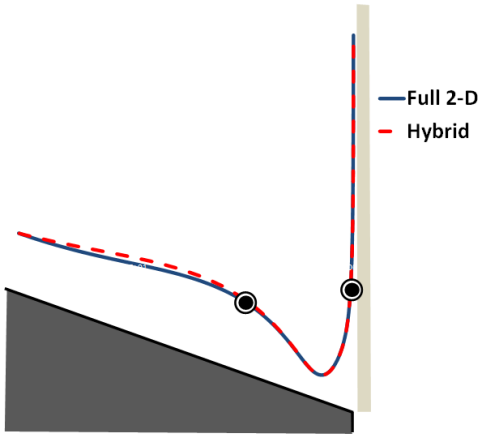

(b) Re = 16, Ca = 0.009, $\frac{h_\infty}{h_0} = 0.16$

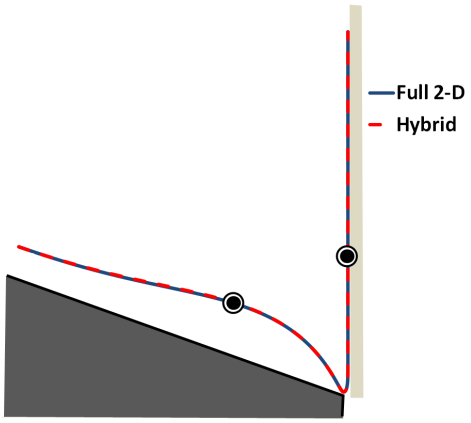

(c) Re = 3, Ca = 0.009, $\frac{h_\infty}{h_0} = 0.05$

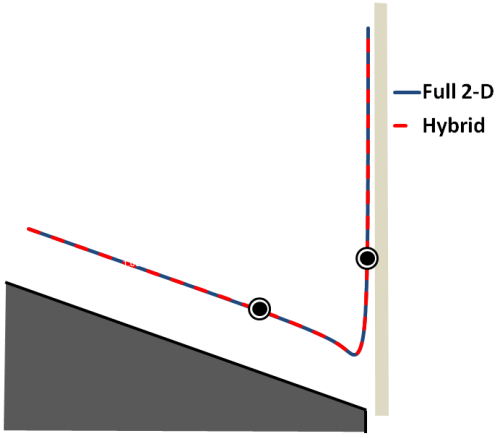

(d) Re = 16, Ca = 1, $\frac{h_\infty}{h_0} = 0.16$

Figure 3.11: Comparison of free surface predictions with full 2-D model at different capillary and Reynolds numbers - $\alpha = 80^o$, $\beta = 0^o$

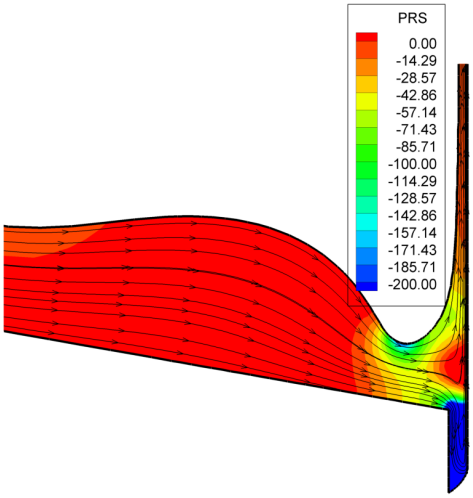

(a) Full 2-D

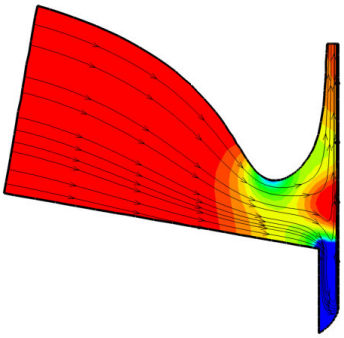

(b) Default matching locations

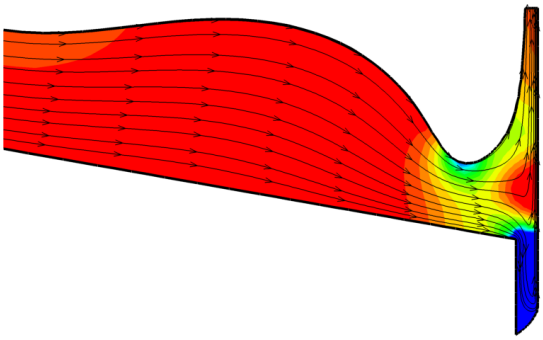

(c) Slide-bead matching location shifted upstream

Figure 3.12: Comparison of streamline and pressure field predictions with full 2-D model at high Reynolds and capillary numbers - $\alpha = 80^o$, $\beta = 0^o$, Re = 39, Ca = 0.4, $\frac{h_\infty}{h_0} = 0.07$

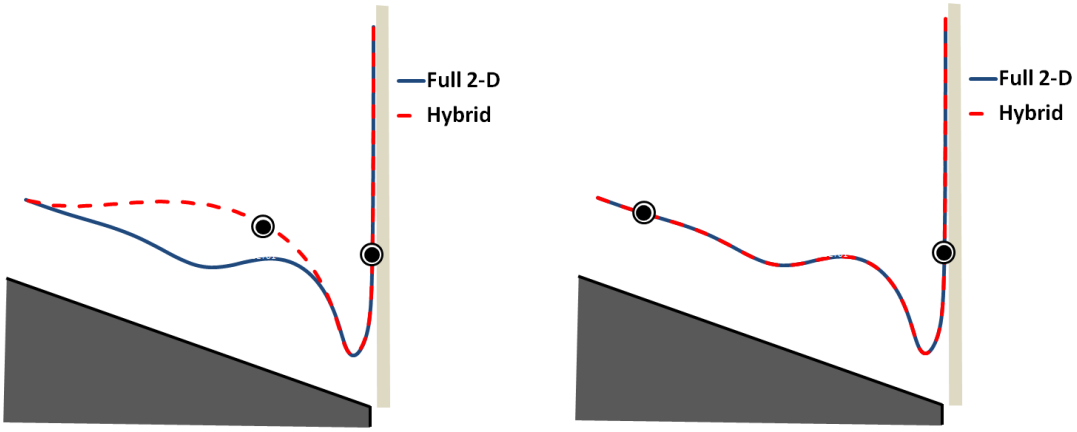

(a) Default matching locations

(b) Slide-bead matching location shifted upstream

Figure 3.13: Comparison of free surface predictions with full 2-D model at high Reynolds and capillary numbers - $\alpha = 80^{o}$, $\beta = 0^{o}$, Re $= 39$, Ca $= 0.4$, $\frac{h_{\infty}}{h_0} = 0.07$

3.6 Concluding Remarks

A hybrid model of slide coating was constructed where a full 2-D Navier-Stokes calculation is performed at the coating bead region only, and film profile equation at the rest of the region. These regions need to be connected with matching conditions and in principle, there are multiple possible combinations of matching conditions that can be employed. However, we demonstrated that only one combination works well. The model requires about 60 % less memory and is twice faster to compute than solutions of the full 2-D model. The hybrid model is as accurate as the full 2-D model, providing that the matching conditions are assigned properly and their locations are far enough such that the approximations employed in deriving the viscocapillary model remains valid there.

Chapter 4

Operability Windows of Slide Coating

4.1 Introduction

Operability window of a coating process is a region of the operating conditions space in which a coating operation is feasible. Feasibility of continuous coating process relies heavily on how to maintain a stable and continuous coating bead. Understanding how coating bead responds to a set of operating condition and liquid properties is essential in producing defect-free coating.

Most of the slide coating windows reported in the literatures came from experiments. Tallmadge et al. (1979) reported experimental values of lower and upper coating speed limits under different flow rates, gap widths, and viscosities. They did not apply vacuum underneath the coating bead. Gutoff and Kendrick (1987) improved Tallmadge et al. (1979)'s experimental methods by incorporating vacuum in their studies of slide coating's low flow limit at different viscosities and gap widths. Low flow limit is defined to be the minimum thickness that can be achieved at a given coating speed or the maximum coating speed that can be achieved at a given coating

thickness. They demonstrated that thinner coating can be achieved when vacuum is applied underneath the bead. Chen (1992) reported experimental values of vacuum limits at different coating thickness, but he did not investigate low flow limit. Hens and van Abbenyen (1997) determined experimentally values of ribbing and rivulets formation. Schweizer (1988) improved flow visualization technique of coating flows with the use of dye and hydrogen bubbles and he was able to capture streamlines and vortices in the slide coating flow. With those tools, he was able to report critical flow rates corresponding to the onset of vortex birth at the downstream meniscus at a given coating speed. However none of these studies explored coating bead breakup mechanisms. Theoretical modeling allows for fundamental understanding in how the coating bead breakup occurs.

Advances in the theoretical modeling of coating flow, especially in slide coating, has been made by Christodoulou and Scriven (1989) where they solved the full 2-D steady Navier-Stokes with Galerkin finite element method. However due to high computation cost in that time, they only made few excursions in the parameter space and therefore, did not perform systematic exploration to find operability limits. The goals of this study are to find mechanisms of coating failures and defects formation and to predict critical operating conditions corresponding to the onset of those failures. Effects of gap width, slide inclination, and die-lip geometry are investigated as well.

4.2 Mathematical Model

Successful coating operation requires the flow to be steady, two-dimensional except at the edges, and stable to small disturbances. The appropriate mathematical model used to describe the flow in the coating bead shown in Fig. 4.1 is steady state full two-dimensional Navier-Stokes equations. The appropriate boundary conditions and solution method are discussed in this section.

4.2.1 Governing Equations and Boundary Conditions

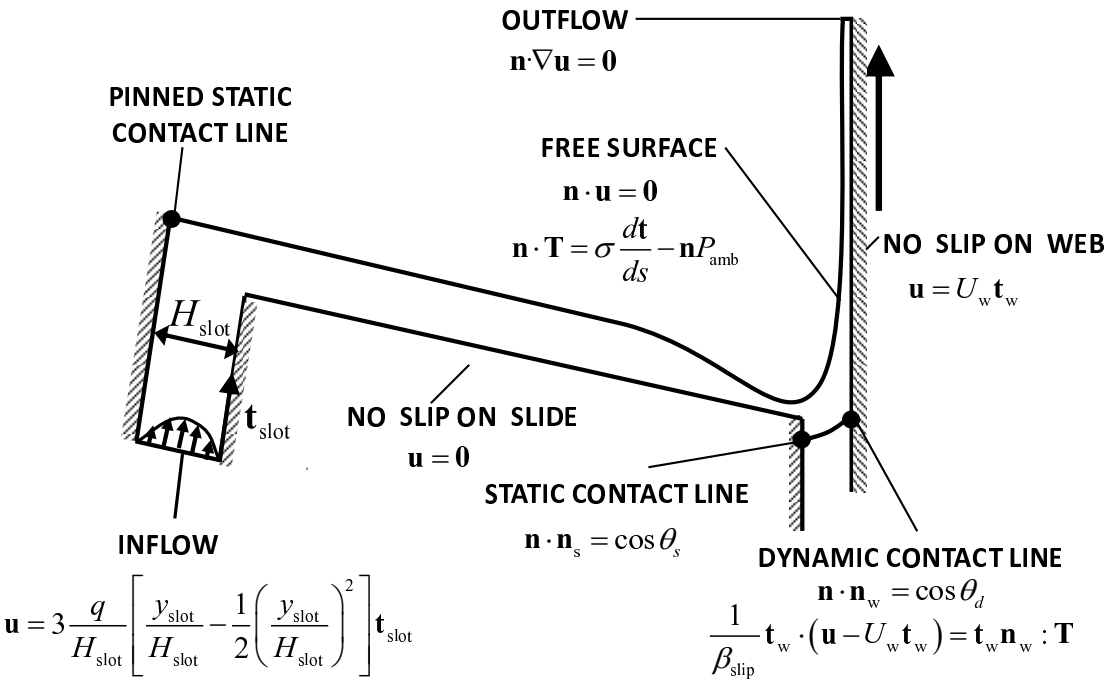

Figure 4.1: Two-dimensional model of slide coating

The steady state full two-dimensional Navier-Stokes equation system that governs liquid flow in slide coating is

$$\rho\mathbf{u}\cdot\nabla\mathbf{u}=\rho\mathbf{g}+\nabla\cdot\mathbf{T}\quad\text{and}\quad\nabla\cdot\mathbf{u}=0 \tag{4.1}$$

where ρ is the liquid density, $\mathbf{g}$ is the gravitational acceleration, $\mathbf{T}=-p\mathbf{I}+\mu\left[\nabla\mathbf{u}+(\nabla\mathbf{u})^{\mathrm{T}}\right]$ is the total stress tensor, p is pressure, and μ is the liquid viscosity.
The conditions at each flow boundary sketched in Fig. 4.1 are:

1. *Inflow: Fully developed velocity profile.* At inflow boundary with width of H_{slot},

a parabolic velocity profile is imposed:

$$\mathbf{u} = 3\frac{q}{H_{\text{slot}}}\left[\frac{y_{\text{slot}}}{H_{\text{slot}}} - \frac{1}{2}\left(\frac{y_{\text{slot}}}{H_{\text{slot}}}\right)^2\right]\mathbf{t_{slot}} \tag{4.2}$$

with specified volumetric flow rate per unit width q.

2. *Slide and web surfaces: No slip, no penetration.* $\mathbf{u} = \mathbf{0}$ at slide surface and $\mathbf{u} = U_{\text{w}}\mathbf{t}_{\text{w}}$ at the web surface, where U_{w} is the web speed.

3. *Free surface: Force balance and kinematic condition.*

$$\mathbf{n}\cdot\mathbf{T} = \sigma\frac{d\mathbf{t}}{ds} - \mathbf{n}P_{\text{amb}} \quad \text{and} \quad \mathbf{n}\cdot\mathbf{u} = 0 \tag{4.3}$$

σ is the liquid surface tension, s is arc length coordinate along the free surface, and P_{amb} is the ambient pressure and set to zero at the top free surface and to a sub-ambient pressure (vacuum pressure) at the bottom free surface.

4. *Static and dynamic contact lines.* The static contact line at the feed slot exit is pinned at the corner of the elevated block adjacent to the slot exit and the static contact line at the coating bead is allowed to move along the die face with prescribed contact angle θ_s. The dynamic contact line in the coating bead is allowed to move along the web with a prescribed contact angle θ_d and the Navier slip condition is imposed to alleviate the singularity there (Huh and Scriven 1971)

$$\frac{1}{\beta_{\text{slip}}}\mathbf{t}_{\text{w}}\cdot(\mathbf{u} - U_{\text{w}}\mathbf{t}_{\text{w}}) = \mathbf{t}_{\text{w}}\mathbf{n}_{\text{w}} : \mathbf{T} \tag{4.4}$$

5. *Outflow: Fully developed flow..* At the web outflow, fully developed flow condition is imposed in the weaker sense such that the velocity profile does not change in the downstream direction. $\mathbf{n}\cdot\nabla\mathbf{u} = \mathbf{0}$

The appropriate dimensionless parameters involved in the analysis are the capillary number $Ca = \dfrac{\mu U_{\text{w}}}{\sigma}$ which represents the ratio of viscous force to capillary pressure and Reynolds number $\dfrac{\rho q}{\mu}$ which represents the ratio of inertia to viscous force.

4.2.2 Solution Method

Due to the free surface, the flow domain is unknown apriori. This free boundary problem was then solved by transforming the equations to an equivalent set defined in a known reference domain. The transformation was performed by a mapping $\mathbf{x} = \mathbf{x}(\boldsymbol{\xi})$ to connect these two domains. This work used the mapping scheme presented by de Santos (1991) and Benjamin (1994). They proposed a pair of elliptic differential equations identical to the ones encountered in diffusional transport process with variable diffusion constant to govern the inverse of mapping, i.e. $\boldsymbol{\xi} = \boldsymbol{\xi}(\mathbf{x})$:

$$\nabla \cdot (\mathrm{D}_\xi \nabla \xi) = 0 \quad \text{and} \quad \nabla \cdot (\mathrm{D}_\eta \nabla \eta) = 0 \tag{4.5}$$

where D_ξ and D_η are diffusion-like coefficients used to control element spacing. The appropriate boundary conditions for these inverse mapping equations are specifications of solid surface geometry as well as in the synthetic inflow and outflow planes. Node distributions along the boundaries were governed by stretching functions listed by Vinokur (1983) and de Santos (1991).

The Navier-Stokes system together with the mapping equation were solved altogether with Galerkin/ finite element method. Velocity and the mapping from reference to physical domain were represented with biquadratic basis function, and pressure was represented with piecewise linear discontinuous basis function. The details of the formulation on this class of problem can be found elsewhere (Kistler and Scriven 1983).

After all of the variables are represented in terms of basis functions, the system of partial differential equations was transformed into a system of algebraic equations that is nonlinear in coefficients of the basis functions. The equation system was then solved with Newton's method and the linear equation system in each Newton iteration was solved with a frontal solver. In the parametric study, initial guess at each new operating conditions was obtained with a pseudo-arc-length continuation method described by Bolstad and Keller (1986).

4.3 Results

First, we describe the different mechanisms associated with the different coating failures. After this general description, predictions of the critical operating parameters that marks the boundaries of the coating window are presented.

4.3.1 Coating Bead Breakdown Mechanisms

Vacuum Limits

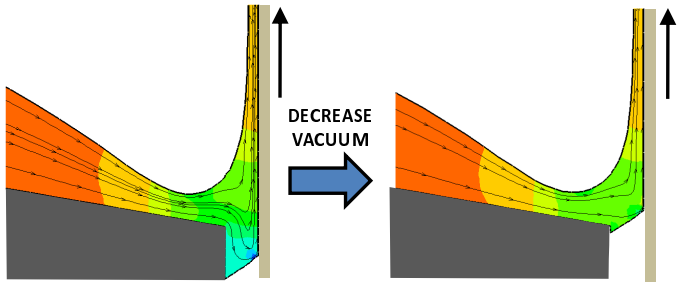

Figure 4.2: Bead breakup mechanism at low vacuum limit

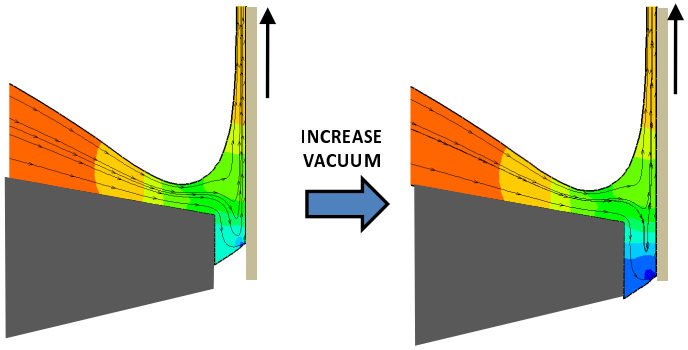

Figure 4.3: Bead breakup mechanism at high vacuum limit

As the applied vacuum underneath the upstream meniscus is reduced, the meniscus position moves downstream and approaches the downstream die lip corner, as shown

in Fig. 4.2. If the applied vacuum is lowered even more, the meniscus will eventually poke through the coating bead and create alternating dry and coated lanes known as *rivulets*. On the other hand, as the applied vacuum underneath is raised, the upstream meniscus position moves upstream toward the vacuum box, as shown at Fig. 4.3. The upper limit of the applied vacuum is reached when the static contact line is located on the upstream corner of die lip. An applied higher vacuum will result in the leakage of the coating liquid toward the vacuum box and the premetered action will be lost. In the conditions studied, the downstream meniscus is not affected by the applied vacuum and plays no role in the bead breakup at low and high vacuum limits. In both low and high vacuum limits, the bead breakdown is originated from the upstream meniscus.

Flow Limits

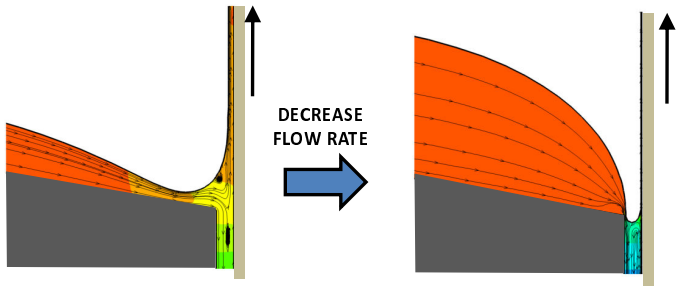

Figure 4.4: Bead breakup mechanism at low flow limit - low Ca

Low-flow or minimum-thickness limit sets the thinnest coating that can be obtained at a given coating speed, or the fastest coating speed that can be achieved at a given coating thickness. It is the most important process limit in terms of the economics that warrants several studies on it (Gutoff and Kendrick (1987); Hens and Boiy (1986); Lee et al. (1992)). As flow rate falls, the downstream meniscus becomes highly curved in order to create the necessary adverse pressure gradient for metering out the coated liquid on the web, as shown in Figs. 4.4 and 4.5. Two different bead breakup mechanisms of low flow limits are observed as the flow rate is lowered to

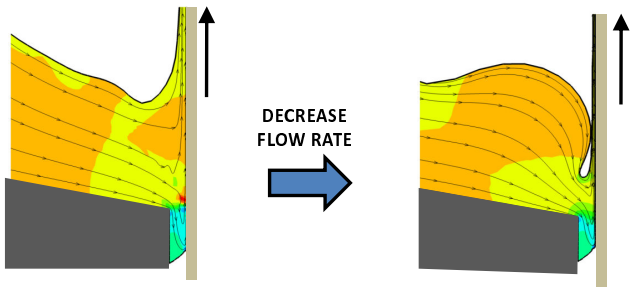

Figure 4.5: Bead breakup mechanism at low flow limit - high Ca

a critical flow rate. At low capillary number, the curved downstream meniscus will invade the gap and poke through the coating bead that will lead to formation of rivulets, just like in the low-vacuum limit case. However, the rivulet formation is now triggered from the downstream meniscus poking through the coating bead, instead of upstream meniscus. At high capillary number, the meniscus is allowed to curve even more without invading the gap due to relatively thick film on the slide. However, the meniscus cannot physically curve more than what is shown in Fig. 4.5, thus it sets the low flow limit at high capillary number. Both limiting flow states at low and high capillary numbers are unlikely observed in practice. The flow probably becomes unstable with respect to 2-D disturbances because of the highly curved meniscus, leading to ribbing formation that might occur before the meniscus breaks

High flow limit is set by the competition between viscous drag supplied by the web and the gravity force. In principle, the thickest film that can be carried away by a moving web is the one corresponding to the onset of turnaround flow at the free surface of the web outflow region. The onset of turnaround flow occurs *when the velocity at the film surface is equal to zero.* Therefore the maximum film thickness is estimated as

$$h_{\infty,\max} = \sqrt{\frac{2\mu U_w}{\rho g \cos\beta}} \tag{4.6}$$

4.3.2 Theoretical Prediction of Coating Window

Theoretical predictions of the coating bead breakup mechanisms reveal that the onset of the bead breakup can be estimated based on the location and the shape of the menisci. Low vacuum limit was set to be the value of the applied vacuum at which the contact line along the web surface, i.e. dynamic contact line position, is located right across from the die-lip corner. This criterion is used to predict the onset of upstream meniscus invasion of the coating bead. Similarly, high vacuum limit corresponds to the value of applied vacuum at which the static contact line is located at the upstream edge of the die face. The predictions of high and low vacuum limits as a function of coating thickness are plotted in Fig. 4.6. The values of high and low vacuum limits rise as the coating thickness fall, indicating the need to apply more vacuum in order to maintain the bead at thinner coating.

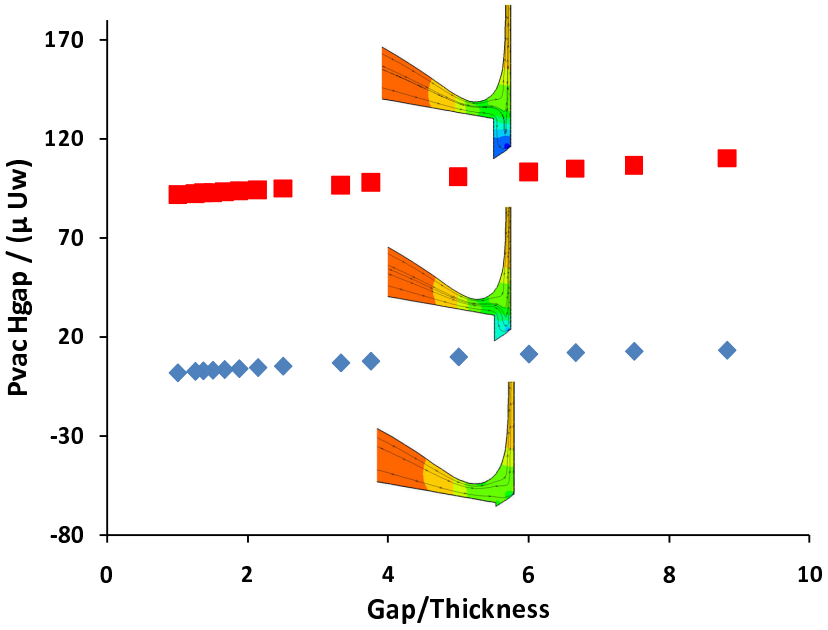

Figure 4.6: Vacuum limits of slide coating

Low flow limit or minimum film thickness can also estimated in the similar manner as the vacuum limits. However, instead of tracking the locations of upstream meniscus, low flow limit determination was made based on the the downstream meniscus configuration. In the low capillary number case, low flow limit is estimated to be critical film thickness at which the apex of the downstream meniscus is in the same plane as the die-lip corner, indicating the onset of meniscus invasion to the gap. At high capillary number case, low-flow limit is estimated to be the thickness at which the standing wave of the film on the slide touches the coated film on the web. Predictions of the minimum thickness as a function of capillary number are plotted in Fig. 4.7, where the x axis, $\frac{\text{Ca}}{\text{Re}}$ is proportional to $\frac{1}{\text{thickness}}$. In addition to the minimum thickness prediction, the plot also contains maximum film thickness curve estimated with the equation (4.6). A curve marking the onset of vortex at the downstream meniscus is included inside the window as well. It is important to mark the conditions at which vortices occur since they are also a potential source of coating defects.

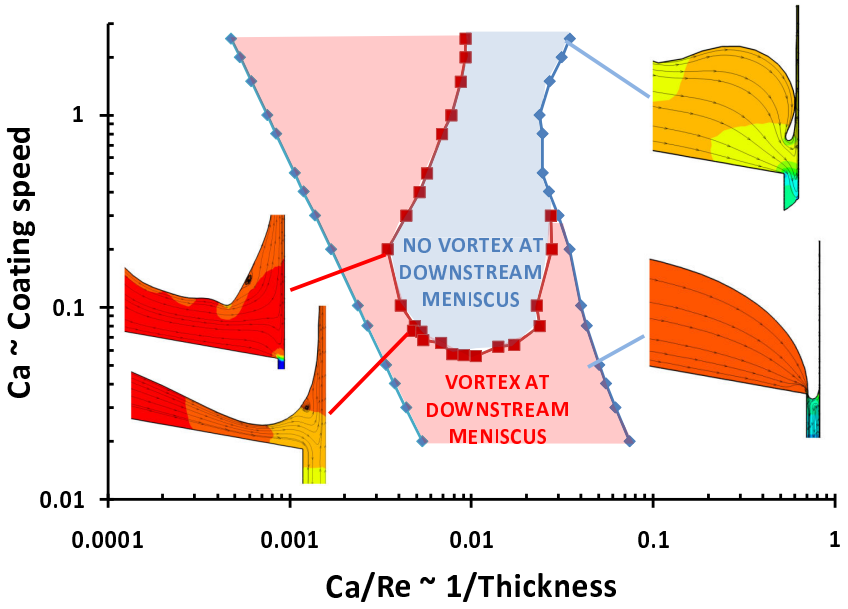

Figure 4.7: Flow limits of slide coating

Figure 4.7 shows that at low capillary number, the minimum thickness rises as capillary number falls, indicating that thinner coating requires slower coating speed. However, at high capillary number, the minimum thickness *falls* as capillary number *rises*, indicating that thinner coating can be achieved by increasing the coating speed. These different trends were caused by inertia, as explained in the next section. The flow limit window also shows that at low capillary number, vortex is always present at the downstream meniscus and it can be avoided by operating at moderate or higher capillary number and thin coating region.

As discussed before, the window presented in Fig. 4.7 was constructed based on the limiting states of 2-D flows. In reality, the flow may become unstable to the crossweb (3-D periodic) disturbances before the limiting states are achieved, making the practical operating window narrower than one presented. This issue is discussed in more detail later.

Effect of Inertia to Low Flow Limit

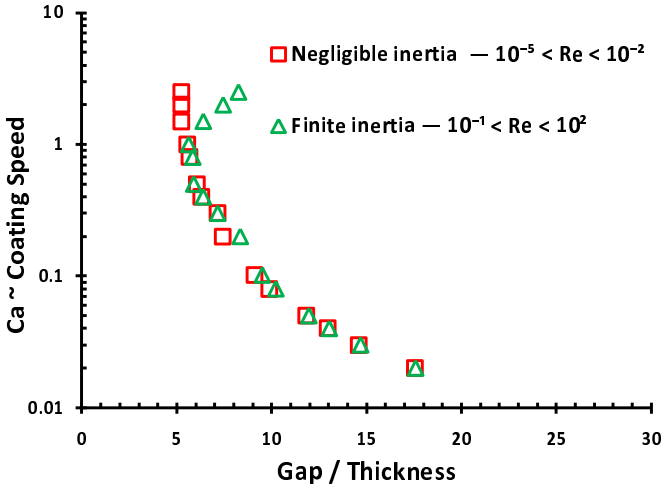

Figure 4.8: Effect of inertia to minimum thickness

Figure 4.8 shows the minimum thickness as defined previously at different values of Reynolds number. At negligible inertia, i.e. $\mathrm{Re} \ll 1$, the minimum thickness

monotonically rises as capillary number rises and at the case of finite inertia range, the minimum thickness falls as capillary number rises above a critical capillary number around 1. This finding suggests that inertia is responsible in delaying the onset of coating bead breakdown in low flow limit. The similar trend was also observed in the slot coating process by Carvalho and Kheshgi (2000).

Effect of Gap Width to Low Flow Limit

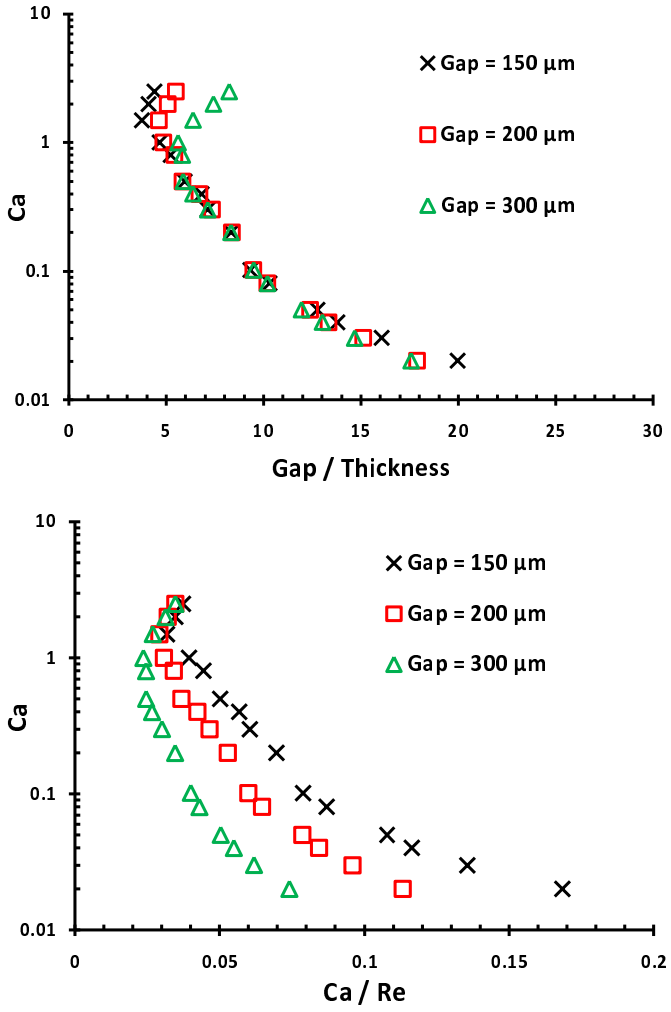

Figure 4.9: Effect of gap width to minimum thickness

The effect of gap width to the minimum thickness is shown in Fig. 4.9. The results are plotted as a function of gap-to-thickness ratio and capillary-to-Reynolds number ratio. The minimum thickness was found to be proportional to the gap width at low capillary number, and independent of the gap at high capillary number. This different behavior could be attributed to the proximity of the downstream meniscus to the gap. At low capillary number, low flow limit is caused by invasion of meniscus to the gap and smaller gap will allow smaller downstream meniscus before the onset of the bead breakup starts. Smaller downstream meniscus creates larger adverse pressure gradient to the flow along the web and leads to thinner coating. At higher capillary number, due to the relatively thick film on the slide, the meniscus will not invade the gap. Since the breakup occur away from the gap, the onset of breakup becomes independent of the gap width.

Effect of Die-Lip Shape to Low Flow Limit

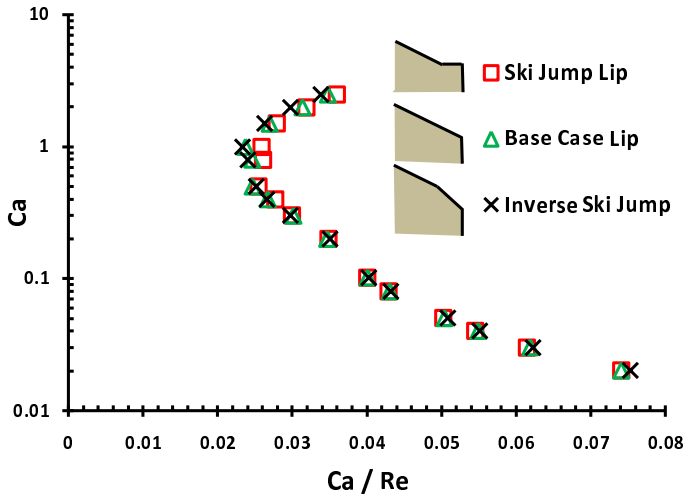

Figure 4.10: Effect of die-lip shape to minimum thickness

The effects of die lip geometry on the slide coating window has not been studied as well as in the case of slot coating. Jackson (1976); Isayama and Takehara (1981); Hirshburg and Christodoulou (1995) proposed a modification of the die-lip shape at the flow turnaround region in order to increase the maximum coating speed. However,

none of those patents substantiated their claims with systematic studies. In this work, we compared low flow limit predictions at three die-lip shapes: Ski jump, straight, which is the base case, and inverted ski jump. The predictions at different capillary number are shown at Fig. 4.10. As shown there, the effects of die-lip geometry are negligible at low capillary number regime, since the bead breakup is dictated by the gap width. At high capillary number regime, ski jump allows for slightly thinner coating due to delay of onset of meniscus touching the film on the web. As mentioned before, the flow states near the low flow limit may be unstable because of the highly curved meniscus. Therefore, this finding is subject to verification from onset of ribbing instability estimation covered in a later section.

Effect of Slide Inclination to Low Flow Limit

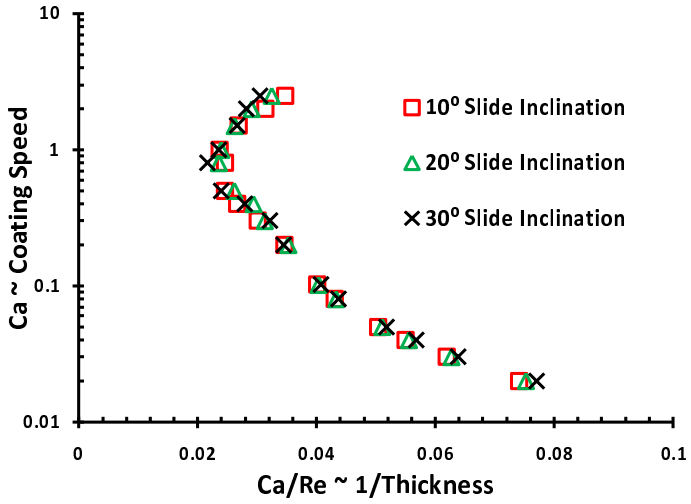

Figure 4.11: Effect of slide inclination to minimum thickness

The effect of slide inclination on the low flow limits is shown in Fig. 4.11. The slide inclination has no significant effect in the minimum thickness except at the high capillary number where slightly thinner coating can be achieved at a lower slide inclination. This improvement can attributed to the less meniscus confinement imposed by the slide and web surfaces.

4.4 Estimating Onset of Ribbing Instability

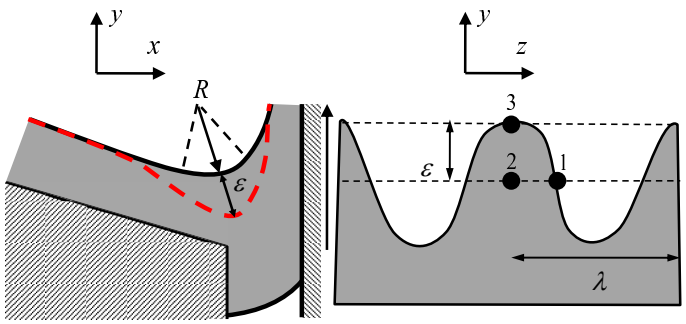

Figure 4.12: Sketch of the analysis of the ribbing instability

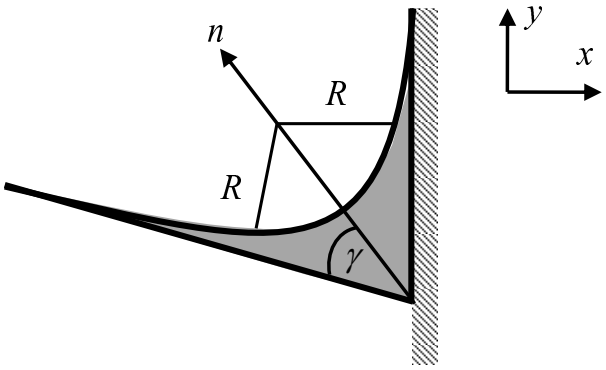

Figure 4.13: Estimating normal gradient of the meniscus curvature

Ribbing instability causes periodic thickness variation along the cross-web direction and can manifest as coating defect at the end product if the leveling rate is not fast enough. Furthermore, ribbing instability can also speed up coating bead breakdown since variation of coating thickness along the cross-web direction leads to variation of distance between the upstream and downstream menisci. The region with shorter distance will be the most vulnerable sites for bead breakup due to the menisci proximity to each other. The coating bead breakup can come from either the upstream meniscus due to low vacuum limit, or from the downstream meniscus due to low flow

limit. Ribbing instability shrinks the coating window.

Analysis on ribbing instability was first performed by Pearson (1960) where he identified the adverse pressure gradient underneath the curved meniscus to be the destablizing force that competes with the action of surface tension that tends to stretch the free surface. He recognized that a critical capillary number marks the onset of the ribbing instability. Pitts and Greiller (1961) then proposed a stability criterion based on spanned momentum balance along the perturbed free surface. They considered the pressure gradient to be the only driving force for the instability. The flow is unstable when the pressure beneath the crest of the wave - location 2 in Fig. 4.12 is less than the pressure in the midpoint between the crest and the trough - location 1 in Fig. 4.12 leading to a flow from the trough to the crest that promotes the growth of the wave.

Graham (2003) later generalized the destabilizing force to include viscous and viscoelastic stresses. Zevallos et al. (2005) combined stability criterion from Pitts and Greiller (1961) and Graham (2003) to form the following stability criterion that they employed to analyze ribbing instability of forward roll coating of viscoelastic liquids. The stability criterion is that the free surface is stable when:

$$\frac{\tau_{tt} - \tau_{nn}}{R} - \rho g_n - \frac{\sigma}{R^2}\frac{\mathrm{d}R}{dn} < 0 \tag{4.7}$$

where τ_{tt} and τ_{nn} are the normal stresses tangent and normal to the free surface respectively, R is the radius of curvature of the meniscus, and $\frac{\mathrm{d}R}{dn}$ is the normal gradient of the radius of curvature. In the case of slide coating, it can be estimated based on the geometrical confinement imposed by the slide and the web surfaces, shown in Fig. 4.13. The radius of curvature of the meniscus can be related with the normal distance from the slide - web intersection as $\frac{R}{n} = \tan\gamma$, and the normal curvature gradient then follows as $\frac{\mathrm{d}R}{dn} = \tan\gamma$. The bisecting angle γ is estimated to be the half angle between the slide and the web $\frac{\alpha}{2}$.

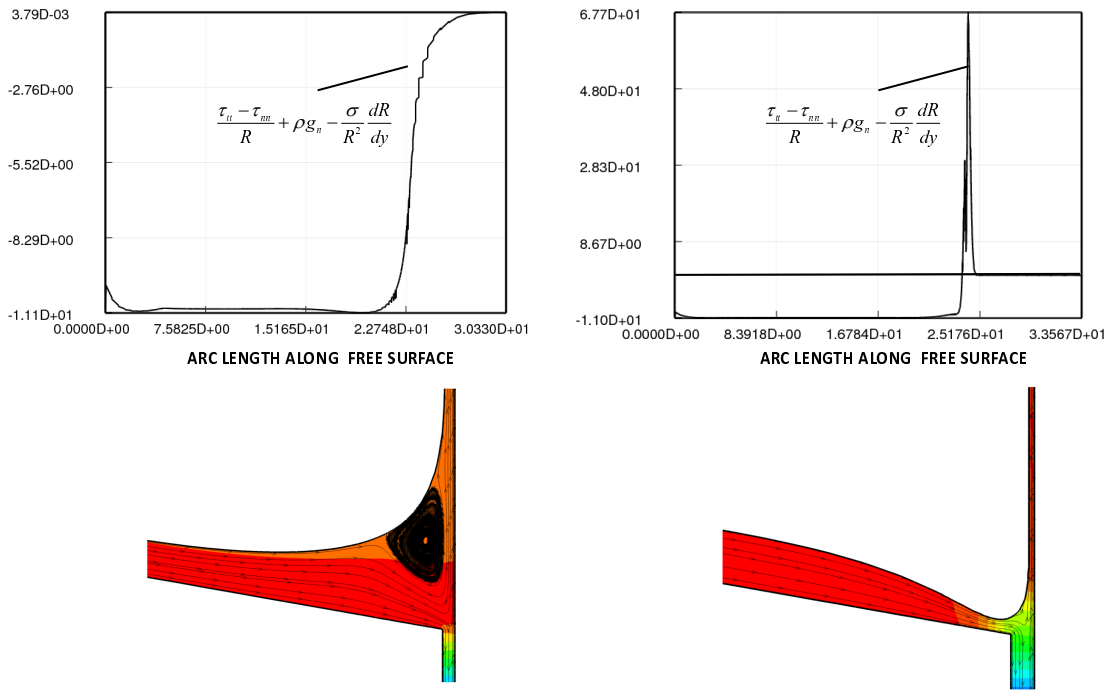

(a) Free of ribbing - Ca = 0.1 Re = 4 (b) Prone to ribbing - Ca = 0.1 Re = 2

Figure 4.14: Stability criterion values along free surface and the corresponding flow state

This criterion was employed in this study to estimate the onset of ribbing instabilities inside the slide coating window. The left hand side of equation 4.7 was evaluated along the free surface and when it becomes positive, the flow state was declared to be prone to ribbing. Figure 4.14 shows examples of the stability criterion evaluation along the arc length of free surface at two flow states: Reynolds number Re = 4, which is stable, and Re = 2, which is unstable to ribbing. The flow is stable when the criterion is all negative along the free surface and unstable when it becomes positive at any point along the free surface. At these examples, the stable flow state has a vortex at the downstream meniscus and the unstable one does not. As shown later, this finding is generally true for a moderate or higher value of capillary number.

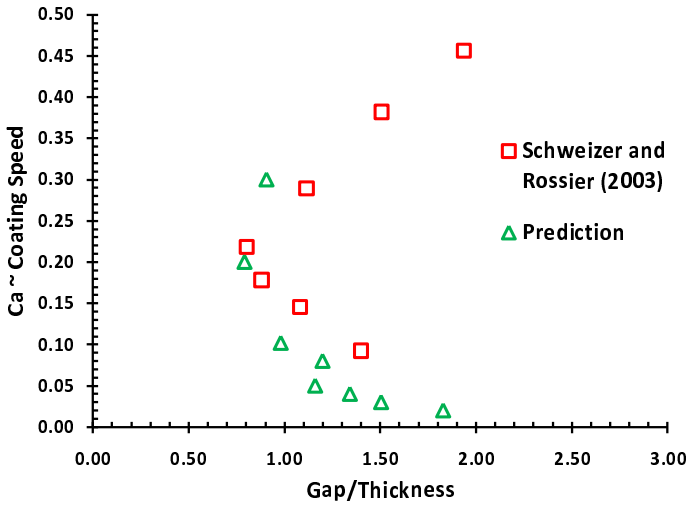

Figure 4.15: Comparison with experimental ribbing data reported by Schweizer and Rossier (2003)

Predictions of onset of ribbing instability at different capillary numbers are compared with experimental values reported by Schweizer and Rossier (2003) and the result is shown in Fig.4.15. The prediction of the onset of ribbing instability agrees well to what was reported from experiment.

With simple model to predict ribbing instability validated, we now include the onset of ribbing instability in the coating window and the updated coating window is presented in Fig. 4.16. At capillary number of 0.08 and higher, the curve that represents the onset of ribbing lies very closely to the onset of the downstream meniscus vortex, indicating that ribbing-free conditions will most likely have a vortex attached to the free surface. The same trade-off between ribbing-free and vortex-free operation is also encountered in the forward roll coating flow (Coyle et al., 1986). As the coating thickness decreases, at a given speed, the ribbing will be formed and later on evolve into rivulets at low flow limit. At moderate and high Ca, the critical thickness at the onset of ribbing falls as speed rises, indicating that thinner uniform (free of ribbing) coating can be obtained at higher speed and free of ribbing.

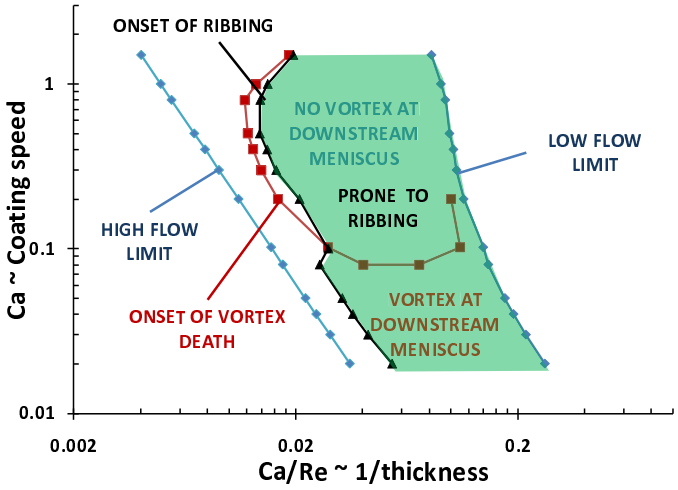

Figure 4.16: Flow limits of slide coating with onset of ribbing

The effect of die-lip to the onset of ribbing is also explored and the results are presented in Fig. 4.17. The die-lip geometry did not affect the onset of ribbing significantly. This can be attributed to the location of meniscus being far away from the die-lip such that changing the die-lip geometry does not change the flow at meniscus and meniscus shape significantly.

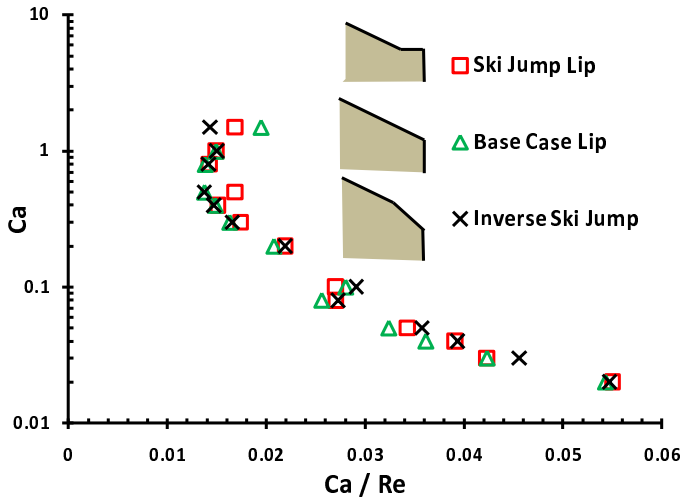

Figure 4.17: Effect of die-lip geometry to onset of ribbing

4.5 Concluding Remarks

Theoretical modeling of slide coating flow reveals coating bead breakup mechanisms at low vacuum, high vacuum, and low flow limits. Both low and high vacuum limits initiate the bead breakdown from the upstream meniscus. Low vacuum limit manifest in the formation of alternating dry and wet lanes referred to as rivulets and high vacuum limit leads to weeping where some of the liquid flows to the vacuum chamber instead of being coated. Low flow limit initiate the bead breakdown from the downstream meniscus and manifest as rivulets as well.

Vacuum limits window shows that thinner coating can be achieved by maintaining higher applied vacuum underneath the coating bead. Flow limits window shows that minimum thickness increases as coating speed increases until it reaches a critical capillary number where the trend is reversed. Inertia is responsible for the reverse of the trend. The minimum thickness is proportional to the gap width at low capillary number regime and independent of the gap at high capillary number due to the proximity of the downstream meniscus to the gap. At low capillary number, the breakup occurs at the gap, at high capillary number, away from the gap. Minimum thickness is not affected by die-lip shape and slide inclination.

A simple stability criterion can be applied to determine the onset of ribbing without performing three-dimensional stability analysis. The prediction of the onset of ribbing agrees qualitatively with experimental results reported by other researchers. Based on the prediction, onset of ribbing almost coincides with the onset of vortex attached to the downstream meniscus. This finding indicates that ribbing-free operation will have vortex present at the downstream meniscus.

Chapter 5

Coating Window by Experiments

5.1 Introduction

Slide coating, like all coating processes, is subjected to fluid mechanical instabilities that cause failure of coating. Most of the experimental studies in slide coating windows in the past were focused on the types of coating failure that occur and the corresponding critical operating conditions. Tallmadge et al. (1979) reported lower and upper coating speed limits under different flow rates, gap widths, and viscosities, however since they did not apply vacuum, it was not clear whether the limitations that they encountered could be overcome by applying vacuum. Gutoff and Kendrick (1987) reported high speed limit or low flow limit at different viscosities and gap widths and they demonstrated that thinner coating can be achieved when vacuum is applied underneath the bead. Chen (1992) added vacuum limits in the operability limits of slide coating and Hens and van Abbenyen (1997) added experimental values of ribbing and rivulets formation. However, mechanisms of how the coating bead breaks and manifest into these coating failures, have not been addressed. One reason is that the none of these studies employed a perceptive view through a transparent back-up roll to visualize the floe and the failure mechanism associated to each coating defect.

In contrast, slot coating window is fairly well understood, the result of perspective through-the-roll viewing and a sequence of theoretical modeling in combination with qualitative understanding of the physical mechanisms that could be involved. Romero et al (2004) employed the aforementioned tools and were able to successfully extract bead break-up mechanisms at low-vacuum limit, high-vacuum limit, and low-flow limit. The goal of the work in this chapter is to extend the methods employed by Romero et al. (2004) to slide coating. We probed the bead breakup mechanisms with the aid of through-the-roll viewing of the bead at low-vacuum limit, high-vacuum limit, and low-flow limit. We also investigated the flow states that lie beyond the operability limits that set them up. The effects of gap height and slide inclination were explored as well. .

5.2 Experimental Apparatus

The schematic of the benchtop slide coater apparatus used in this study is shown in Fig. 5.1. The coating liquid is supplied to the coating die via a zenith gear pump (Model No. BMC-5337-27.8cc/rev, Parker Hannifin Co. Zenith Division, Sanford, NC 27330). The flow rate is monitored with a Coriolis mass flowmeter (model MFC 100/MFS 3000, KROHNE Americ Inc, Peabody, Massachusetts). The slide die is 12.8 cm (5 in) wide and positioned above a mounting block that sets the inclination of the die: 10^o, 20^o, and 30^o. The mounting block is mounted to a positioning plate that is used to adjust the gap between die lip and the glass roll. The positioning plate can be moved by turning four finely thread 1/4 inches screws and its position is monitored by two dial indicators (Model No 2119-51, Mitutoyo, Japan) with 1μm precision.

A vacuum chamber is installed beneath the slide die and the roll. It consists of two sections: a low pressure section directly underneath the bead and a vacuum section located further upstream. The purpose of the addition of the low pressure section, which was patented by Krussig (1982), is to dampen fluctuations in the vacuum cham-

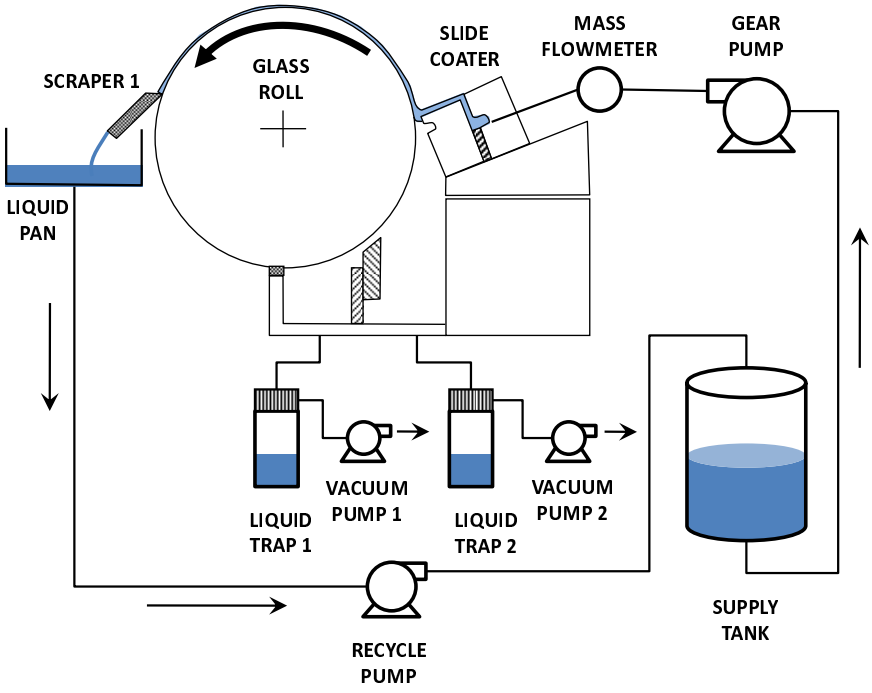

Figure 5.1: Schematic of slide coating apparatus

ber. The combined volume of both chambers is 2000 cm^3, the largest volume that the space constraints allowed. Vacuum from each section is drawn from a three-ring compressor vacuum pump ((Model VFC084P-5T, Fuji Electric Co, Tokyo, Japan) and controlled with a butterfly valve. The pressure right underneath the coating bead is monitored by a pressure transducer (Model UPS 3000 AEB, Eaton Consolidated Controls, Pressure Sensors Division, Bethel, Connecticut) with the precision in the order of 35 Pa.

The liquid is applied directly onto an overhang glass roll instead of a web in order to exclude the complexities of web handling from the study. The advantage of using this overhang glass roll is that it allows for front view visualization of the coating bead by installing a mirror inside the overhang, as shown in Fig. 5.2, provided that the coating liquid is transparent as well. The glass roll was manufactured by Professional Instrument Company, Hopkins, Minnesota and has dimension of 21.6 cm in diameter and 10.6 cm in length. The roll has high precision with maximum run-out of 0.5μm and driven through a pulley system by a permanent magnet DC motor (Model no. SRF5556-3928-82BC, Pacific Scientific, Rockford, Illinois). The motor is controlled by a feedback controller (Model M-Drive, Fenner Digital Control, Osseo, Minnesota).

The coating liquid used was water-glycerine solution with a viscosity range of 38 - 42 cP, measured with a Brookfield viscometer with an LDV cylinder fixture (Model LVT, Brookfield Eng. Lab., Soughton, Mass.), and surface tension range of 62 - 64 dyne/cm, measured with a digital tensiometer (Model K10ST, Krss USA, Charlotte, North Carolina). Measurements of liquid properties are performed during each run.

5.3 Visualization of Coating Bead Breakdown

Flow visualization of slide coating is performed from two different views. First, as mentioned before, is a front view for observing the menisci locations and their shapes along the cross roll direction, obtained by positioning a high speed camera (Photron

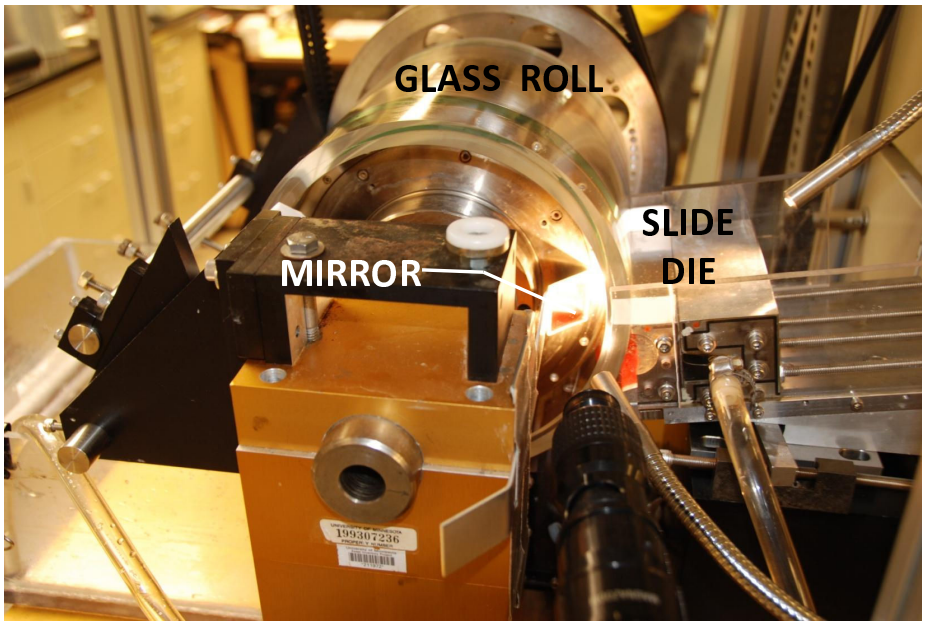

Figure 5.2: Photograph of the experiment apparatus

FASTCAM Ultima APX) facing the mirror installed inside the overhang of the glass roll. The camera was recording at a speed of 500 fps with a 1024 X 1024 resolution. The second view is the side view for observing the free surface configuration, obtained by injecting silvered spheres particles (14 $\mu(m)$ diameters, Conduct-o-Fil S-5000-S3, Potter Industries, NJ), shining a thin sheet of laser (672.8 nm wavelength, 340 mW, Magnum-670-500-10°), and capturing the shape with the high speed camera. The sample photographs of both views are shown in Fig. 5.3.

The first objective of the study is to uncover bead breakup mechanisms by taking advantage of the available high speed camera. The observation results and the analysis are presented below.

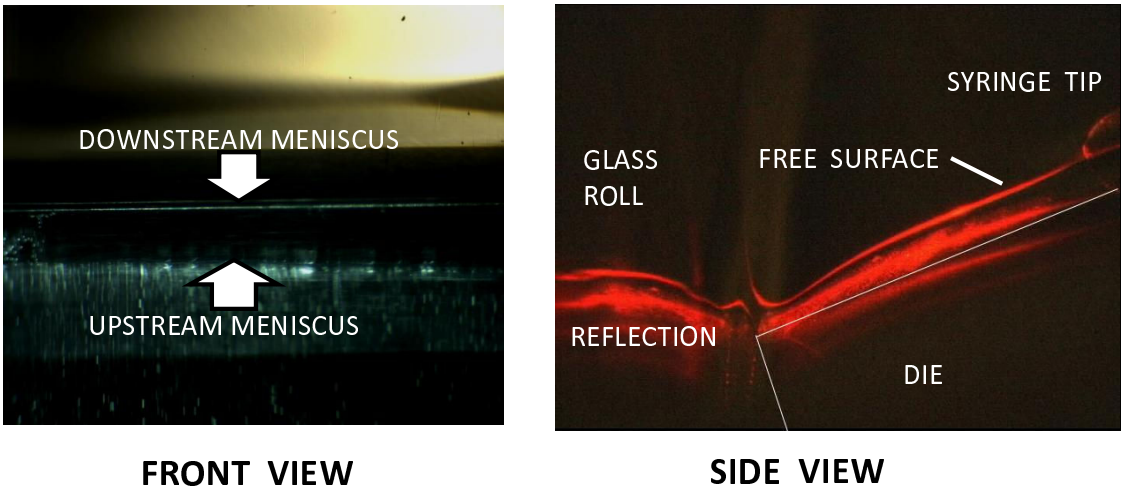

Figure 5.3: Samples of photographs obtained with flow visualization

5.3.1 Vacuum Limits

Figures 5.4 and 5.5 show bead breakup mechanisms at low and high vacuum limits respectively. At low vacuum limit, the upstream meniscus moves toward the edge of the die lip and an air finger pokes through the coating bead. This results in the formation of periodic alternating dry and wet lanes known as rivulets. This condition can be reversed by raising the applied vacuum underneath and allowing the coating bead to heal. At high vacuum limit, the coating liquid leaks to the vacuum chamber underneath and if the applied vacuum is strong enough, cause the coating bead breakup to break and forms passage of air flow to the chamber, as shown in Fig. 5.5. In both limits, the breakup is initiated from the upstream meniscus, just as predicted from the Chapter 4. The same phenomena was also reported in the slot coating flow visualization study by Romero et al. (2004).

Figure 5.5: Bead breakup mechanism at high vacuum limit

5.3.2 Low Flow Limit

Figure 5.4 shows the coating bead breakup mechanism in the low flow limit. At sufficiently low flow rate, ribbing instability at the downstream meniscus creates periodic ribs pattern across the coating. Then, an air finger pokes through the crest region of the coating bead, as shown in the figure, creating rivulets. Both low vacuum and low flow limits failures lead to rivulet flow state, however they come from different mechanisms. At low vacuum limit, upstream meniscus is responsible for the bead breakup while at low flow limit, the downstream meniscus is. This finding is supported by theoretical modeling performed at Chapter 4 and also reported at the case of slot

coating by Romero et al. (2004).

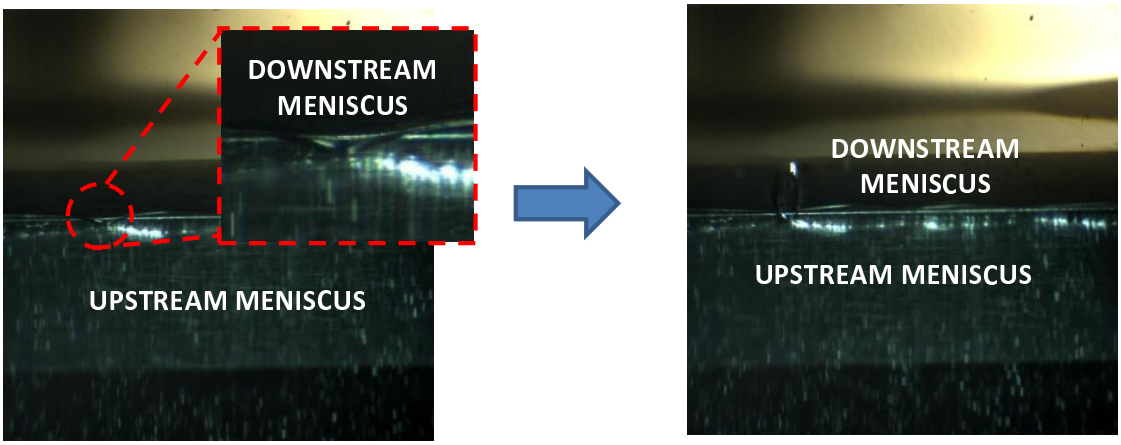

Figure 5.6: Bead breakup mechanism at low flow limit

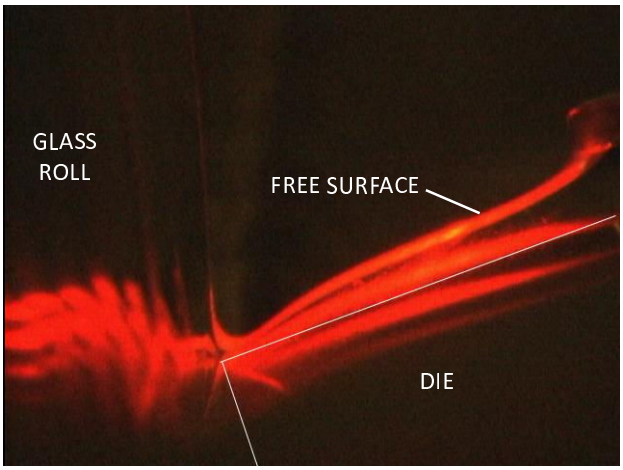

Figure 5.7: Free surface shape at near low flow limit

5.3.3 Edge Effects

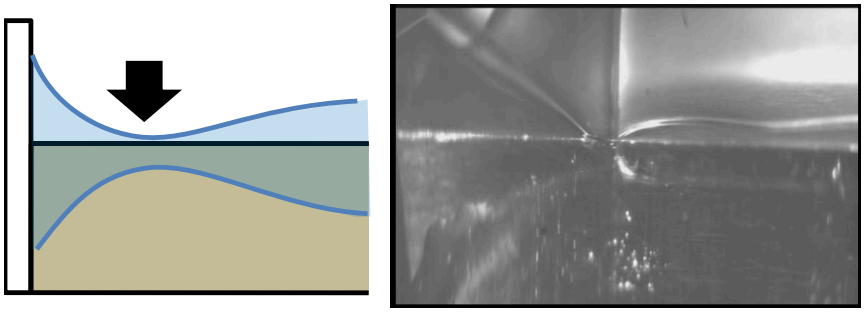

Figure 5.8: Edge effects in low vacuum limit

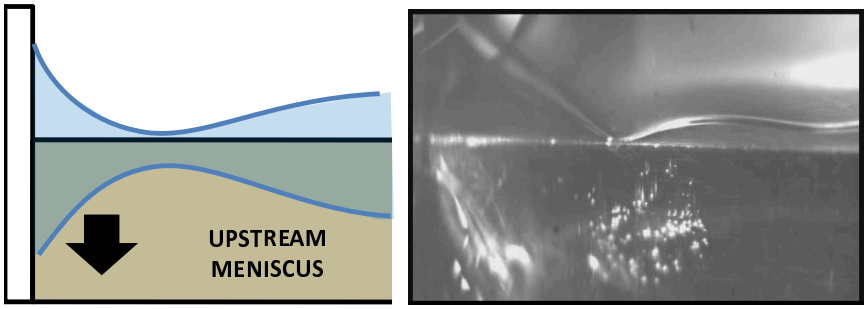

Figure 5.9: Edge effects in high vacuum limit

In slide coating operation, edge effects can severely limit the operability of slide coating, just as in the curtain coating process. Edge effects are usually caused by liquid wetting the edge that creates local thickening of the film flow at the region. The thick film at the edge starves the flow at the immediate region and creates a region of thin film. This thin film region is more susceptible to coating bead breakdown in the low and high vacuum limits, as shown in Figs. 5.8 and 5.9 respectively. If not handled properly, edge effects will shrink the operability windows in both vacuum and low flow limits. This edge problem has been tackled in the past by controlling the wetting at the edges such that the wetting line makes 0^o angle with the film free surface. This solution was patented by Yapel et al. (1998).

5.4 Flow Limits by Experiments

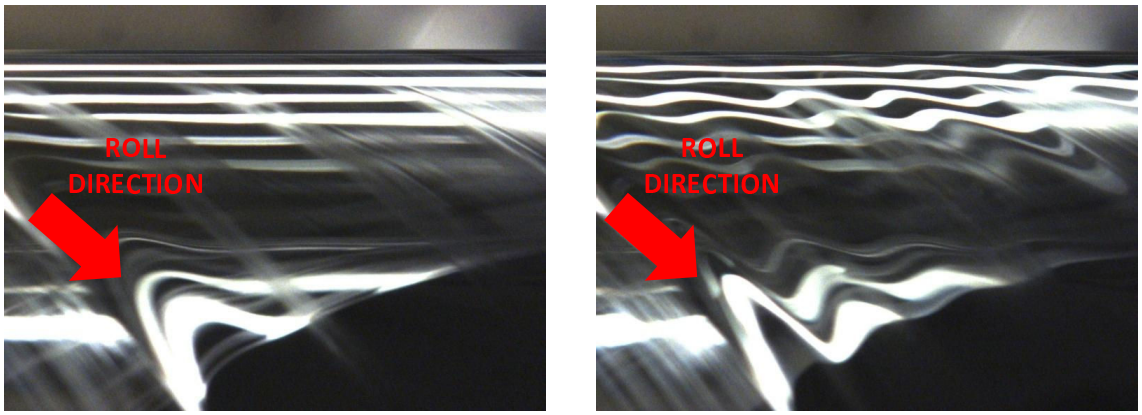

Figure 5.10: Reflection of fluorescent light tubes as a mean for detecting ribbing instability

The procedure used here to determine the ribbing and low flow limits at a given roll speed was:

1. The pump speed is set to deliver relatively thick coating, i.e. approximately about the gap width thick. A high enough vacuum is applied to move the upstream meniscus to the die face, but not too much that will cause edge weeping. A slender wooden stick is then used to distribute the liquid on the slide surface and to make the coating bead continuous - a common expedient technique in the coating practice

2. The flow rate is lowered gradually and the flow is allowed to reach steady state. If the upstream meniscus moves toward the die-lip edge, more vacuum is applied to return it to approximately its original location.

3. Ribbing instability is detected by observing the reflection of fluorescent light tubes on the coated layer. When ribs occur, the reflection of the tubes becomes wavy, as shown in Fig. 5.10, due to the nonuniformity film profile over the roll.

4. Low flow limit is determined when rivulets are formed and the coating bead cannot be reestablished by increasing vacuum and distributing the liquid with the wooden stick. The minimum film thickness is calculated by dividing the flow rate per unit width by the roll speed.

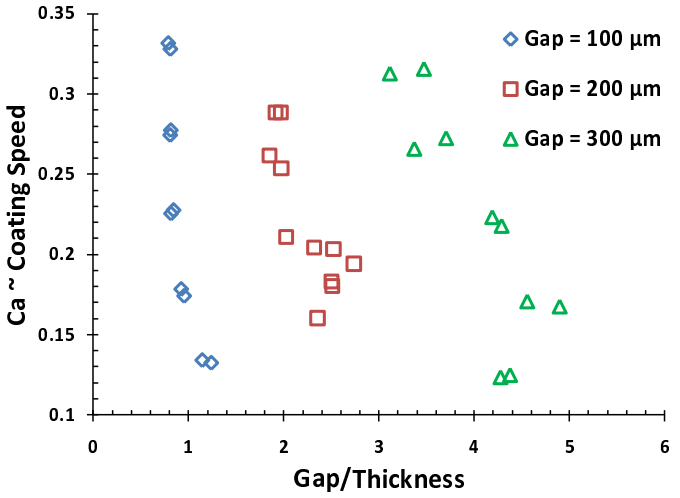

(a)

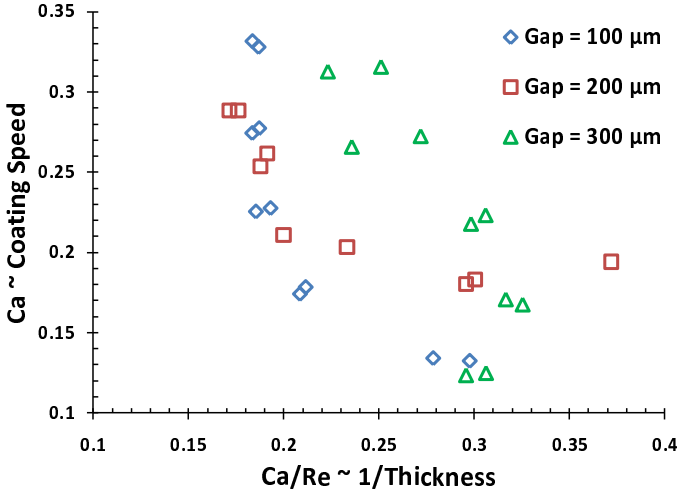

(b)

Figure 5.11: Low flow limit measurements at different gap widths

Figures 5.11 and 5.12 show the experimental values of minimum thickness and onset of ribbing instabilities as a function of coating speed at different gap width respectively.

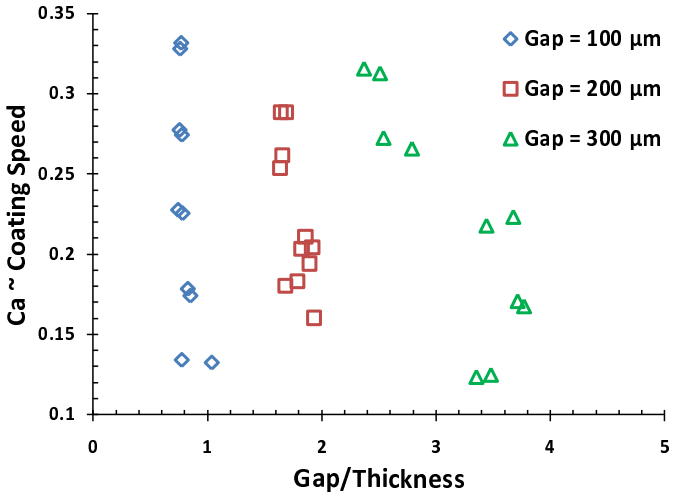

(a)

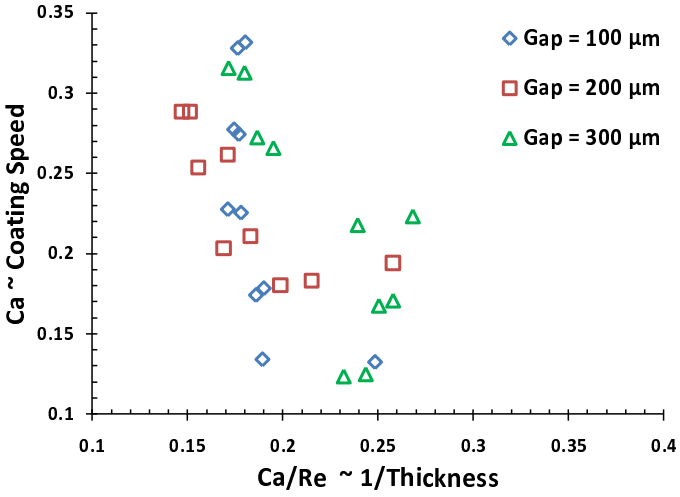

(b)

Figure 5.12: Ribbing limit measurements at different gap widths

The minimum thickness and onset of ribbing *increases* as the gap width *decreases*, suggesting that thinner uniform coating is achieved at *larger gap*. This finding is in contrary with the results of the theoretical prediction reported in the Chapter 4. This finding indicates other factors that are not considered in the model might play a dominant role in the low flow limit experiments. The possible candidates are edge effects and fluctuations that come from the vacuum chamber and roll run-out. At

smaller gap, the flow becomes more susceptible to vacuum fluctuations and roll run-out, adding more disturbances to the flow state and transforms into ribbing flow state at higher flow rate than in larger gap. As flow rate decreases even more, the crests and troughs at the downstream meniscus grow until the bead break due to low flow limit.

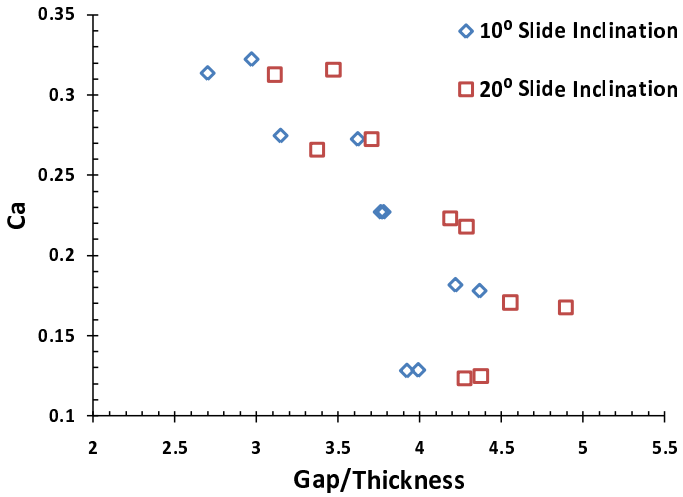

Figure 5.13: Low flow limit measurements at different slide inclinations

Figs. 5.13 and 5.14 shows the minimum thickness and onset of ribbing instabilities as a function of coating speed at slide inclination respectively. Both limits are not affected by slide inclination and this finding is consistent with theoretical predictions at the given capillary number range.

Comparison of experimental ribbing and low flow limits with those predicted from the theory is shown at Fig. 5.15. Although the theory can predict the general trend of these flow limits change with coating speed, the values of these limits do not match. The theory predicts onset of ribbing to occur at higher flow rate than the experiment. This discrepancy can be attributed to the leveling of the coated layer before it arrives at the observation point or a lack of sensitivity in the detection method. In contrast, the theory predicts low flow limit to be at lower flow rate than the experiment. This

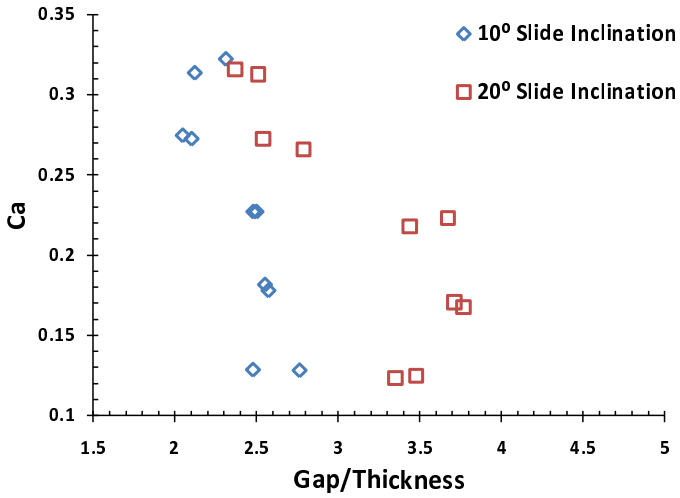

Figure 5.14: Ribbing limit measurements at different slide inclinations

discrepancy can be attributed to edge effects and ribbing instability that tend to speed up coating bead breakdown due to the growth of crests and troughs at the downstream meniscus.

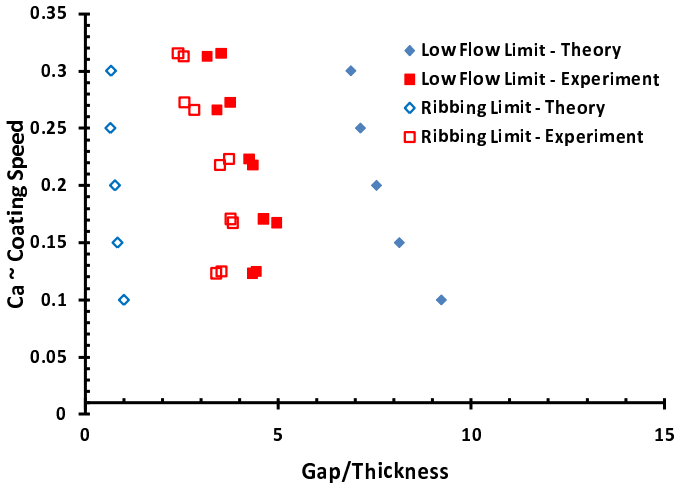

Figure 5.15: Comparison of flow limits with theoretical prediction - gap = 300 μm

5.5 Concluding Remarks

Flow visualization from a benchtop slide coater reveals coating bead breakup mechanisms at low vacuum, high vacuum, and low flow limits. Both low and high vacuum limits initiate the bead breakdown from the upstream meniscus. Low vacuum limit manifest through the formation of alternating dry and wet lanes referred as rivulets and high vacuum limit leads to weeping where some of the liquids flow to the vacuum chamber instead of being coated. Low flow limit initiate the bead breakdown from the downstream meniscus and manifest as rivulets as well.

Experimental values of the minimum thickness and onset of ribbing matches theoretical predictions qualitatively. The experimental values of minimum thickness are higher than the theoretical prediction and this discrepancy can be attributed to edge effects and ribbing instability that tend to speed up coating bead breakdown. The experimental thickness values corresponding to the onset of ribbing are found to be lower than the theoretical predictions due to leveling of the coated layer before it arrives at the observation point and a lack of sensitivity in the detection method.

Chapter 6

Conclusions

Slide coating is the leading method for simultaneous multilayer coating. The thickness of the coated layer is set solely by the flow rate and speed, and independent from other process conditions. The uniformity of the layer, however, can strongly depend on the other process conditions and uniform coating can only be achieved in certain ranges of operating conditions. The parameter space in operating conditions where coating is feasible is referred as coating window. Slide coating window, even for single-layer case, is not well understood as the slot coating window. Slot coating operability limits have been well studied and the bead breakup mechanisms have been identified as well. The goals of this thesis are to uncover the mechanisms of coating bead breakdown at the edges of the windows and to predict critical operating conditions corresponding to the bead breakup. The study was initiated by developing a one-dimensional viscocapillary model of slide coating.

A critical review of the available viscocapillary model is presented in Chapter 2. The model consists of spliced solutions of film profile equations of the flow falling down the slide and up the moving web. We have demonstrated that with the appropriate formulation, a simplified 1-D viscocapillary model of slide coating can be constructed and its range of validity are governed by the limitation of the approximations employed: Small inclination of film thickness, low capillary number, and low Reynolds

number. The approximation worsen at the bead zone, as expected, where in the 1-D viscocapillary model it was assumed to be a static pool and in a realistic coating operation, it is not so. The results show that viscocapillary model are accurate only at low capillary numbers and small gap-to-thickness ratio.

The accuracy of the model can be improved by augmenting it with full 2-D Navier-Stokes theory at the coating bead region, where the flow is fully two-dimensional. These regions, slide, bead, and web regions, need to be connected with matching conditions and in principle, there are multiple possible combinations of matching conditions that can be employed. However, we demonstrated that only one combination works well. The model only requires about 60 % less memory and it is twice faster to compute than solutions of the full 2-D model. The hybrid model is as accurate as the full 2-D model, providing that the matching conditions are assigned properly and their locations are far enough such that the approximations employed in deriving the viscocapillary model remain valid there.

Future development of the model should incorporate implementation of asymptotic inflow and outflow boundary conditions at slide upstream and web downstream regions. Applying asymptotic boundary conditions allow the domain length to be shorten even more without loss of accuracy, just as demonstrated in Chapter 2. Another suggested improvement is to include the matching locations to be unknown as well. In this manner, locations of the matching points have to be solved as well as the rest of degrees of freedoms such that the matchings are made in the proper location. Conditions that can be used to set the locations are numerous, but I believe the most sensible ones are in the form of setting the residuals of the film profile equations, evaluated at the matching planes, to be within a specified tolerance. In this manner, the matching planes are always located at regions where the assumptions used in deriving the film profile equations are still valid. The resulting matching locations also need to be validated by testing the solution sensitivity to the matching locations. The appropriate matching locations should be where the solution is invariant by moving the slide-bead matching plane slightly upstream and bead-web plane downstream.

Theoretical modeling and flow visualization of slide coating flow reveal bead breakup mechanisms at low vacuum, high vacuum, and low flow limits. Both low and high vacuum limits initiate the bead breakdown from the upstream meniscus. Low vacuum limit manifest through the formation of alternating dry and wet lanes referred as rivulets and high vacuum limit leads to weeping where some of the liquid flows to the vacuum chamber instead of being coated. Low flow limit initiate the bead breakdown from the downstream meniscus and manifest as rivulets as well.

Theoretical prediction of vacuum limits window shows that thinner coating can be achieved by maintaining higher applied vacuum underneath the coating bead and this is consistent with experimental observation. Flow limits window show that minimum thickness increases as coating speed increases until it reaches a critical capillary number where the trend is reversed. This is not seen in the experiment due to relatively low Reynolds and capillary numbers in the experimental conditions - $\mathrm{Re} < 2$ and capillary number - $\mathrm{Ca} < 0.4$. The values of the minimum thickness found from the experiment are consistently higher than what is predicted by the theory. This discrepancy can be attributed to edge effects and ribbing instability that tend to speed up coating bead breakdown.

A simple stability criterion was used to determine the onset of ribbing without performing three-dimensional stability analysis. The prediction of the onset of ribbing agrees qualitatively with experimental results reported by other researchers but not with the flow visualization experiments performed in this study. The discrepancy can be attributed to the leveling of the coated layer before it arrives at the observation point or a lack of sensitivity in the detection method.

Theoretical prediction reveals that minimum thickness and onset of ribbing are not affected by the die-lip shape, unlike in slot coating. This lack of effect from die-lip shape is due to the lack of confinement of the coating bead from the solid surface.

Coating bead in slot coating is more contained and therefore its pressure and flow fields can be altered more by the change of die geometry. However, the geometry of the feed slot can affect the coating quality significantly by regulating the position of the static contact line or interlayer separating line, in the case of multilayer coating

Future development of this study is first, to extend the analysis to two-layer or more, since the chief reason of the development of slide coating is to be able to coat multi-layer precisely. Another suggested extension is to study the effect of rheology to the operability windows.

Bibliography

Beguin, A. E. 1954 Method of coating strip material. US Patent No. 2,681,294.

Benjamin, D. F. 1994 *Roll coating flows and multiple roll systems*. PhD thesis University of Minnesota Published by University Microfilms International, Ann Arbor, MI.

Bixler, N. E. 1982 *Stability of coating flow*. PhD thesis University of Minnesota Published by University Microfilms International, Ann Arbor, MI.

Bolstad, J. H. and Keller, H. B. 1986 A multigrid continuation method for elliptic problems with folds. *SIAM J. Sci. Stat. Comput.* **7** 1081 – 1104.

Carvalho, M. S. and Kheshgi, H. S. 2000 Low flow limit in slot coating: Theory and experiments. *AICHE J.* **46** 1907 – 1917.

Chen, K. S. 1992 *Studies of multilayer slide coating and related processes*. PhD thesis University of Minnesota Published by University Microfilms International, Ann Arbor, MI.

Christodoulou, K. N. 1990 *Computational physics of slide coating flow*. PhD thesis University of Minnesota Published by University Microfilms International, Ann Arbor, MI.

Christodoulou, K. N. and Scriven, L. E. 1989 The fluid mechanics of slide coating. *J. Fluid Mech.* **208** 321 – 354.

Coyle, D. J., Macosko, C. W. and Scriven, L. E. 1986 Film-splitting flows in forward roll coating. *J. Fluid Mech.* **71** 183 – 207.

de Santos, J. M. 1991 *Two-phase cocurrent downflow through constricted passages.* PhD thesis University of Minnesota Published by University Microfilms International, Ann Arbor, MI.

Fuchigami, S. 2005 Challenges and opportunities in flat panel industry. Proceeding of the eighth international conference on web handling. Stillwalter, OK.

Galehouse, D. and Colt, J. 1984 Simplified analytical solutions of the free fluid surfaces associated with slide coating. AICHE. Ann. Meeting, Atlanta, GA, March 12, 1984.

Gates, I. D. 1999 *Slot coating flows: Feasibility, quality.* PhD thesis University of Minnesota Published by University Microfilms International, Ann Arbor, MI.

Graham, M. D. 2003 Interfacial hoop stress and instability of viscoelastic free surface flows. *Phys. Fluids* **15** 1702 – 1710.

Gutoff, E. B. and Kendrick, C. E. 1987 Low flow limits of coatability on a slide coater. *A.I.C.H.E. J.* **33** [No. 1] 141 – 145.

Hens, J. and Boiy, L. 1986 Operations of the bead of a pre-metered coating device. *Chem. Eng. Sci* **41** 1827 – 1831.

Hens, J. and van Abbenyen, W. 1997 Slide coating. In S. F. Kistler and P. M. Schweizer (eds), *Liquid film coating* 427 – 462 Chapman and Hall, London, UK.

Higgins, B. G. and Scriven, L. E. 1979 Interfacial shape and evolution equations for liquid films and other viscocapillary flows. *Ind. Eng. Chem. Fund.* **18** [No. 3] 208 – 215.

Higgins, B. G. and Scriven, L. E. 1980 Capillary pressure and viscous pressure drop set bounds on coating bead operability. *Chem. Eng. Sci.* **35** 673 – 682.

Hirshburg, R. I. and Christodoulou, K. N. 1995 Dual geometry for slide-bead coating. US Patent No. 5,458,925.

Huh, C. and Scriven, L. E. 1971 Hydrodynamic model of steady movement of a solid/liquid/fluid contact line. *J. Coll. Int. Sci.* **35** 85 – 101.

Isayama, S. and Takehara, N. 1981 Coating apparatus. US Patent No. 4,299,188.

Jackson, B. W. 1976 Apparatus for coating a substrate. US Patent No. 3,993,019.

Jung, H. W., Lee, J. S., Hyun, J. C., Kim, S. J. and Scriven, L. E. 2004 Simplified modeling of slide-fed curtain coating flow. *Korea Australia Rheology J.* **16** [No. 4] 227 – 233.

Kheshgi, H. S. and Scriven, L. E. 1979 Rising film flow: first-order approximation solved. *Bull. Amer. Phys. Soc.* **25** 1131 –.

Kistler, S. F. 1984 *The fluid mechanics of curtain coating and related viscous free surface flows with contact lines.* PhD thesis University of Minnesota Published by University Microfilms International, Ann Arbor, MI.

Kistler, S. F. and Scriven, L. E. 1979 Falling film flow: first-order approximation solved. *Bull. Amer. Phys. Soc.* **24** 1131 –.

Kistler, S. F. and Scriven, L. E. 1983 Coating flow. In J. M. Pearson and S. M. Richardson (eds), *Computational Analysis of Polymer Processing* Applied Science Publishers, London, UK.

Kolb, W. B. and Huelsman, G. L. 2004 Magnetic recording media having specific wet thickness and coating methods. US Patent No. 6,733,906.

Krussig, K. F. 1982 Apparatus for coating a web with a viscous coating material. US Patent No. 4,335,672.

Lee, K. Y., Liu, L. D. and Liu, T. J. 1992 Minimum wet thickness in extrusion slot. *Chem. Eng. Sci* **47** [No. 7] 1703 – 1713.

Mercier, J., Torpey, W. and Russell, T. A. 1956 Multiple coating apparatus. US Patent No. 2,761,419.

Nagashima, K. 1993 *Slide coating flow: splice passage.* M.S. thesis University of Minnesota.

Nagashima, K. 2004 Viscocapillary modelling of slide coating flow. *Ind. Coating Res.* **5** 81 – 106.

Park, E. 2008 *Physics of coating tensioned-web over slot die.* PhD thesis University of Minnesota Published by University Microfilms International, Ann Arbor, MI.

Pearson, J. R. A. 1960 The stability of uniform viscous flow under rollers and spreaders. *J. Fluid. Mech.* **7** 481 – 500.

Pitts, E. and Greiller, J. 1961 The flow of thin liquid films between rollers. *J. Fluid. Mech.* **11** 33 – 50.

Romero, O. J., Suszynski, W. J., Carvalho, M. S. and Scriven, L. E. 2004 Low-flow limit in slot coating of dilute solutions of high molecular weight polymer. *J. Non. Newt. Fluid. Mech.* **118** 137 – 156.

Ruschak, K. J. 1976 Limiting flow in a pre-metered coating device. *Chem. Eng. Sci.* **31** 1057 – 1060.

Sartor, L. 1990 *Slot coating: Fluid mechanics and die design.* PhD thesis University of Minnesota Published by University Microfilms International, Ann Arbor, MI. Best Seller in 1990.

Schwarz, M. C. 2008 Method and apparatus for coating a medical device using a coating head. US Patent No. 7,371,424.

Schweizer, P. M. 1988 Visualization of coating flows. *J. Fluid. Mech.* **193** 285 – 302.

Schweizer, P. M. and Rossier, P. A. 2003 High Speed Operating Range for Slide Coating. Proceeding of the sixth European coating symposium. Fribourg, Switzerland.

Stay, M. S. and Barocas, V. H. 2003 Coupled lubrication and Stokes flow finite elements. *Int. J. Numer. Meth. Fluids* **43** 129 – 146.

Tallmadge, J. A., Weinberger, C. B. and Faust, H. L. 1979 Bead coating instability: A comparison of speed limit data with theory. *AICHE J.* **25** [No. 6] 1065 – 1072.

Tjiptowidjojo, K. and Carvalho, M. S. 2009 Viscocapillary model of slide coating: Effect of operating parameters and range of validity. *AICHE J.* **55** 2491 – 2505.

Vinokur, M. 1983 On one-dimensional stretching functions for finite-difference calculations. *J. Comp. Phys.* **50** 215 – 234.

Yapel, R. A., Bhave, A. V. and Millbourn, T. M. 1998 Profiled edge guide. US Patent No. 5,837,324.

Youn, S. I., Kim, S. Y., Shin, D. M., Lee, J. S., Jung, H. W. and Hyun, J. C. 2006 A review on viscocapillary models of pre-metered coating flows. *Korea Australia Rheology J.* **18** [No. 4] 209 – 215.

Zevallos, G. A., Carvalho, M. S. and Pasquali, M. 2005 Forward roll coating flows of viscoelastic liquids. *J. Non Newtonian Fluid Mech.* **130** 96 – 109.